isvr Institute of Sound and Vibration Research

Smart Panel with an Array of Decentralized Control Systems for Active Structural Acoustic Control

E. Bianchi, P. Gardonio and S.J. Elliott

ISVR Technical Memorandum No 886

March 2002

University of Southampton

SCIENTIFIC PUBLICATIONS BY THE ISVR

Technical Reports are published to promote timely dissemination of research results by ISVR personnel. This medium permits more detailed presentation than is usually acceptable for scientific journals. Responsibility for both the content and any opinions expressed rests entirely with the author(s).

Technical Memoranda are produced to enable the early or preliminary release of information by ISVR personnel where such release is deemed to the appropriate. Information contained in these memoranda may be incomplete, or form part of a continuing programme; this should be borne in mind when using or quoting from these documents.

Contract Reports are produced to record the results of scientific work carried out for sponsors, under contract. The ISVR treats these reports as confidential to sponsors and does not make them available for general circulation. Individual sponsors may, however, authorize subsequent release of the material.

UNIVERSITY OF SOUTHAMPTON

INSTITUTE OF SOUND AND VIBRATION RESEARCH

SIGNAL PROCESSING AND CONTROL GROUP

Smart Panel with an Array of Decentralized Control Systems for Active Structural Acoustic Control

by

E. Bianchi, P. Gardonio and S.J. Elliott

ISVR Technical Memorandum No. 886

March 2002

Authorized for issue by
Professor S.J. Elliott
Group Chairman

ACKNOWLEDGEMENTS

The experimental work presented in this report has been carried out by Mr. Bianchi within the "European Doctorate in Sound and Vibration Studies" (EDSVS) which is supported by the European Commission through the 'Marie Curie Training Site' programme. Mr. Bianchi would like to thank Professor Gian Luca Ghiringhelli for giving him the opportunity to take part to the EDSVS programme.
Also, the authors would like to thanks Mr Alan Sanders and Mr Robert Stansbridge who built the text rig and the sixteen channel control system respectively. Finally, *PCB Piezotronix* and *Morgan Matroc* are thanks for their support in providing the set of sixteen accelerometers and sixteen piezoceramic patches respectively.

ABSTRACT

This report presents the results of a theoretical and experimental study of active sound transmission through a partition using a smart panel. The system studied consists of a thin aluminium panel of dimensions $414 \times 314 \times 1$ *mm with an embedded array of* 4×4 *square piezoceramic actuators. The sensing system consists of an array of* 4×4 *accelerometers that are positioned on the panel above the centres of the sixteen piezoceramic patches. Each of the sixteen sensor–actuator pairs is arranged to implement local (decentralised) velocity feedback control.*

The report is divided into three parts. In part one a theoretical model is formulated with which the total kinetic energy and sound radiation ratio can be derived as a function of the incident acoustic field and as a function of the feedback gain implemented in the sixteen decentralised control units. Simulations results have been produced with reference to a range of feedback control gains and the results of two cases have been considered. Initially the sensor–actuator transducers have been idealised as sensors devices that precisely detect the point velocity at the centre of the control unit and actuator devices that generates four line moments along the perimeter of each actuator patch. Then, the stiffness and mass effects of the piezoelectric actuators and the mass effects have been taken into account together with the local dynamics of the accelerometers sensors.

In part two the design of a single control unit made of a collocated piezoelectric rectangular patch and an accelerometer has been studied. This study was initially carried out on a pre existing panel with five sensor-actuator units and then completed on a panel with sixteen control devices. The open loop sensor – actuator frequency response function has been studied in order to assess the feasibility of a stable feedback control system. The effects of different positioning of the sensor (same or opposite side of the actuator, slightly off set) and also the difference between force actuation and strain-type actuation via a piezoelectric patch have been assessed experimentally. Also, the effects produced by varying the size of the piezoelectric patch have been considered. Most of the experimental results have been discussed with reference to theoretical ones obtained with simplified analytical models. In particular, the higher frequency dynamics of the actuators (stiffening and mass effects) and of the sensors (mass effect and SDOF resonant effect of the accelerometer) have been studied up to 50 kHz. *Finally, the design of a single channel stable feedback analogue controller has been presented. This includes the design of a compensator circuit to avoid higher frequency instabilities.*

Part three is focussed on the complete smart panel with sixteen decentralised feedback control units. First of all the design of the smart panel and testing rig on which this has been mounted has been described in detail. Then, the design and implementation of sixteen control units are discussed. Finally control results in terms of the velocity at the error sensor positions and in terms of an estimate of the sound power radiated are given.

INDEX

1. INTRODUCTION

During the past two decades the problem of interior noise in passenger transportation vehicles, as for example cars, coaches, trains, helicopters and aircraft, has become more and more important. In general this problem is tackled by using sound insulation materials, by mean of mass, damping and stiffness treatments to the bodywork of the vehicle or by means of shielding techniques of localized sources of noise, as for example engine or gearbox components [1,2]. The acoustic insulation of the engine compartment of cars and coaches has produced good results even though tire noise and, at higher velocities, aerodynamic noise sources are still an open problem. The structure borne noise component has been radically reduced in trains by better designing the suspension systems of the carriages and by providing damping means to the railway truck. Also, noise insulation treatments of the bodywork panels and damping treatments of the framework structure have produced very good high frequencies attenuations. However, the continuous increase of train speed keeps open the aerodynamic noise problem due to turbulent boundary layer air–flow over the coaches bodywork [2]. Finally both helicopter and aircraft vehicles still suffer from relatively high levels of cabin noise that is due to both air–borne (engine noise and turbulent boundary layer excitations) and structure–borne (engine vibration, front and tail wing vibration due to airflow excitations, helicopter main and tail gearbox–rotor vibration) sources [1]. In general passive treatments do not produce good sound insulation at relatively low frequencies where the disturbance wavelength is larger than the characteristic dimensions of the passive isolating system. In particular, manufacturers of both road and air vehicles are finding it difficult to tackle the low frequency noise insulation without increasing the weight of the vehicle. This is a very important problem. In fact, for aircraft and helicopters an increment of weigh has a direct effect on the transportation costs. For road vehicles the increment in weight is also directly related to the cost of the vehicle itself.

Active Noise control (ANC) systems have been successfully developed for the control of low frequencies tonal disturbances in propeller aircraft [3,4]. This type of systems are however relatively costly because they require a large number of control actuators (loudspeakers) and sensors (microphones) which are connected to a multiple channel control system. As a result, this type of active control system has not been implemented in other types of vehicles than propeller aircrafts.

During the past ten years or so, scientists have begun to study new techniques for the Active Structural Acoustic Control (ASAC) through partitions. The first generation of these systems was made of structural actuators mounted on the partition (inertial actuators or strain actuators made using piezoelectric elements) driven by a multiple channel feed–forward control system to minimise the sound radiated as estimated by a set of microphones distributed in the radiating area [5-7]. Although laboratory experiments showed promising results, it soon became clear that this new approach was still limited to the control of tonal disturbances and required relatively large numbers of sensors and actuators to be connected to a multiple channel control unit. Thus the problem of weigh and costs was still unsolved. A second generation of systems was therefore developed which use fewer structural actuators and structural sensors arranged to implement Active Structural Acoustic Control through partitions [8]. In these systems, the sensor and actuator transducers are made of relatively large films of piezoelectric material bonded on the partitions themselves in such a way as to form a very compact and light smart structure. The collocated positioning of the sensor–actuator pair enables the implementation of single channel feedback control system with which both tonal and random incident noise can be controlled [9,10]. Experimental results on

testing smart panels have indicated that this type of systems can give good reductions of low frequencies sound transmission/radiation. However, their implementation in practical applications has been found to be difficult because of the strong dependence between the shaping of the transducers and the geometry–mounting design of the panel, because of the low control authority of piezoelectric films and because of the complicated physical phenomena that characterizes the interaction between the distributed sensor and the distributed actuator bonded on the structure [10,11]. The sensor-actuator coupling problem has been overcame by using discretized version of the volume velocity transducers as described in references [11] and [12]. During the past two years or so scientists have started to investigate a third type of systems which uses large numbers of small collocated sensor–actuator pairs controlled individually by decentralised feedback systems [10,14-16]. These new systems have been designed to overcome the problems found with the other two kinds of active control systems. Indeed the present trend is to use large numbers of sensor–actuator pairs, which however are driven by simple single channel controllers that could be, integrated within the sensor and actuator components. It is hoped that these sensor–controller–actuator systems could be miniaturized to very small and light systems such that light and compact smart panel can be produced.

The study presented in this report is concerned with the design of a smart panel with an array of 16 decentralized sensor–controller–actuator systems. Each control unit is composed by a square piezoelectric small plate bonded on one side of the panel. An accelerometer is placed on the other side of the panel in such a way as it measures the panel transverse velocity in correspondence of the centre of the small piezoelectric actuator. The actuator is driven by a simple analogue feedback controller, which provides a constant gain for the implementation of velocity feedback control.

This type of arrangement was first proposed by Elliott et al. [15] who found that for low gain values the decentralized controllers act as to absorb energy from the low frequency modes of the panel so that both the total kinetic energy of the panel and the sound radiated is slightly reduced in correspondence to the first few resonance frequencies. For very high gains the controllers act as to pin the panel so that the vibration of the panel is rearranged into a new set of modes, which however are very little, damped. As a consequence the total kinetic energy of the panel and the sound radiated are not reduced, on the contrary they can even be increased compared to the values with no control. Elliott et al. [15], however, found that there is an optimal intermediate value of the gain for which the total kinetic energy of the panel and the sound radiated can be substantially reduced.

The report is organised in three parts:

- In part one (section 2) a theoretical model is formulated with which the total kinetic energy and sound radiation ratio can be derived as a function of the incident acoustic field and as a function of the feedback gain implemented in the sixteen decentralised control units. Simulations results have been produced for a range of feedback control gains and the results of two cases have been considered. In case one the sensor–actuator transducers have been idealised as sensors devices that precisely detect the point velocity at the centre of the control unit and actuator devices that generates four line of moments along the perimeter of each actuator patch. In case two, the stiffness and mass effects of the piezoelectric actuators and the mass effects together with the local dynamics of the accelerometers sensors have been taken into account.
- Part two (section 3 and 4) is related to the activity on a pre-existing smart panel of dimensions 278 mm × 247 mm × 1 mm, which is glued on a rigid Perspex frame and it is equipped with five piezoelectric patch strain actuators. With this arrangement the

behaviour of two types of collocated sensor-actuator pairs have been studied: first velocity sensor-force actuator and second velocity sensor-piezo patch strain actuator. Their open loop sensor–actuator frequency response functions are analysed in section 3, considering two possible positions of the sensor-actuator pair: one in the centre and one in the corner. In particular, the mass effects of the transducer elements, the effects due to the first resonance of the accelerometer sensor and the effects due to the dimensions of the piezoelectric patches have been investigated. The implementation of one feedback control system is then described in section 4. The main features of velocity feedback control are then introduced. Finally, the design of a compensator for the implementation of a stable feedback control loop is discussed and control results when the panel is excited by another piezoelectric patch or by a point force with a shaker are shown.

- Part three (section 5 and 6) is concerned with the complete system of sixteen piezoelectric actuators driven locally by the output of sixteen collocated velocity sensors, via individual control loops. First, the design of a smart panel with the array of sixteen sensor – controllers – actuator systems is presented in section 5. Also, for this new panel the frequency response functions of two sensor-actuator pairs are presented with reference to the feedback control requirements. Second, the preparation of a test rig for sound transmission tests is briefly described. The system consists of a box with one side open such that the smart panel can be fixed on it via a rigid metal frame. The box is made of very thick Plexiglas walls so that the noise generated by a loudspeaker placed within the panel is mainly transmitted through the test smart panel. Third, in section 6, the results of real time active control are shown and discussed.

2. SMART PANEL WITH AN ARRAY OF DECENTRALISED SENSORS/ACTUATORS

In this section the sound transmission through the smart panel under study is evaluated numerically. As shown in Figure 2.1 below, the system studied consist of a clamped and baffled aluminium panel of dimensions 414 mm × 314 mm × 1 mm. The panel is excited on one side by a harmonic plane acoustic wave of unit amplitude. The azimuthal and lateral incidence angles of the acoustic wave are chosen to be of $\phi = 45^o$ and $\theta = 45^o$ so that all the structural modes of the panel are excited. The panel radiates sound on the other side of the panel into free field. A weakly coupled model is used to describe the sound transmission through the panel which assumes that the acoustic pressure of the radiated sound has no effect on the vibration of the panel, which is a reasonable assumption in air for this thickness of panel.

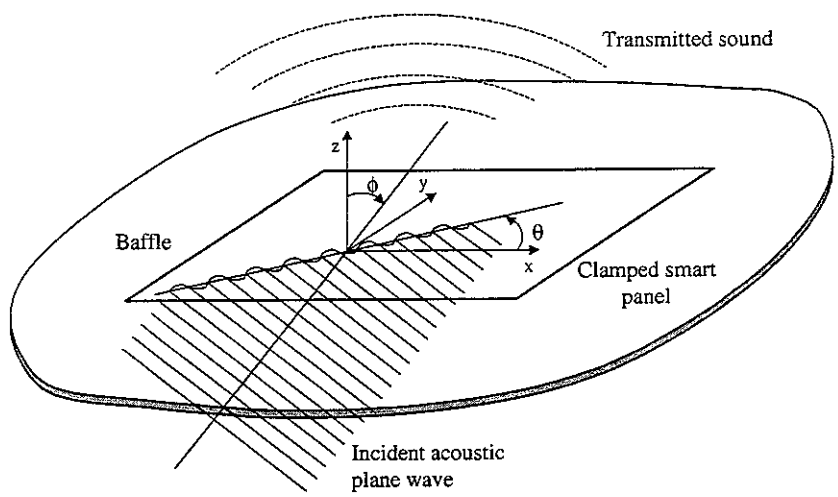

Figure 2.1: *Physical arrangement for the computer simulations, in which the vibration of a baffled clamped panel is excited by a plane acoustic wave on one side and radiates sound into an anechoic half space on the other side of the panel.*

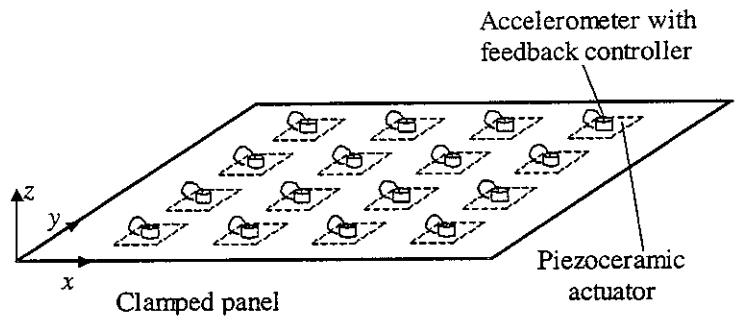

Figure 2.2: *Smart panel with a 4×4 array of decentralized control systems composed by an accelerometer sensor with a built in feedback control system and a piezoceramic actuator is mounted on the panel to implement vibro–acoustic control.*

As shown in Figure 2.2, the panel is equipped with an array of 4×4 control systems that operate independently. The sixteen control systems have been equally spaced along the x– and y–directions so that the distances between two actuators or between a lateral actuator and the edge of the plate are $d_x = l_x/5 = 82.8\,\text{mm}$ and $d_y = l_y/5 = 62.8\,\text{mm}$. Each control system consist of a piezoelectric actuator, of dimensions 25 mm × 25 mm × 0.5 mm, which is bonded on the excited side of the panel and a small accelerometer which is placed on the other side of the panel in correspondence of the centre of the actuator. The actuator is driven by a small single–channel analogue controller that implement velocity feedback control and could be integrated within the accelerometer case. Tables 2.1 to 2.3 below summarize the geometrical and physical properties of the system.

Table 2.1: *Geometry and physical constants for the panel.*

Parameter	Value
dimensions	$l_x \times l_y = 414 \times 314$ mm
thickness	$h_s = 1$ mm
mass density	$\rho_s = 2700\,\text{Kg/m}^3$
Young's modulus	$E_s = 7 \times 10^{10}$ N/m^2
Poisson ratio	$\nu_s = 0.33$
loss factor	$\eta_s = 0.05$
Smeared mass density (including part of the mass effects of the piezo actuators)	$\overline{\rho}_s = 3000\,\text{Kg/m}^3$
Smeared Young's modulus (including the stiffening effects of the piezo actuators)	$\overline{E}_s = 7.1 \times 10^{10}$ N/m^2

Table 2.2: *Geometry and physical constants for the PZT patches.*

Parameter	Value
Dimensions of the PZT patches	$l_{xp} \times l_{yp} = 25 \times 25$ mm
Thickness of the PZT patches	$h_p = 0.5$ mm
Young's modulus	$E_p = 2 \times 10^9$ N/m^2
Poisson ratio	$\nu_p = 0.29$
Stress constant	$e_{31} = 0.052$ N/Vm
Strain constant	$d_{31} = 23 \times 10^{-12}$ m/V
Distance between the centres of two adjacent patches	$d_x \times d_y = 82.8 \times 62.8$ mm

The steady state response of the panel and sound radiation in a frequency range 0 to 1 kHz have been calculated assuming the primary disturbance to be harmonic with time dependence of the form $\exp(j\omega t)$. The velocity-type and force-type parameters used in the model have been taken to be the real part of counter clock wise rotating complex vectors, e.g. phasors. The velocity or force parameters are therefore given by $\dot{w}(t) = \mathrm{Re}\{\dot{w}(\omega)e^{j\omega t}\}$ or $f(t) = \mathrm{Re}\{f(\omega)e^{j\omega t}\}$ where $\dot{w}(\omega)$ and $f(\omega)$ are the velocity and force phasor at the instant $t = 0$.

2.1 Mathematical model

The mathematical model built in for the simulations considers the panel divided into a grid of rectangular elements whose dimensions have been taken to be $l_{xe} = l_x/(4M)$ and $l_{ye} = l_y/(4N)$, where M and N are the higher modal orders used in the calculus.

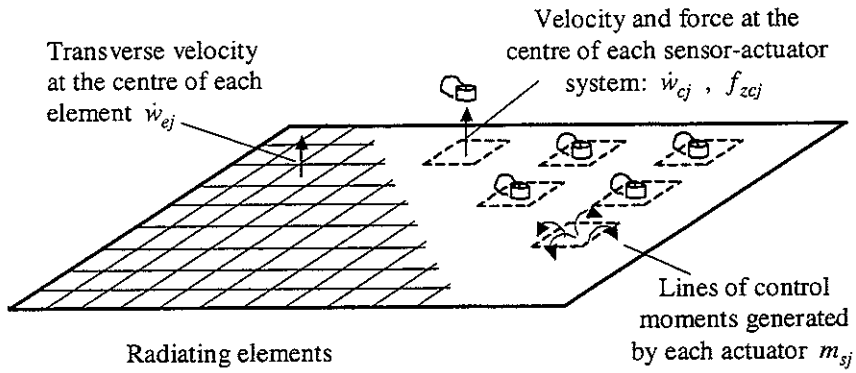

Figure 2.3: *Velocity and force-moment notation used in the mathematical model.*

The phasors of the transverse velocities, $\dot{w}_{ej}(\omega)$ at the centres of these elements have been grouped into the following vector:

$$\mathbf{v}_e(\omega) \equiv \begin{Bmatrix} \dot{w}_{e1}(\omega) \\ \dot{w}_{e2}(\omega) \\ \vdots \\ \dot{w}_{eP}(\omega) \end{Bmatrix}, \tag{2.1}$$

where $P = 8MN$ is the total number of elements. Similarly the phasors of the transverse velocities, $\dot{w}_{cj}(\omega)$, and forces, $f_{zcj}(\omega)$, at the centres of each control systems have been defined as follows:

$$\mathbf{v}_c(\omega) \equiv \begin{Bmatrix} \dot{w}_{c1}(\omega) \\ \dot{w}_{c2}(\omega) \\ \vdots \\ \dot{w}_{c16}(\omega) \end{Bmatrix} \qquad \mathbf{f}_c(\omega) \equiv \begin{Bmatrix} f_{zc1}(\omega) \\ f_{zc2}(\omega) \\ \vdots \\ f_{zc16}(\omega) \end{Bmatrix}, \tag{2.2a,b}$$

The primary excitation is given by the amplitude of the incident acoustic wave in which case:

$$\mathbf{f}_p(\omega) = p_i(\omega) \tag{2.3}$$

The excitations of the sixteen piezoelectric control actuators can be approximated by four line moments, all with equal magnitude, acting along the edges of the piezoelectric patches so that the control excitations can be grouped into a vector of moments as follows:

$$\mathbf{f}_s(\omega) = \begin{Bmatrix} m_{s1}(\omega) \\ m_{s2}(\omega) \\ \vdots \\ m_{s16}(\omega) \end{Bmatrix} \tag{2.4}$$

The vibration of the panel at the centres of the elements and at the centres of the control systems can be expressed in matrix form using mobility functions so that:

$$\mathbf{v}_e(\omega) = \mathbf{Y}_{ep}(\omega)\mathbf{f}_p(\omega) + \mathbf{Y}_{es}(\omega)\mathbf{f}_s(\omega) \ , \tag{2.5}$$

$$\mathbf{v}_c(\omega) = \mathbf{Y}_{cp}(\omega)\mathbf{f}_p(\omega) + \mathbf{Y}_{cs}(\omega)\mathbf{f}_s(\omega) \ , \tag{2.6}$$

where the elements of the four mobility matrices are defined as follows [17]:

$$Y_{ep}^{p,1}(\omega) = \frac{\dot{w}_{e,p}(\omega)}{p_i(\omega)} = j\omega \sum_{m=1}^{M}\sum_{n=1}^{N} \frac{\phi(x_{ep}, y_{ep}) \int_0^{l_y}\int_0^{l_x} \phi(x,y)dxdy}{\Lambda_{mn}\left[\omega_{mn}^2(1+j\eta_s) - \omega^2\right]} \ , \tag{2.7}$$

$$Y_{es}^{p,q}(\omega) = \frac{\dot{w}_{e,p}(\omega)}{m_{s,q}(\omega)} = j\omega \sum_{m=1}^{M}\sum_{n=1}^{N} \frac{\phi(x_{ep}, y_{ep})\left\{\int_0^{a_x} \psi^{(y)}(x_{sq}, y_{sq1}) + \psi^{(y)}(x_{sq}, y_{sq2})dx + \int_0^{a_y} \psi^{(x)}(x_{sq1}, y_{sq}) + \psi^{(x)}(x_{sq2}, y_{sq})dy\right\}}{\Lambda_{mn}\left[\omega_{mn}^2(1+j\eta_s) - \omega^2\right]} \ , \tag{2.8}$$

$$Y_{cp}^{p,1}(\omega) = \frac{\dot{w}_{c,p}(\omega)}{p_i(\omega)} = j\omega \sum_{m=1}^{M}\sum_{n=1}^{N} \frac{\phi(x_{cp}, y_{cp}) \int_0^{l_y}\int_0^{l_x} \phi(x,y)dxdy}{\Lambda_{mn}\left[\omega_{mn}^2(1+j\eta_s) - \omega^2\right]} \ , \tag{2.9}$$

$$Y_{cs}^{p,q}(\omega) = \frac{\dot{w}_{c,p}(\omega)}{m_{s,q}(\omega)} = j\omega \sum_{m=1}^{M}\sum_{n=1}^{N} \frac{\phi(x_{cp}, y_{cp})\left\{\int_0^{a_x} \psi^{(y)}(x_{sq}, y_{sq1}) + \psi^{(y)}(x_{sq}, y_{sq2})dx + \int_0^{a_y} \psi^{(y)}(x_{sq1}, y_{sq}) + \psi^{(y)}(x_{sq2}, y_{sq})dy\right\}}{\Lambda_{mn}\left[\omega_{mn}^2(1+j\eta_s) - \omega^2\right]} \ , \tag{2.10}$$

where:

$\dot{w}(\omega)$	is the phasor of the panel velocity in z–direction,
$p_i(\omega)$	is the sound pressure phasor of the incident acoustic wave,
ω	is the circular frequency ,
j	is the complex operator ,
m,n	are modal indices ,
ω_{mn}	is the natural frequency of the m,n-th mode,
$\phi_{mn}(x,y)$	is the m,n-th bending natural mode at position (x,y) ,
E_s	is the Young's modulus of elasticity ,
ρ_s	is the density of the material of the panel ,
ν_s	is the Poisson ratio ,
η_s	is the hysteresis loss factor ,
$\Lambda_{mn} = \rho_s h_s l_x l_y / 4$	is a modal normalisation parameter ,
$\psi_{mn}^{(x)}(x,y) = \dfrac{\partial \phi_{mn}(x,y)}{\partial x}$,	is the first derivative in x direction of the m,n-th bending natural mode at position (x,y) ,
$\psi_{mn}^{(y)}(x,y) = -\dfrac{\partial \phi_{mn}(x,y)}{\partial y}$,	is the first derivative in y direction of the m,n-th bending natural mode at position (x,y) ,

For a clamped rectangular thin panel the natural frequencies are given by [17]:

$$\omega_{fmn} = \sqrt{\frac{E_s h_s^2}{12\rho_s(1-\nu_s^2)}} \cdot \left(\frac{\pi}{l_x}\right)^2 q_{mn} \tag{2.11}$$

where ω_{fmn} is in rad/s and

$$q_{mn} = \sqrt{G_x^4(m) + G_y^4(n)\left(\frac{l_x}{l_y}\right)^4 + 2\left(\frac{l_x}{l_y}\right)^2 \left[\nu H_x(m)H_y(n) + (1-\nu)J_x(m)J_y(n)\right]} , \tag{2.12}$$

and the constants G_x, G_y, H_x, H_y, J_x, J_y are summarised in Table 2.3 below

Table 2.3: *Values for the constants G_x, G_y, H_x, H_y, J_x, J_y when a rectangular plate has all four edges are clamped (from reference* [17,18]*).*

m or n	G_x or G_y	H_x or H_y	J_x or J_y
1	1.506	1.248	1.248
2,3,4,....	$m+\frac{1}{2}$	$\left(m+\frac{1}{2}\right)^2\left(1-\frac{4}{(2m+1)\pi}\right)$	$\left(m+\frac{1}{2}\right)^2\left(1-\frac{4}{(2m+1)\pi}\right)$

The plate natural modes $\phi_{mn}(x,y)$ are given by the product of the $\varphi_m(x)$ and $\varphi_n(y)$ beam functions

$$\phi_{mn}(x,y)=\varphi_i(x)\varphi_k(y). \tag{2.13}$$

The function $\varphi_i(x)$ represents the natural modes of a beam having the same boundary conditions of the plate under consideration at $y=0$ and $y=l_y$ and, in the same way, the function $\varphi_k(y)$ represents the natural modes of a beam having the same boundary conditions of the plate under consideration at $x=0$ and $x=l_x$.

The boundary conditions for a plate with all edges clamped are given by [18]:

$$\begin{array}{lll} x=0 \text{ and } x=l_x & w=0 & \dfrac{\partial w}{\partial x}=0 \\ y=0 \text{ and } y=l_y & w=0 & \dfrac{\partial w}{\partial y}=0 \end{array} \tag{2.14}$$

and the beam functions in the x-direction for a clamped-clamped beam, also given in references [17,18], are:

$$\begin{aligned} \varphi_{1,3,5,\ldots}(x) &= \cos\gamma_m\left(\frac{x}{l_x}-\frac{1}{2}\right)+k_m\cosh\gamma_m\left(\frac{x}{l_x}-\frac{1}{2}\right) \\ \varphi_{2,4,8,\ldots}(x) &= \sin\gamma'_m\left(\frac{x}{l_x}-\frac{1}{2}\right)+k'_m\sinh\gamma'_m\left(\frac{x}{l_x}-\frac{1}{2}\right) \end{aligned}. \tag{2.15a,b}$$

where in this case

$$k_m=\frac{\sin(\gamma_m/2)}{\sinh(\gamma_m/2)} \qquad k'_m=-\frac{\sin(\gamma'_m/2)}{\sinh(\gamma'_m/2)}. \tag{2.16a,b}$$

and the constants γ_m and γ'_m are the m-th zeros of the two following implicit equations

$$\tan(\gamma_m/2)+\tanh(\gamma_m/2)=0 \qquad \tan(\gamma'_m/2)-\tanh(\gamma'_m/2)=0 \tag{2.17a,b}$$

whose roots are summarised in Table 2.4. The beam functions in the y-direction are the same as those in the x-direction given by equations (2.15.a) and (2.15.b) and are all normalised so that the norm Λ_{mn} for a plate with all edges clamped is given by $\Lambda_{mn} = \rho_s h_s l_x l_y / 4$.

Table 2.4: *Roots for the 2 equations (17a) and (17b). r=6,7,8,9,....*

$\gamma_1 = 4{,}7300$	$\gamma'_2 = 7{,}8532$
$\gamma_3 = 10{,}9956$	$\gamma'_4 = 14{,}1372$
$\gamma_5 = 17{,}2788$	$\gamma'_6 = 20{,}4204$
$\gamma_7 = 23{,}5620$	$\gamma'_8 = 26{,}7036$
$\gamma_9 = 29{,}8452$	$\gamma'_{10} = 32{,}9868$
$\gamma_{11,13,\ldots} = (4r-1)\pi/2$	$\gamma'_{12,14,\ldots} = (4r+1)\pi/2$

Using beam functions, the first derivative modes function are given by the following relations:

$$\psi^{(x)}_{mn}(x,y) = \varphi_i(x)\cdot\frac{\partial\varphi_k(y)}{\partial y} \qquad \psi^{(y)}_{mn}(x,y) = -\varphi_k(y)\cdot\frac{\partial\varphi_i(x)}{\partial x}. \tag{2.18a,b}$$

so that

$$\frac{\partial\varphi_{1,3,5,\ldots}(x)}{\partial x} = \frac{\gamma_m}{l_x}\left\{-\sin\gamma_m\left(\frac{x}{l_x}-\frac{1}{2}\right)+k_m\sinh\gamma_m\left(\frac{x}{l_x}-\frac{1}{2}\right)\right\}$$
$$\frac{\partial\varphi_{2,4,6,\ldots}(x)}{\partial x} = \frac{\gamma'_m}{l_x}\left\{\cos\gamma'_m\left(\frac{x}{l_x}-\frac{1}{2}\right)+k'_m\cosh\gamma'_m\left(\frac{x}{l_x}-\frac{1}{2}\right)\right\} \tag{2.19a,b}$$

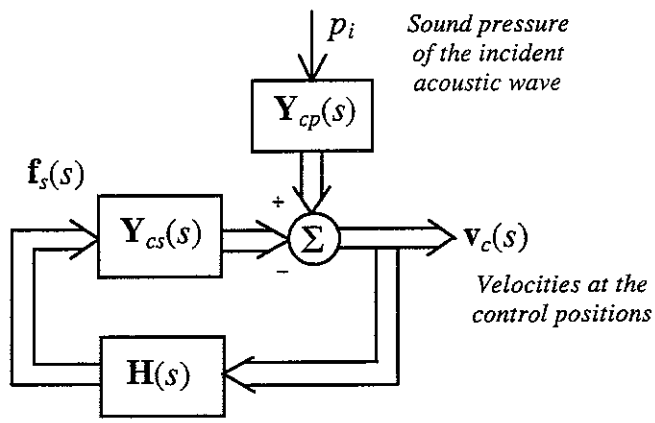

Figure 2.4: *Multichannel feedback control system, which for a passive plant response, $\mathbf{Y}_{cs}(s)$, and a passive controller $\mathbf{H}(s)$, is unconditionally stable.*

If there is no control action, i.e. $\mathbf{f}_s(\omega) \equiv \mathbf{0}$, then the transverse velocities at the centre positions of the panels can be calculated directly from equation (2.5) to be:

$$\mathbf{v}_e(\omega) = \mathbf{Y}_{ep}(\omega)\mathbf{f}_p(\omega) \ , \tag{2.20}$$

Provided the control system is stable, if, as shown in Figure 2.4, for each sensor–actuator pair a decentralized feedback control loop is implemented with constant feedback gain, h, such that:

$$\mathbf{f}_s(\omega) = -\mathbf{H}(\omega)\mathbf{v}_c(\omega) \ , \tag{2.21}$$

where

$$\mathbf{H}(\omega) = \begin{bmatrix} h_1 & & & \\ & h_2 & & \\ & & \ddots & \\ & & & h_{16} \end{bmatrix} , \tag{2.22}$$

then, as can be deduced by the block diagram in Figure 2.3 the velocities at the centre positions of the control system are given by:

$$\mathbf{v}_c(\omega) = \left(\mathbf{I} + \mathbf{Y}_{cs}(\omega)\mathbf{H}(\omega)\right)^{-1}\mathbf{Y}_{cp}(\omega)\mathbf{f}_p(\omega) \ . \tag{2.23}$$

Also, from equations (2.5), (2.21) and (2.23), the transverse velocities at the centre positions of the panels can be calculated as a function of the primary excitation vector and the gains in the matrix $\mathbf{H}(\omega)$:

$$\mathbf{v}_e(\omega) = \left[\mathbf{Y}_{ep}(\omega) - \mathbf{Y}_{es}(\omega)\mathbf{H}(\omega)\left(\mathbf{I} + \mathbf{Y}_{cs}(\omega)\mathbf{H}(\omega)\right)^{-1}\mathbf{Y}_{cp}(\omega)\right]\mathbf{f}_p(\omega) \ , \tag{2.24}$$

It should be underlined that these results are valid provided the sixteen decentralized feedback control units are all stable. Elliott et all. [15] have shown that this is true when collocated and compatible transducers are used. Elliott et all. [15] have also shown that a collocated piezoceramic actuator patch and accelerometer sensor where the actuator is modelled as a set of four line-moment excitation and the sensor is modelled such that it precisely measures the transverse velocity in correspondence to the centre of the actuator patch, then, at low frequency, the system is stable. In the second part of this report the true behaviour of these two transducers is analysed in more details both experimentally and with a more detailed analytical model that takes into account the stiffness and mass effects of the piezoelectric actuator and takes into account the dynamics of the accelerometer. It is here anticipated that when the true transducers are analysed, then each control unit is not guaranteed to be stable above few kilo Hertz. A limited feedback gain is therefore required in equations (2.23) and (2.24) otherwise they can not assumed to be true since the control units are unstable.

The total kinetic energy of the panel or the total sound power radiated per unit primary excitation can be derived from the velocities of the radiating elements given in equation (2.24). The total kinetic energy of the panel is given by

$$E(\omega) = \frac{\rho_s h_s}{2} \int_{S_s} |\dot{w}(x, y, \omega)|^2 \, dx \, dy \,, \tag{2.25}$$

where S_s is the surface area of the panel. This expression can be approximated to the summation of the kinetic energies of each element into which the panel has been subdivided so that:

$$E(\omega) = \frac{m_s}{2} \mathbf{v}_e^H(\omega) \mathbf{v}_e(\omega) \,, \tag{2.26}$$

where $m_s = \rho_s h_s$ is the mass per unit area of the panel. The total sound power radiation by a baffled panel can be derived by integrating the product of the nearfield sound pressure on the radiating side and the transverse velocity of the panel so that

$$W(\omega) = \frac{1}{2} \int_0^{l_x} \int_0^{l_y} p_o(x, y, \omega)^* \dot{w}(x, y, \omega) \; dx \; dy \,, \tag{2.27}$$

The sound pressures in front of the panel $p_o(x, y, \omega)$ is related to the transverse velocity of the panel at the same position by the specific acoustic impedance in air Z_o so that:

$$p_o(x, y, \omega) = Z_o \dot{w}(x, y, \omega) \,. \tag{2.28}$$

Similarly to the case of kinetic energy, the integral in equation (2.17) can be approximated to the radiated sound power by all the elements into which the panel has been subdivided so that the total sound power radiation can be expressed as:

$$W(\omega) = \frac{\Delta S_s}{2} \mathrm{Re}\left[\mathbf{v}_e^H(\omega) \mathbf{p}(\omega)\right]. \tag{2.29}$$

where ΔS_s is the area of each element and $\mathbf{p}(\omega)$ is the vector with the sound pressure terms in front of the panel at the centre positions of the grid of elements:

$$\mathbf{p}(\omega) = \begin{Bmatrix} p_1(\omega) \\ p_2(\omega) \\ \vdots \\ p_{16}(\omega) \end{Bmatrix}. \tag{2.30}$$

Equation (2.29) can also be written as

$$W(\omega) = \frac{\Delta S_s}{2} \mathrm{Re}\left[\mathbf{v}_e^H(\omega) \mathbf{Z}(\omega) \mathbf{v}(\omega)_e\right] = \mathbf{v}_e^H(\omega) \mathbf{R}(\omega) \mathbf{v}_e(\omega) \,, \tag{2.31}$$

where $\mathbf{Z}$ is the matrix with the point and transfer acoustic impedance terms over the grid of point into which the panel has subdivided [19]

$$\mathbf{Z}(\omega)=\frac{\omega^2\rho_o}{2\pi c_o}\begin{bmatrix} 1 & \frac{\sin(k_o r_{12})}{k_o r_{12}} & \cdots & \frac{\sin(k_o r_{1I})}{k_o r_{1I}} \\ \frac{\sin(k_o r_{21})}{k_o r_{21}} & 1 & & \\ \cdots & \cdots & \cdots & \cdots \\ \frac{\sin(k_o r_{I1})}{k_o r_{I1}} & & & 1 \end{bmatrix}, \tag{2.32}$$

where $k_o=\omega/c_o$ is the acoustic wavenumber in air and r_{ij} is the distance between i-th and j-th elements. The radiation matrix $\mathbf{R}$ is therefore given by [19]:

$$\mathbf{R}(\omega)=\left(\frac{\Delta S_s}{2}\right)\mathrm{Re}[\mathbf{Z}(\omega)]=\frac{\omega^2\rho_o S_s^2}{4\pi c_o}\begin{bmatrix} 1 & \frac{\sin(k_o r_{12})}{k_o r_{12}} & \cdots & \frac{\sin(k_o r_{1I})}{k_o r_{1I}} \\ \frac{\sin(k_o r_{21})}{k_o r_{21}} & 1 & & \\ \cdots & \cdots & \cdots & \cdots \\ \frac{\sin(k_o r_{I1})}{k_o r_{I1}} & & & 1 \end{bmatrix}, \tag{2.33}$$

Although the sound power radiated by the panel usefully quantifies the far-field pressure it generates, high vibration levels in weakly radiated modes can give rise to significant pressure levels in the near-field of the panel. It has been shown that the total kinetic energy of a panel provides a better measure of near-field pressure than radiated sound power [8], and so if there is any possibility that listeners may be in close proximity to the panel, as well as being further away, then both of these criteria are important for active structural acoustic control.

For practical computations only a finite number of modes can be used in the expansion for the mobility functions given by equations (2.7) to (2.10). The convergence of the modal series can be investigated by calculating the ratio of the velocity computed at a point on the panel with a modal summation using N modes, to that computed with a large number of modes, such as 500, with natural frequencies up to 25 kHz. This result can be misleading for the active control simulations presented here, however, since very high levels of attenuation are predicted at some frequencies and so the residual components of the vibration may be more sensitive to modal truncation. The results presented here were obtained by taking in equation (2.7) to (2.10) the natural modes and natural frequencies up to 25 kHz. This was chosen since none of the results presented here was significantly altered if the upper limit of the modal summation was higher. A large number of modes is required to accurately model the velocity with a collocated actuator because the velocity is influenced by the nearfield of the actuator, which is more intense for the piezoelectric actuator than it is for the point force. It should be noted that only the line moment excitation of the piezoelectric actuator [20] has been taken into account in the model, not the local stiffening effect.

2.2 Sensor–actuator dynamic effects

The matrix model introduced above neglects two features of the system:

(a) the dynamic effects of the piezoelectric actuators and accelerometer sensors, and

(b) the frequency response function of the accelerometer sensor.

The small dimensions of one sensor–actuator pair compared to that of the panel justify this choice. However, because the panel is equipped with sixteen of these control systems, their dynamic effects are certainly important even at low frequencies. Also, the accelerometer sensor operates as a single degree resonant system with natural frequency at relatively high frequency, in general about 20–30 kHz, and thus the high frequency response of the panel with the sixteen accelerometer sensors could be quite different to that of the panel on itself.

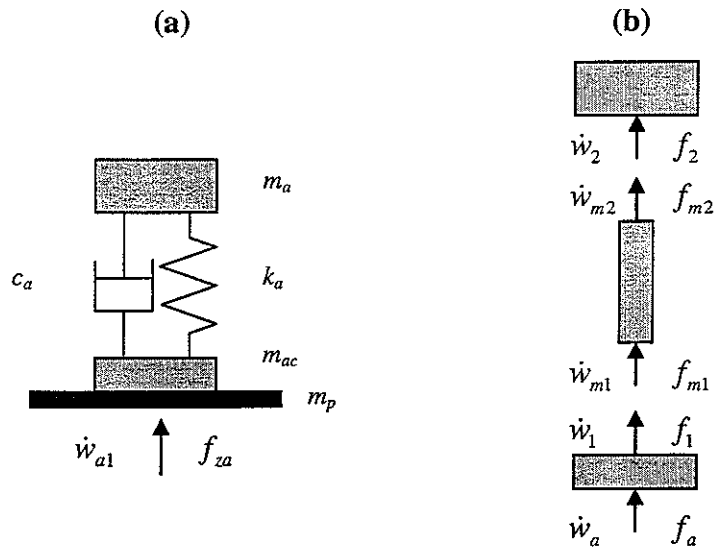

Figure 2.5: *Mobility diagram of one sensor–actuator system, which has been modelled with three lumped elements: the accelerometer inertial mass, equivalent stiffness and damping of the sensing piezo element and the mass of the accelerometer case. The dynamic effects of the piezoelectric actuator have instead been smeared over the panel surface by modifying the Young's modulus and density parameters of the panel.*

Since the piezoelectric patches are uniformly distributed over the panel surface and, up to 1 kHz, their surface dimensions are not negligible if compared to the wave length of the bending vibration in the panel, then their stiffness and part of the mass effects can be modelled as a smeared effect over the entire surface of the panel so that low order mode shapes remains unaltered and the variation of the natural frequencies can be easily derived assuming a higher bending stiffness and density of the panel. The local dynamics of sensor–accelerometer plus part of the mass effect of the piezo actuator have instead been modelled with a lumped parameter that accounts for the inertial mass, stiffness and damping of the accelerometer and the mass of accelerometer case plus part of the mass of the piezoelectric actuator arranged as shown in Figure 2.5.

The driving point impedance of each accelerometer sensor $Z(\omega) = f_{cz}(\omega)/\dot{w}_c(\omega)$ can easily derived by considering the diagram in Figure 2.4(b) above [21]. For the top and bottom masses the following two relations can be written:

$$\dot{w}_2(\omega) = Y_2(\omega) f_2(\omega) \ , \tag{2.34}$$

$$\dot{w}_1(\omega) = Y_1(\omega) f_1(\omega) + Y_1(\omega) f_a(\omega) \ , \tag{2.35}$$

where $Y_2(\omega)$ and $Y_1(\omega)$ are the mobility terms for the two masses:

$$Y_2(\omega) = \frac{1}{j\omega m_a} \ , \qquad Y_1(\omega) = \frac{1}{j\omega m_{ac}} \ , \tag{2.36,2.37}$$

Also, for the four poles mounting system described by a spring element and damping element in parallel, the following two equations can be written:

$$\begin{aligned} f_{m1}(\omega) &= Z_{m11}(\omega)\dot{w}_{m1}(\omega) + Z_{m12}(\omega)\dot{w}_{m2}(\omega) \\ f_{m2}(\omega) &= Z_{m21}(\omega)\dot{w}_{m2}(\omega) + Z_{m22}(\omega)\dot{w}_{m2}(\omega) \end{aligned} \ , \tag{2.38a,b}$$

where the four impedance terms are given by

$$\begin{aligned} Z_{m11}(\omega) &= \left(c_a + \frac{k_a}{j\omega} \right) \quad Z_{m12}(\omega) = -\left(c_a + \frac{k_a}{j\omega} \right) \\ Z_{m21}(\omega) &= -\left(c_a + \frac{k_a}{j\omega} \right) \quad Z_{m22}(\omega) = \left(c_a + \frac{k_a}{j\omega} \right) \end{aligned} \ , \tag{2.39a-c}$$

Using (a) the dynamic equilibrium and (b) compatibility conditions at the top and bottom junctions, so that

(a) dynamic equilibrium $\qquad f_1 = -f_{m1}$ and $f_2 = -f_{m2}$ (2.40a,b)

(b) compatibility $\qquad \dot{w}_1 = \dot{w}_{m1}$ and $\dot{w}_2 = \dot{w}_{m2}$ (2.41a,b)

the following equation is obtained

$$\dot{w}_1(\omega) = \frac{Y_1(\omega)}{1 - T(\omega)} f_a(\omega) \ , \tag{2.42}$$

$$T(\omega) = -Y_1(\omega) Z_{m11}(\omega) + \frac{Y_1(\omega) Z_{m12}(\omega) Y_2(\omega) Z_{m21}(\omega)}{1 + Y_2(\omega) Z_{m22}(\omega)} \ , \tag{2.43}$$

Thus, since $\dot{w}_a(\omega) = \dot{w}_1(\omega)$, the equivalent impedance of the mechanical system shown in Figure 4 can be calculated to be:

$$Z_{eq}(\omega) = \frac{f_a(\omega)}{\dot{w}_a(\omega)} = \frac{1 - T(\omega)}{Y_1(\omega)} \quad . \tag{2.44}$$

As well known, the output signal of accelerometers is proportional to the differential acceleration of the accelerometer–mass and accelerometer–case:

$$\text{measured acceleration} \propto \ddot{w}_2 - \ddot{w}_a \quad . \tag{2.45}$$

Thus, for a given velocity at the mounting point of the accelerometer $\dot{w}_c = \dot{w}_a$ the measured value is given by:

$$\dot{w}_{mes}(\omega) = A(\omega)\dot{w}_c(\omega) \quad . \tag{2.46}$$

where $A(\omega)$ is the accelerometer frequency response function [22]:

$$A(\omega) = \frac{m_a}{k_a - m_a\omega^2 + jc_a\omega} = \frac{1}{\omega_n^2 - \omega^2 + j\xi_a 2\omega\omega_n} \quad . \tag{2.47}$$

with $\omega_n = \sqrt{k_a/m_a}$ the accelerometer natural frequency and $\xi_a = c_a/2\sqrt{k_a m_a}$ the damping ratio of the accelerometer.

Table 2.5: *Physical properties of the sensor-actuator transducers.*

Parameter	Value
Mass of the piezo actuator	$m_p = 0.2\times10^{-3}$ Kg
Mass of the accelerometer case	$m_{ac} = 0.2\times10^{-3}$ Kg
Inertia mass of the accelerometer	$m_a = 0.22\times10^{-3}$ Kg
Stiffness of the accelerometer	$k_a = 1.1\times10^{7}$ N/m
Mounted frequency resonance of accelerometer	$f_a = \omega_n/2\pi = 33.6\times10^{3}$ Hz
Damping coefficient of the accelerometer	$c_a = 2.5$ N/ms^{-1}

In the next subsection, for the simulations in which the sensor-actuator local dynamic effects have been taken into account, the physical parameters given in Table 2.5 above have been used. As discussed above the mass effect of the piezo actuators have been taken into account partially as a localized effect and partially as a smeared effect over the panel surface. As a result, the lumped mass of each piezo actuator has been taken to be $m_p = 0.2\times10^{-3}$ Kg,

although the true mass is 1×10^{-3} Kg. In order to account for the smeared inertia effect of the sixteen piezo actuators, the density of the material of the panel has been taken to be: $\overline{\rho}_s = 3000\,\mathrm{Kg/m^3}$. The stiffening effect of the piezo actuators has also been smeared over the panel and thus the Young's modulus of elasticity used in the simulations has been assumed to be $\overline{E}_s = 7.1\times10^{10}\ \mathrm{N/m^2}$.

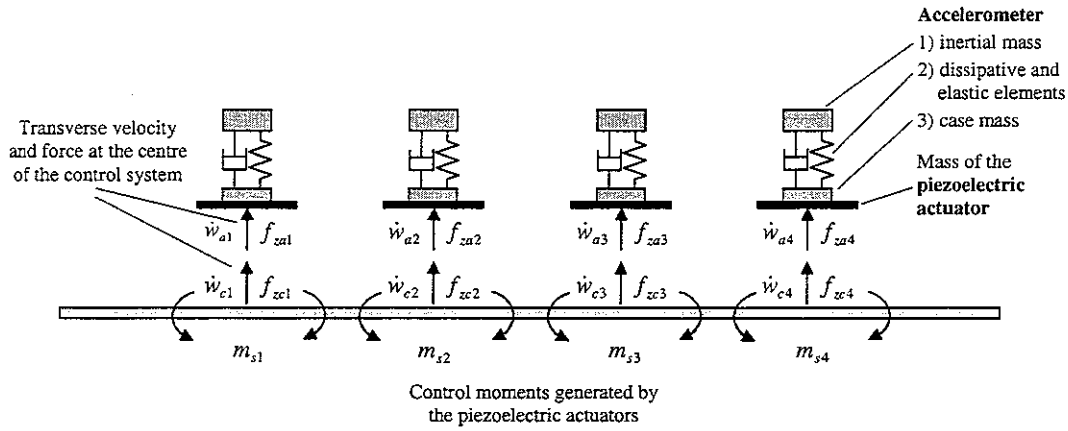

Figure 2.6: *Schematic representation of the sensor–actuator elements, which are represented by four lumped elements: the mass of the piezoelectric actuator, the mass of the case of the accelerometer and the spring and inertial mass in the accelerometer.*

When the dynamic effects of the sixteen sensor–actuator systems are taken into account then, according to the notation shown in Figure 2.6 above, equations (2.5) and (2.6) should be reformulated as follows:

$$\mathbf{v}_e(\omega) = \mathbf{Y}_{ec}(\omega)\mathbf{f}_c(\omega) + \mathbf{Y}_{ep}(\omega)\mathbf{f}_p(\omega) + \mathbf{Y}_{es}(\omega)\mathbf{f}_s(\omega)\ , \tag{2.48}$$

$$\mathbf{v}_c(\omega) = \mathbf{Y}_{cc}(\omega)\mathbf{f}_c(\omega) + \mathbf{Y}_{cp}(\omega)\mathbf{f}_p(\omega) + \mathbf{Y}_{cs}(\omega)\mathbf{f}_s(\omega)\ , \tag{2.49}$$

where the elements of the $\mathbf{Y}_{ec}(\omega)$ and $\mathbf{Y}_{cc}(\omega)$ matrices are given by:

$$Y_{ec}^{p,q}(\omega) = \frac{\dot{w}_{e,p}(\omega)}{f_{zc,q}(\omega)} = j\omega\sum_{m=1}^{M}\sum_{n=1}^{N}\frac{\phi(x_{ep},y_{ep})\phi(x_{eq},y_{eq})}{\Lambda_{mn}\left[\omega_{mn}^2(1+j\eta_s)-\omega^2\right]}\ . \tag{2.50}$$

$$Y_{cc}^{p,q}(\omega) = \frac{\dot{w}_{c,p}(\omega)}{f_{zc,q}(\omega)} = j\omega\sum_{m=1}^{M}\sum_{n=1}^{N}\frac{\phi(x_{cp},y_{cp})\phi(x_{cq},y_{cq})}{\Lambda_{mn}\left[\omega_{mn}^2(1+j\eta_s)-\omega^2\right]}\ . \tag{2.51}$$

According to equation (2.44), the phasors of the transverse velocities , $\dot{w}_{aj}(\omega)$, and forces, $f_{zaj}(\omega)$, at the centres of each control systems can be related by the following impedance expression:

$$f_{zaj}(\omega) = Z_{eq}(\omega)\dot{w}_{aj}(\omega) \ . \tag{2.52}$$

Thus, defining the vectors $\mathbf{v}_a(\omega)$ and $\mathbf{f}_a(\omega)$ to be given by the velocities and forces at the bottom of the accelerometer sensors respectively:

$$\mathbf{v}_a(\omega) \equiv \begin{Bmatrix} \dot{w}_{a1}(\omega) \\ \dot{w}_{a2}(\omega) \\ \vdots \\ \dot{w}_{a16}(\omega) \end{Bmatrix} \qquad \mathbf{f}_a(\omega) \equiv \begin{Bmatrix} f_{za1}(\omega) \\ f_{za2}(\omega) \\ \vdots \\ f_{za16}(\omega) \end{Bmatrix} \ . \tag{2.53a,b}$$

then

$$\mathbf{f}_a(\omega) = \mathbf{Z}_{aa}(\omega)\mathbf{v}_a(\omega) \ . \tag{2.54}$$

where the impedance matrix $\mathbf{Z}_{aa}(\omega)$ is diagonal

$$\mathbf{Z}_{aa}(\omega) = \begin{bmatrix} Z_{eq1} & & & \\ & Z_{eq2} & & \\ & & \ddots & \\ & & & Z_{eq16} \end{bmatrix} . \tag{2.55}$$

since the sixteen sensor – actuator systems are coupled only via the plate structure as shown in Figure 2.6.

If there is no control action, i.e. $\mathbf{f}_s(\omega) = \mathbf{0}$, then the transverse velocities at the centre positions of the panels can be calculated using (a) the dynamic equilibrium and (b) compatibility conditions at the junctions between the control units and the plate:

(a) dynamic equilibrium $\qquad \mathbf{f}_c = -\mathbf{f}_a$ (2.56)

(b) compatibility $\qquad \mathbf{v}_c = \mathbf{v}_a$ (2.57)

Therefore the velocities of the panel at the centre of the sensor-actuator units is found to be:

$$\mathbf{v}_c(\omega) = \left(\mathbf{I} + \mathbf{Y}_{cc}(\omega)\mathbf{Z}_{aa}(\omega)\right)^{-1}\mathbf{Y}_{cp}(\omega)\mathbf{f}_p(\omega) \ , \tag{2.58}$$

and the transverse velocities at the centre positions of the panels are given by

$$\mathbf{v}_e(\omega) = \mathbf{Y}_{ep}(\omega)\mathbf{f}_p(\omega) - \mathbf{Y}_{ec}(\omega)\mathbf{Z}_{aa}(\omega)\left(\mathbf{I} + \mathbf{Y}_{cc}(\omega)\mathbf{Z}_{aa}(\omega)\right)^{-1}\mathbf{Y}_{cp}(\omega)\mathbf{f}_p(\omega) \ , \tag{2.59}$$

As discussed in the previous case when the system is stable, if for each sensor–actuator pair a decentralized feedback control loop using the measured velocity $\dot{w}_{mes}(\omega) = T(\omega)\dot{w}_c(\omega)$ given by equation (2.46) is implemented with constant feedback gain, h, such that:

$$\mathbf{f}_s(\omega) = -\mathbf{H}(\omega)\mathbf{v}_m(\omega) \ , \tag{2.60}$$

and

$$\mathbf{v}_m(\omega) = \mathbf{A}(\omega)\mathbf{v}_c(\omega) \ , \tag{2.61}$$

where $\mathbf{H}(\omega)$ is given by equation (2.22) and

$$\mathbf{A}(\omega) = \begin{bmatrix} A_1 & & & \\ & A_2 & & \\ & & \ddots & \\ & & & A_{16} \end{bmatrix} . \tag{2.62}$$

with

$$\mathbf{v}_m(\omega) \equiv \begin{Bmatrix} \dot{w}_{m1}(\omega) \\ \dot{w}_{m2}(\omega) \\ \vdots \\ \dot{w}_{m16}(\omega) \end{Bmatrix} , \tag{2.63}$$

then, the velocities of the panel at the accelerometer positions is found to be:

$$\mathbf{v}_c(\omega) = \left(\mathbf{I} + \mathbf{Y}_{cs}(\omega)\mathbf{H}(\omega)\mathbf{A}(\omega) + \mathbf{Y}_{cc}(\omega)\mathbf{Z}_{aa}(\omega)\right)^{-1}\mathbf{Y}_{cp}(\omega)\mathbf{f}_p(\omega) \ . \tag{2.64}$$

and the transverse velocities at the centre positions of the panels are given by

$$\mathbf{v}_e(\omega) = \mathbf{Y}_{ep}(\omega)\mathbf{f}_p(\omega) - \left(\mathbf{Y}_{es}(\omega)\mathbf{H}(\omega)\mathbf{A}(\omega) + \mathbf{Y}_{ec}(\omega)\mathbf{Z}_{aa}(\omega)\right)\mathbf{G}^{-1}(\omega)\mathbf{Y}_{cp}(\omega)\mathbf{f}_p(\omega) \ , \tag{2.65}$$

where:

$$\mathbf{G}(\omega) = \mathbf{I} + \mathbf{Y}_{cs}(\omega)\mathbf{H}(\omega)\mathbf{A}(\omega) + \mathbf{Y}_{cc}(\omega)\mathbf{Z}_{aa}(\omega) \ . \tag{2.66}$$

In the following two subsections the kinetic energy of the panel and the total sound radiated per unit incident acoustic plane wave are plotted in a frequency range 0 to 1 kHz.

2.3 Simulations results

In this section the response of the panel and its sound radiation is discussed with reference to a range of feedback gains in the decentralised control loops. First, the analysis is carried out without considering the stiffness and mass effects of the piezoceramic patches and the dynamic and mass effects of the velocity transducers. Therefore the kinetic energy and sound power radiation, given by equations (2.25) and (2.30) have been calculated using equations (2.20) and (2.24) for the velocities of the radiating elements in the two cases of no control or active control.

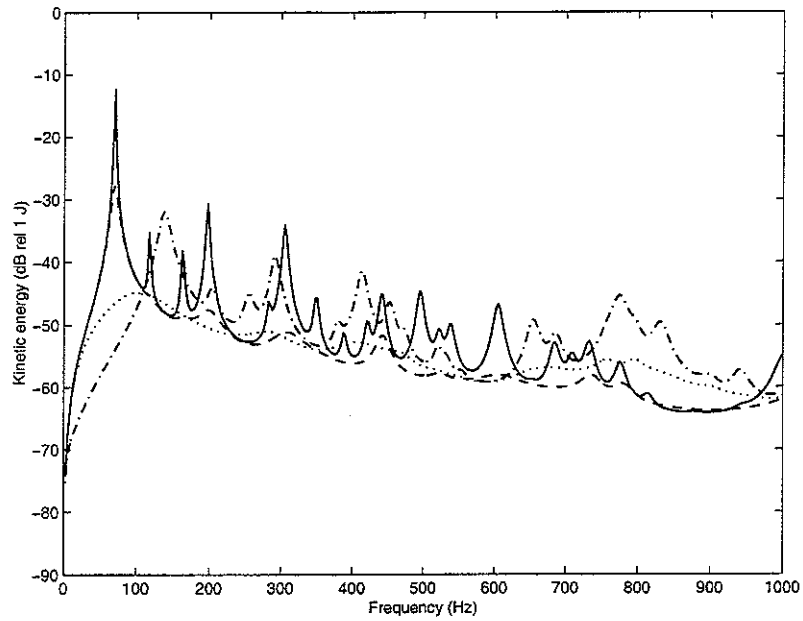

Figure 2.7: *Kinetic energy of the plane wave-excited panel when the dynamics of the sensor-actuator transducers are not taken into account with no control, solid, and with a 16 channel decentralised feedback controller using force actuators having a feedback gain of 10, dashed, 100, dotted, and 1000, dot-dashed.*

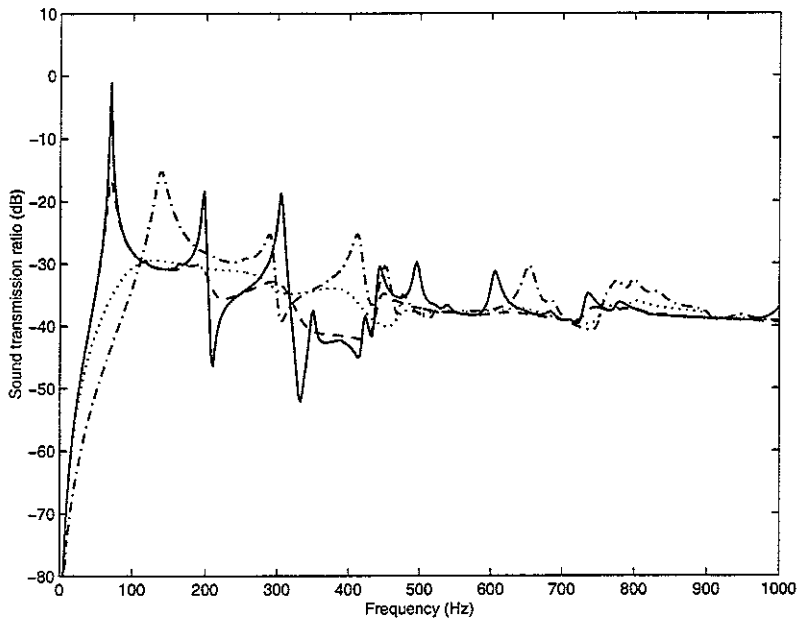

Figure 2.8: *Sound transmission ratio of the plane wave-excited panel when the dynamics of the sensor-actuator transducers are not taken into account with no control, solid, and with a 16 channel decentralised feedback controller using force actuators having a feedback gain of 10, dashed, 100, dotted, and 1000, dot-dashed.*

Figure 2.7 shows the total kinetic energy of the panel excited by the plane wave before control and when subject to control with sixteen individual single channel control system with various feedback gains, h. The modal response of the panel is clearly seen in the plot of the

kinetic energy against frequency before control, with the resonances associated with the first four modes, (1,1), (1,2), (2,1) and (1,3) occurring respectively at about 70, 118, 163 and 197 Hz. As the gains of the feedback loops are increased, the resonances in the response become more heavily damped, as one would expect with velocity feedback control. If the gains of the feedback loops are increased beyond a certain value, however, the closed loop response displays new peaks, such as that at about 140 Hz for example, which become more pronounced as the feedback gain is increased. As discussed by Elliott et al [15] these extra peaks are due to the resonances of the controlled dynamic system, which is effectively pinned at the sensor positions with high feedback gain. If feedback controllers having very high gain were used, the velocities at each sensor could be driven to zero and the physical result would be equivalent to that of perfect control of the sensor outputs with a feedforward control system, which could have been implemented if a suitable reference signal were available.

Figure 2.8 shows the ratio of the sound power radiated on one side of the panel to the incident sound power due to the plane wave excitation on the other side, which is termed the sound transmission ratio, T. Before control only the modes whose modal integers are odd radiate sound significantly at low frequencies and also anti-resonances appear, due to destructive interference between the sound pressures radiated by adjacent odd modes. As the feedback gains are increased, similar trends are observed in the reduction of the sound transmission ratio as in the reduction of the panel's kinetic energy, except that the new resonance at about 140 Hz has the greatest prominence, since its velocity distribution has the greatest net volume velocity.

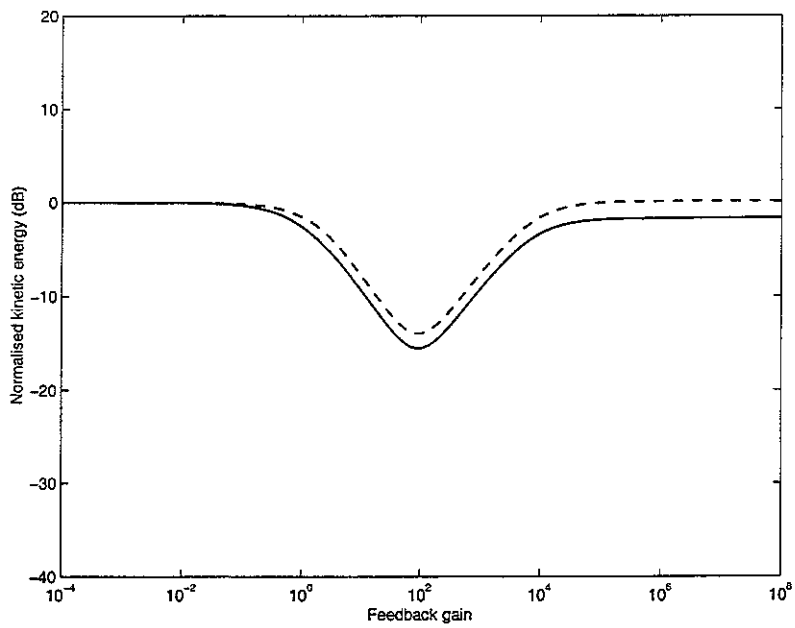

Figure 2.9: *Normalised kinetic energy level of the panel, integrated from 0 Hz to 1 kHz, plotted against the gain in the decentralised feedback controller, h, when the dynamics of the sensor-actuator transducers are not taken into account, solid, or are taken into account, dashed.*

When the panel's kinetic energy is integrated across the bandwidth shown in Figure 2.7 (up to 1 kHz) and this is plotted against feedback gain, a clear minimum of 15.8 dB is observed, for a gain of about 100, as shown in Figure 2.9. These velocities give rise to a poor estimate of

the panel's global response when the feedback gains are high enough for the new resonances to become significant. Figure 2.10 shows the variation with feedback gain for the sound transmission ratio integrated across this bandwidth, which corresponds to the total radiated sound power if the plate is subject to broadband excitation by a plane wave up to a frequency of 1 kHz, and this also has a minimum value of 10 dB for a feedback gain of about 100. At high feedback gains the overall sound power radiated after control is some 3.4 dB higher than it was with no control, because of the effect of the new resonance at about 140 Hz.

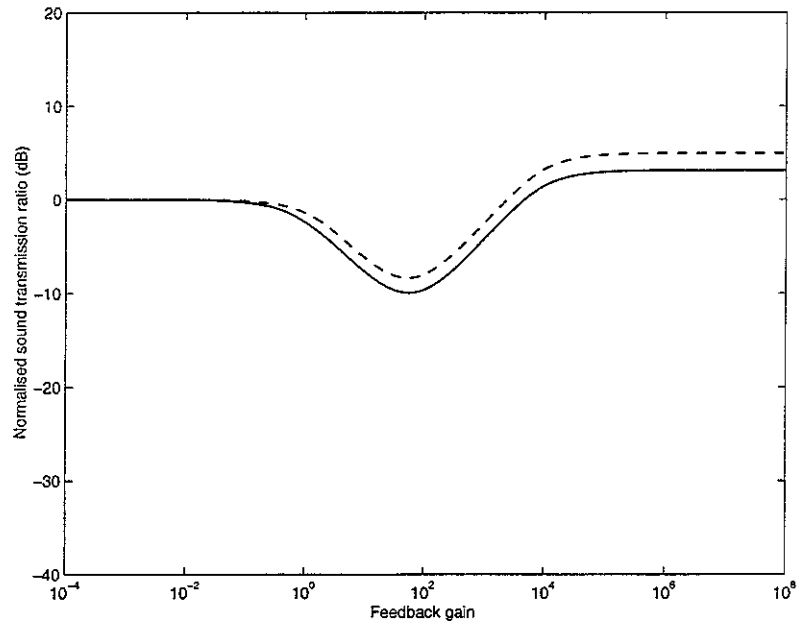

Figure 2.10: *Normalised sound transmission ratio level, integrated from 0 Hz to 1 kHz, plotted against the gain in the decentralised feedback controller, h, when the dynamics of the sensor-actuator transducers are not taken into account, solid, or are taken into account, dashed.*

In the second case studied, the stiffness and mass effects of the piezoceramic patches and the dynamic and mass effects of the velocity transducers have both been taken into account. Thus the kinetic energy and sound power radiation, given by equations (2.25) and (2.30) have been calculated using equations (2.59) and (2.65) for the velocities of the radiating elements in the two cases of no control or active control.

Figure 2.11 shows the total kinetic energy of the panel excited by the plane wave before control and when subject to control with sixteen individual single channel control system with various feedback gains, h. The modal response of the panel is slightly different to that shown in Figure 2.7 for the previous case. Indeed the resonances associated with the first four modes, (1,1), (1,2), (2,1) and (1,3) occur at slightly lower frequencies: 67, 115, 160 and 193 Hz. This is due to the added mass effects of the sensors and actuators transducers. The resonance due to the accelerometer occurs at too high frequency to be evident in this figure. As one would expect, also in this case, as the gains of the feedback loops are increased, the resonances in the response become more heavily damped and when the gains of the feedback loops are increased beyond a certain value, the closed loop response displays new peaks due to the additional constraints at the sensors positions.

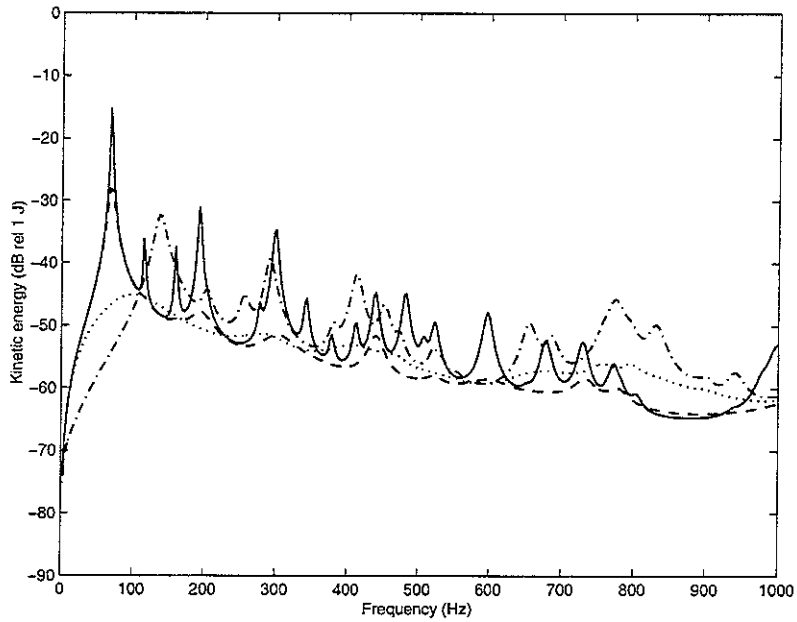

Figure 2.11: *Kinetic energy of the plane wave-excited panel when the dynamics of the sensor-actuator transducers are taken into account with no control, solid, and with a 16 channel decentralised feedback controller using force actuators having a feedback gain of 10, dashed, 100, dotted, and 1000, dot-dashed.*

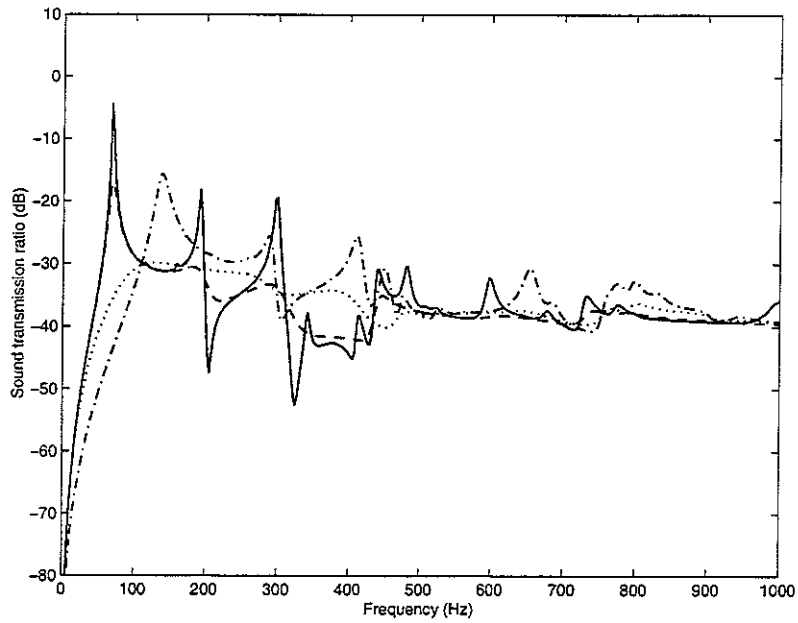

Figure 2.12: *Sound transmission ratio of the plane wave-excited panel when the dynamics of the sensor-actuator transducers are taken into account with no control, solid, and with a 16 channel decentralised feedback controller using force actuators having a feedback gain of 10, dashed, 100, dotted, and 1000, dot-dashed.*

Figure 2.12 shows for this second case the sound transmission ratio, T before control and when subject to control with sixteen individual single channel control system with various

feedback gains, h. As the feedback gains are increased, similar trends are observed in the reduction of the sound transmission ratio as in the reduction of the panel's kinetic energy.

The integrated panel's kinetic energy and integrated sound transmission ratio across the 0 to 1 kHz bandwidth are given by the dashed lines in Figures 2.9 and 2.10. Both curves have a similar trend to those found for the previous case. In this case, the sixteen decentralised control units seems to be slightly less effective since the maximum reduction of the kinetic energy and sound transmission ratio of the smart panel are of about 14 dB and 10 dB respectively. This is due to the fact that the control effectiveness in terms of reduction of the kinetic energy or sound transmission of the panel is limited to the same bottom floor as in the previous case. However the added mass of the sensors and actuators transducers have reduced the kinetic energy and sound transmission of the panel when there is no control by 2–3 dB. As a result the reductions of these two parameters generated by the control system are less pronounced than in the previous case.

3. OPEN LOOP SENSORS/ACTUATORS FREQUENCY RESPONSE FUNCTION

In this section the measured open loop frequency response functions of sensor–actuator pairs are analysed and contrasted with those derived from a simulation, in a frequency range up to 50 kHz. This study is focused on a pre-existing aluminium panel ($l_x \times l_y \times s = 278 \times 247 \times 1$ mm), which is glued on a rigid Perspex frame and it is equipped with five piezoelectric strain actuators patches[1] bonded on the bottom side of the panel ($a \times b \times c = 25 \times 25 \times 0.5$ mm). One of the actuators is positioned in correspondence of the centre of the plate, while the others are placed at the four corners so that the actuators' centres are distant 45 and 50 mm respectively from the short edge of the panel and from the long one.

A set of accelerometer has been placed in correspondence of the centre of each actuator, in such a way to have five co-locate sensor-actuator pairs. Both arrangements with the accelerometers on the upper side or the bottom side (i.e. on the same side of actuators) have been investigated.

In addition, a configuration based on a co-locate sensor with a force type shaker actuator has been considered, positioning the accelerometer on the bottom side of the panel while the shaker operates from the upper side.

The results presented in this section refer to measurements taken on the central sensor-actuator transducers and to the top right corner transducers, as shown in Figure 3.1. For each sensor-actuator pair, a set of open loop sensor-actuator frequency response functions have been measured with reference to different frequency ranges. Also, in order to highlight the sensitivity to geometrical offsets of the co-located positioning of the accelerometer with respect to the piezoelectric actuator or the mechanical shaker, other measurements were taken introducing a small offset in the placement of the sensor (about 5 mm, equal to the diameter of the sensor).

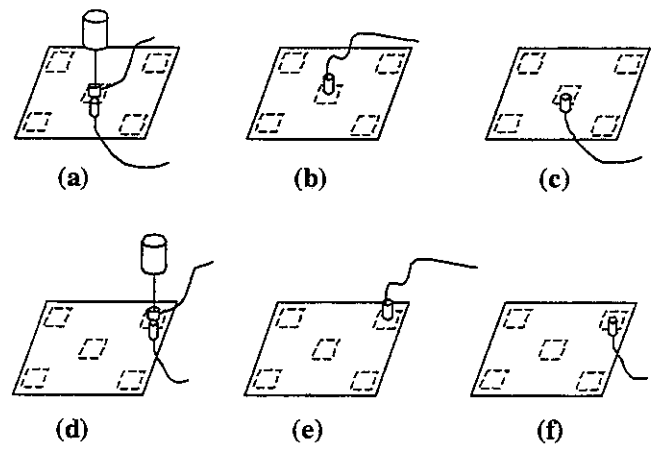

Figure 3.1: *The six sensor actuator configuration studied in this section.*

The simulated frequency response function has been derived analytically using the Euler–Bernoulli plate theory for bending vibration [23]. Although the plate was glued on a relatively rigid frame some degree of transverse rotation was in practice possible along the edges and thus the mathematical model has been formulated assuming the four edges of the panel to be simply supported.

[1] In the remaining part of the section this type of actuator will be abbreviate to "piezo actuator".

3.1 Measured sensors/actuators frequency response function

In this paragraph the measured sensors/actuators frequency response functions[2] of the central and top right pairs are reported and analysed. A spectral analyser of Advantest Corporation, model R9211B/C, has been used to measure the frequency response functions of the sensor/actuator pairs, i.e. the relationship between the velocity signal of the sensor and the disturbance signal applied to the actuator (piezo patch or shaker). High sensitivity ICP accelerometers of PCB Piezotronics, model 352C67, have been mounted on the panel at the measure positions and PCB integrators have been used to obtain the velocity signal from the accelerometers.

In the first part of the paragraph, the measured sensor/actuator frequency response functions of the central pair are analysed with reference to the different frequency ranges investigated: 0 to 1 kHz, 0 to 10 kHz and 0 to 50 kHz. Then, in the second part, the results concerning with the top right sensor/actuator pair are analysed in a frequency range of 1 kHz.

The solid lines in Figures 3.2 and 3.3 below show the measured frequency response functions of the velocity at the central sensor per unit excitation of the mechanical shaker and of the piezo actuator respectively, in a frequency range 0 to 1 kHz. Comparing the two figures, it can be seen that the shaker is more effective at low frequency than the piezo actuator, particularly in correspondence of the first resonance of the plate. Also, the thin lines in both figures show that, when there is a little off-set between the sensor and the actuator (about 5 mm, equal to the diameter of the sensor), the measured frequency response function is quite similar to that obtained with a perfectly collocated sensor/actuator pair.

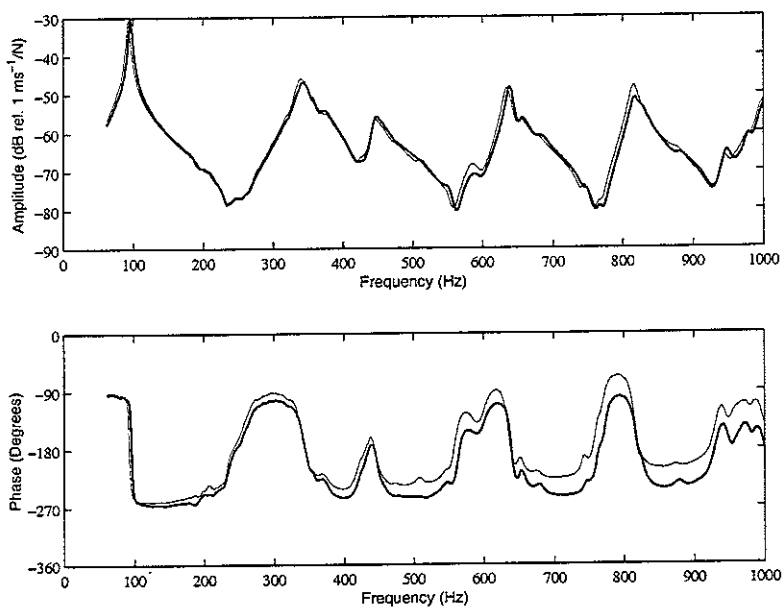

Figure 3.2: *Open Loop FRF (0-1 kHz) in the centre of the plate exciting with mechanical shaker (solid line) and with an off-set of 5 mm in the placement of accelerometer (faint line)*

[2] In the figure captions, frequency response function will be abbreviate to "FRF".

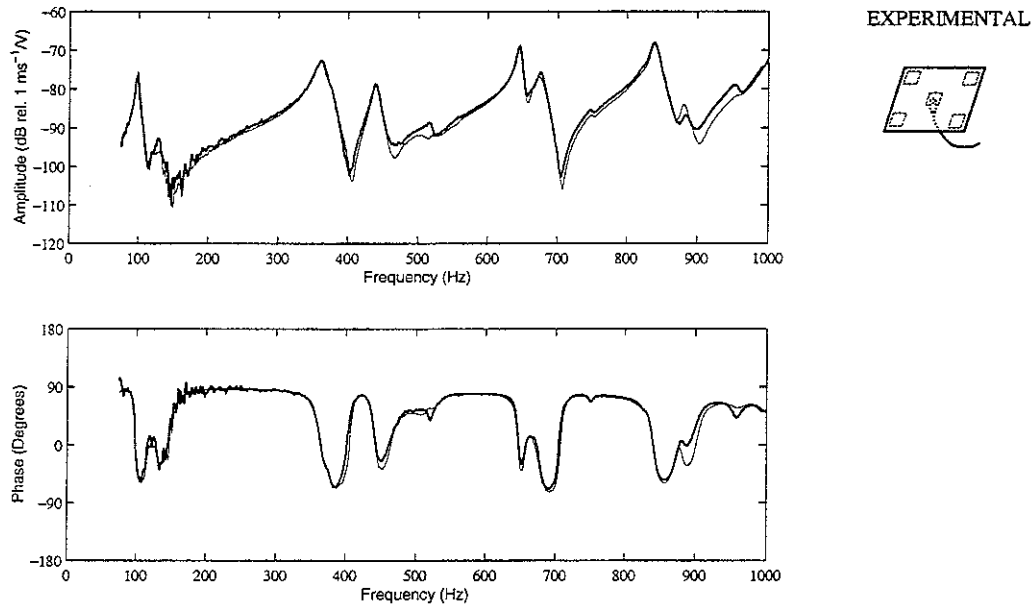

Figure 3.3: *Open Loop FRF (0-1 kHz) in the centre of the plate, exciting with piezoelectric actuator, with accelerometer on the bottom side (solid line) and with an off-set of 5 mm in the placement of accelerometer (faint line)*

In Figure 3.4 it is compared the measured frequency response functions of the velocity at the central sensor per unit excitation of the co-located piezo actuator, with the sensor on the upper side (solid line) and on the bottom side (faint line) in a frequency range 0 to 1 kHz. The two responses are very similar, except for a phase shift of 180 degrees, due to the opposite orientation of the sensors.

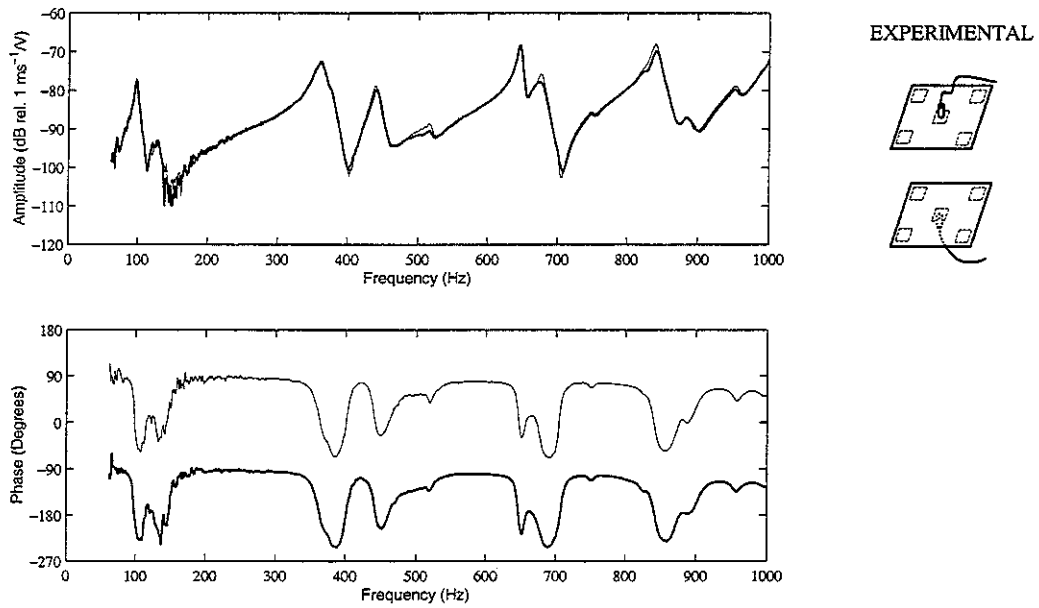

Figure 3.4: *Open Loop FRF (0-1 kHz) in the centre of the plate, exciting with piezoelectric actuator, with accelerometer on the upper side (solid line) and on the bottom side (faint line)*

The following two Figures 3.5 and 3.6 show the measured frequency response functions of the velocity at the central sensor per unit excitation of the mechanical shaker and of the piezo actuator respectively, in a frequency range of 10 kHz. It can be seen that the off-set in the placing of the sensor (faint line) has a marked effect in this frequency range: a difference of 10 dB appears in the both of frequency response function modules above 6 kHz while the phase plots have a shifting of about 50 degrees with respect to the original phase diagram.

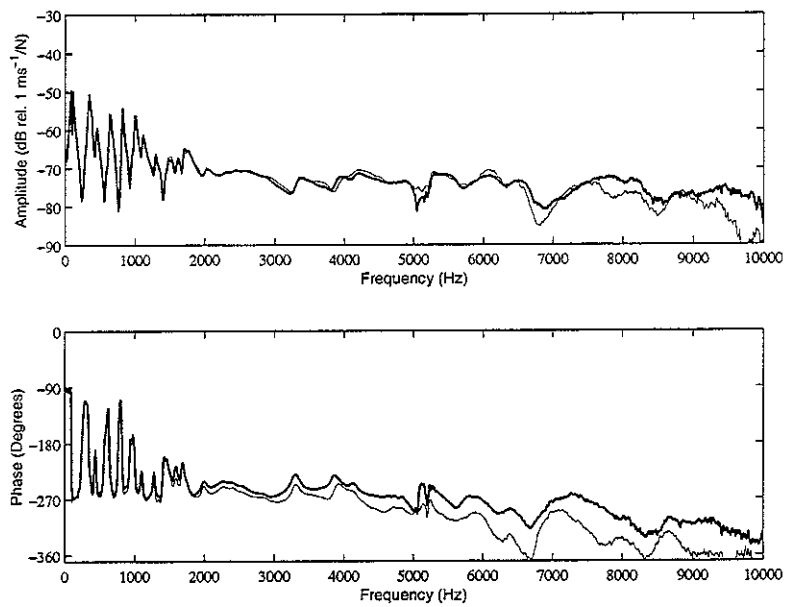

Figure 3.5: *Open Loop FRF (0-10 kHz) in the centre of the plate exciting with mechanical shaker (solid line) and with an off-set of 5 mm in the placement of accelerometer (faint line)*

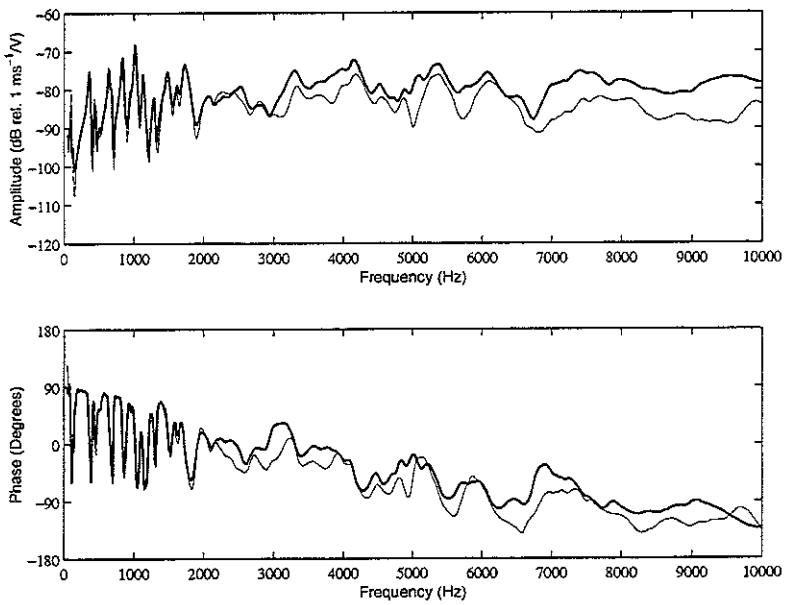

Figure 3.6: *Open Loop FRF (0-10 kHz) in the centre of the plate, exciting with piezoelectric actuator, with accelerometer on the bottom side (solid line) and with an off-set of 5 mm in the placement of accelerometer (faint line)*

Figure 3.7 shows a comparison between the measured frequency response function obtained with the sensor on the upper side (solid line) and on the bottom side (faint line) in a frequency range of 10 kHz. Even in this frequency range, the two functions taken with the sensor on either sides of the plate are quite similar, although a little difference in module appears above 7 kHz.

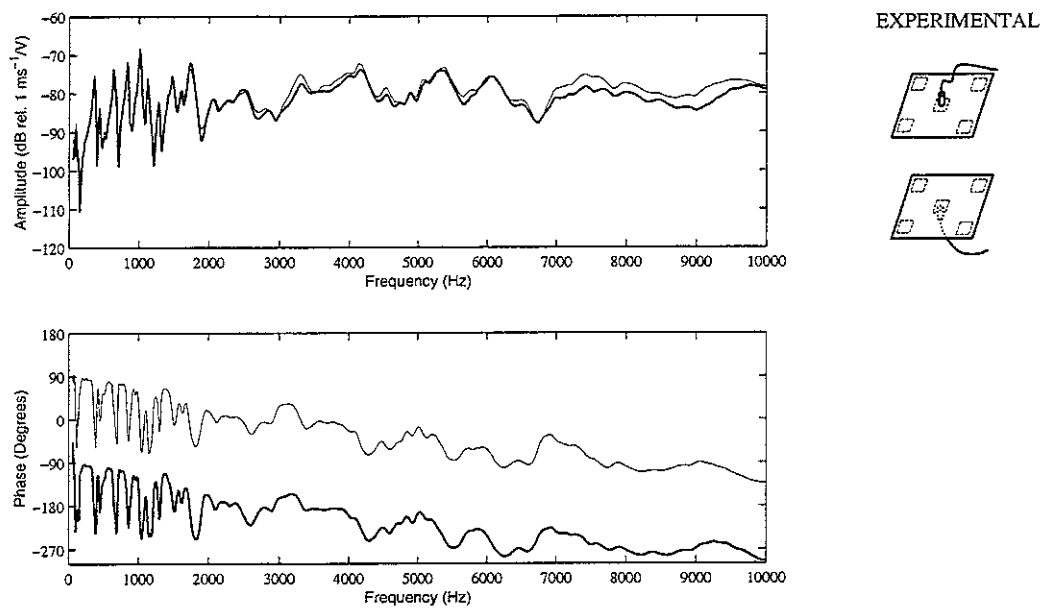

Figure 3.7: *Open Loop FRF (0-10 kHz) in the centre of the plate, exciting with piezoelectric actuator, with accelerometer on the upper side (solid line) and on the bottom side (faint line)*

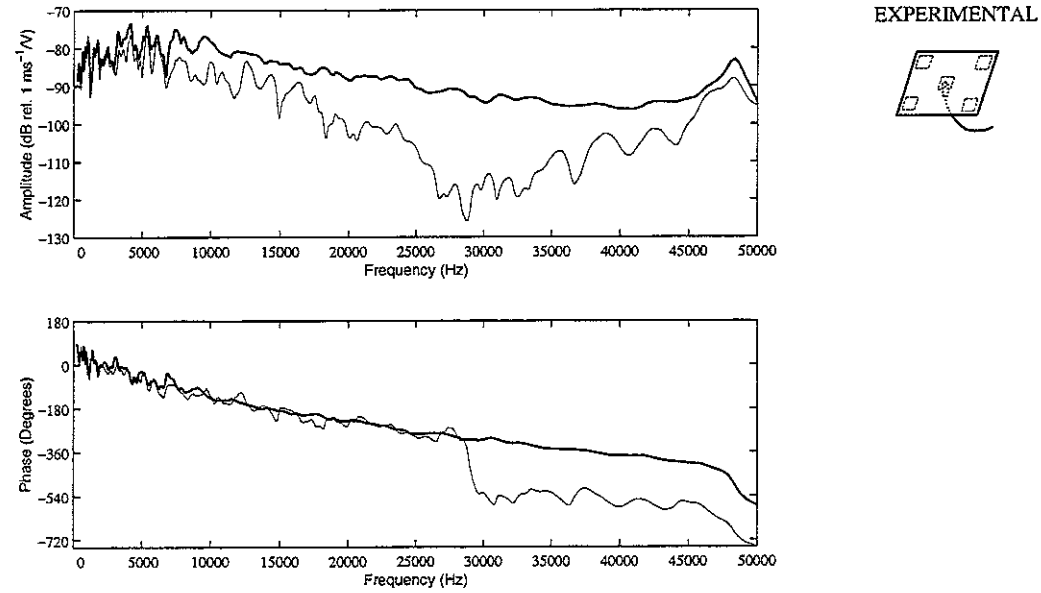

Figure 3.8: *Open Loop FRF (0-50 kHz) in the centre of the plate, exciting with piezoelectric actuator, with accelerometer on the bottom side (solid line) and with an off-set of 5 mm in the placement of accelerometer (faint line)*

Figure 3.8 shows the measured frequency response functions of the velocity at the central sensor per unit excitation of the piezo actuator, in a frequency range of 50 kHz. Considering this figure, it can be seen that in correspondence of about 48 kHz, the response is dominated by a significant peak, and the phase is affected by a shift of 180 degree. This phenomenon is probably due to the dynamics effects of the mounted accelerometer that, in a first instance, could be assumed to be a mass effect. Also, the thin lines show that, when there is an off-set of 5 mm between the sensor and the actuator, the module of the measured frequency response function presents a very accentuate trough between 25 and 45 kHz. In correspondence of this downturn, the phase is affected by a shift of about 300 degree. Above 16 Hz the bending wavelength is comparable to the dimension of the piezoelectric patch so that small offsets in the positioning of the accelerometer involve large variations of the measured signal that could even be of opposite phase for a left or right side offset or for a top or bottom offset.

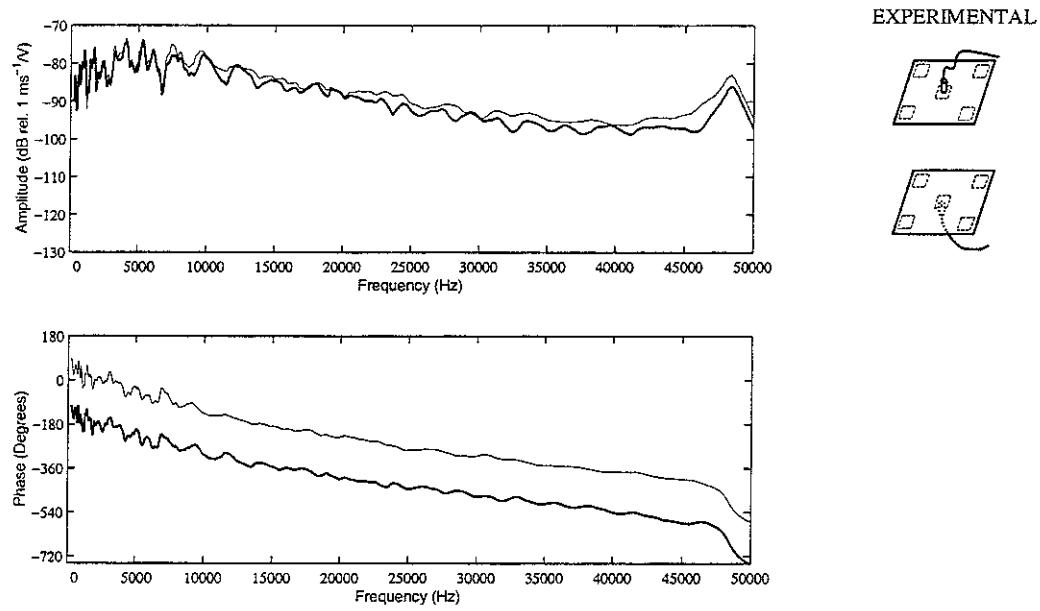

Figure 3.9: *Open Loop FRF (0-50 kHz) in the centre of the plate, exciting with piezoelectric actuator, with accelerometer on the upper side (solid line) and on the bottom side (faint line)*

Figure 3.9 shows a comparison between the measured frequency response function obtained with the sensor on the upper side (solid line) and on the bottom side (faint line) in a frequency range of 0 to 50 kHz. Again, the plot shows that no remarkable effects occur when the sensor is accurately positioned at the centre of the piezoelectric patch, there is just a little difference in the module of the response above 40 kHz.

In the second part of this section the measured frequency response functions between a collocated accelerometer and a piezoelectric strain actuator or shaker force actuator positioned at the top right corner of the panel in Figure 3.1 are studied. Only frequency response functions between 0 and 1 kHz are discussed since at higher frequencies the response is characterised by the same features found for the sensor actuator pairs positioned at the centre of the panel.

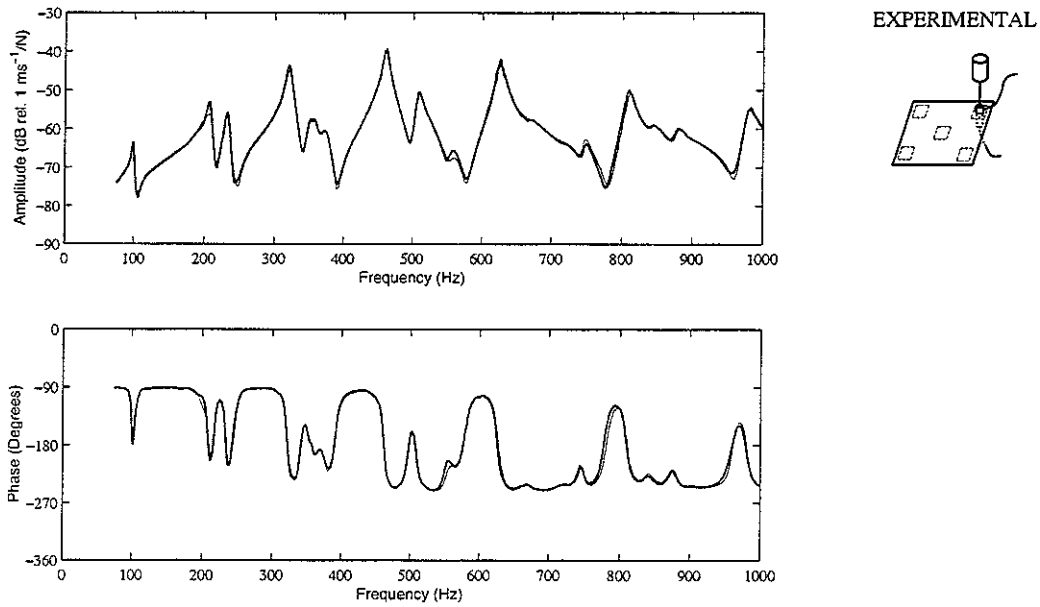

Figure 3.10: *Open Loop FRF (0-1 kHz) in a corner of the plate exciting with mechanical shaker (solid line) and with an off-set of 5 mm in the placement of accelerometer (faint line)*

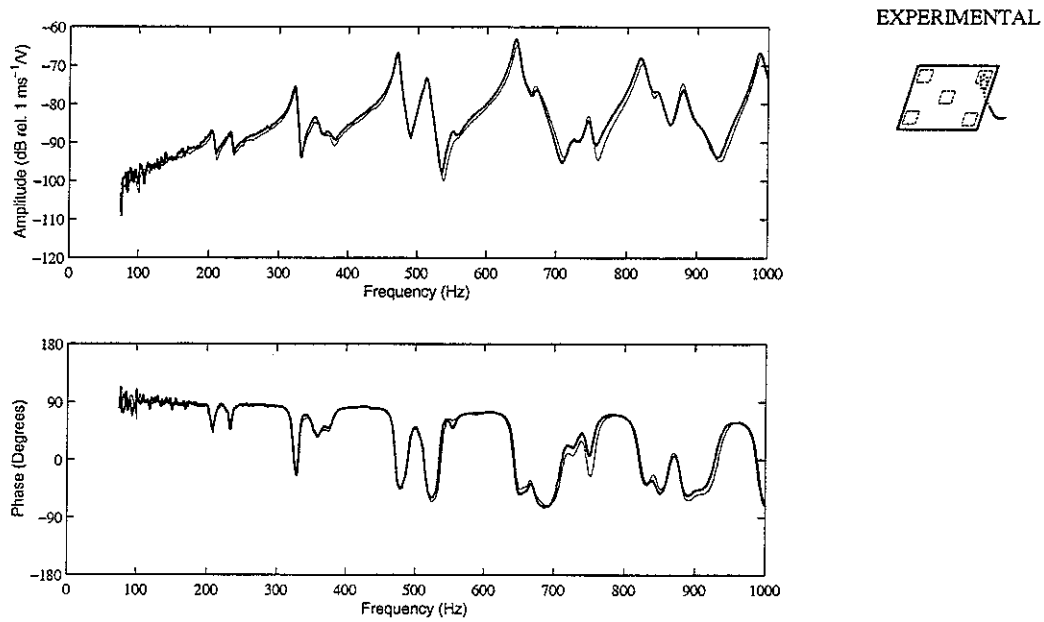

Figure 3.11: *Open Loop FRF (0-1 kHz) in a corner of the plate, exciting with piezoelectric actuator, with accelerometer on the bottom side (solid line) and with an off-set of 5 mm in the placement of accelerometer (faint line)*

Figures 3.10 and 3.11 show the measured frequency response functions of the velocity at the corner sensor per unit excitation of the mechanical shaker and of the piezo actuator respectively, in a frequency range of 0 to 1 kHz. Comparing these plots with those reported in Figures 3.2 and 3.3, it can be seen that the measured frequency response functions with the

top right corner transducers are characterised by few more resonance frequencies, which are not picked up by the sensor placed at the centre of the panel. Indeed, the sensor actuator pair positioned at the centre of the panel can not excite nor detect the low frequency modes which have nodal lines in correspondence to the axes of the plate. In fact the frequency response function of the velocity sensor and piezo actuator positioned at the top right corner of the panel is characterised by two resonances at 211 and 239 Hz as shown in Figure 3.10. In contrast, the frequency response function of the velocity sensor and piezo actuator positioned at the centre of the panel does not display those two resonances as can be seen in Figure 3.3.

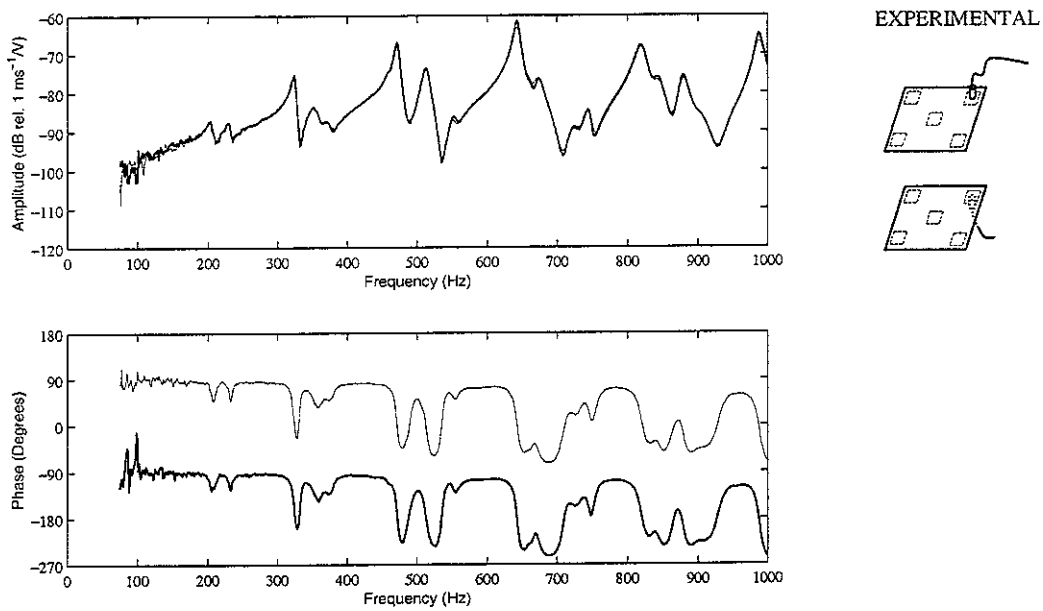

Figure3.12: *Open Loop FRF (0-1 kHz) in a corner of the plate, exciting with piezoelectric actuator, with accelerometer on the upper side (solid line) and on the bottom side (faint line)*

Figure 3.12 shows a comparison between the measured frequency response function when the piezo actuator is used, and the sensor is positioned on the upper side (solid line) or bottom side (faint line) of the panel, in a frequency range of 0 to 1 kHz. Also for the corner positioning of the transducers it is found that, apart form the phase chance of 180 degrees, there are no major differences between the two frequency response functions of the systems with the sensor either on top or bottom side of the plate.

3.2 Simulated sensor – actuator frequency response functions

In this section the frequency response functions of the central sensor-actuator pair of the smart panel under study have been numerically derived with reference to different frequency ranges: 0 tol kHz, 0 to 10 kHz and 0 to 50 kHz. Two types of collocated sensor-actuator pairs have been studied: first the velocity sensor-force actuator and second the velocity sensor-piezo patch strain actuator.

As described in section 2.1, the simulated frequency response functions have been derived analytically using the Euler–Bernoulli plate theory for bending vibration. Although the plate was clamped with a relatively rigid frame some degree of transverse rotation is in practice

possible along the edges and thus the mathematical model has been formulated assuming the four edges of the panel to be simply supported. Therefore, using the same notation presented in section 2.1 for equations (2.7) to (2.10), the sensor–actuator frequency response functions when the actuator is either the piezoelectric patch or the transverse force are given by the following two equations:

$$Y_{cs}(\omega)=\frac{\dot{w}_c(\omega)}{m_s(\omega)}=j\omega\sum_{m=1}^{M}\sum_{n=1}^{N}\frac{\phi(x_c,y_c)\left\{\int_0^{a_x}\psi^{(y)}(x_s,y_{s1})+\psi^{(y)}(x_s,y_{s2})dx+\int_0^{a_y}\psi^{(x)}(x_{s1},y_s)+\psi^{(x)}(x_{s2},y_s)dy\right\}}{\Lambda_{mn}\left[\omega_{mn}^2(1+j\eta_s)-\omega^2\right]}, \quad (3.1)$$

$$Y_{cs}(\omega)=\frac{\dot{w}_c(\omega)}{f_{zs}(\omega)}=j\omega\sum_{m=1}^{M}\sum_{n=1}^{N}\frac{\phi(x_c,y_c)\,\phi(x_s,y_s)}{\Lambda_{mn}\left[\omega_{mn}^2(1+j\eta_s)-\omega^2\right]}, \quad (3.2)$$

where $\dot{w}_c(\omega)$ is the transverse velocity at the centre of the sensor-actuator transducers, $m_s(\omega)$ is line-moment control excitations along the four edges of the piezoelectric actuator patch and $f_{zs}(\omega)$ is the transverse control force at the centre of the sensor actuator transducer pair. Also, for the simply supported panel, the natural frequencies and natural modes are given by

$$\omega_{fmn}=\sqrt{\frac{E_s h_s^2}{12\rho_s(1-\nu_s^2)}}\left[\left(\frac{m\pi}{l_x}\right)^2+\left(\frac{n\pi}{l_y}\right)^2\right], \quad (3.3)$$

$$\phi_{mn}(x,y)=\sin\frac{m\pi x}{l_x}\sin\frac{n\pi y}{l_y}. \quad (3.4)$$

Using the mode shapes given by equation (3.4) and remembering that

$$\psi_{mn}^{(x)}(x,y)=\frac{\partial\phi_{mn}(x,y)}{\partial x} \qquad \psi_{mn}^{(y)}(x,y)=-\frac{\partial\phi_{mn}(x,y)}{\partial y}, \quad (3.5a,b)$$

then equation (3.1) gives:

$$Y_{cs}^{p,q}(\omega)=-j\omega\sum_{m=1}^{M}\sum_{n=1}^{N}\frac{(k_m^2+k_n^2)}{k_m k_n}\frac{\phi(x_{ci},y_{ci})\cdot(\cos k_m x_{sq1}-\cos k_m x_{sq2})(\cos k_n y_{sq1}-\cos k_n y_{sq2})}{\Lambda_{mn}\left[\omega_{mn}^2(1+j\eta_s)-\omega^2\right]}, \quad (3.6)$$

where $k_m=m\pi/l_x$ and $k_n=n\pi/l_y$ are the m-th and n-th modal wavenumbers.

First of all, the case of velocity sensor-force actuator pair is analysed, with reference to the central position of the plate. The results of the simulated sensor/actuator frequency response functions between the velocity at the central error sensor per unit force excitation are reported in a frequency range of either 0 to 1 kHz (Figure 3.13) or 0 to 10 kHz (Figure 3.14). In those plots, the simulated frequency responses (solid line) are compared with the equivalent measured frequency response functions (faint line). The low frequency resonances of the

simulated and measured frequency response functions in Figure 3.13 are very close to each

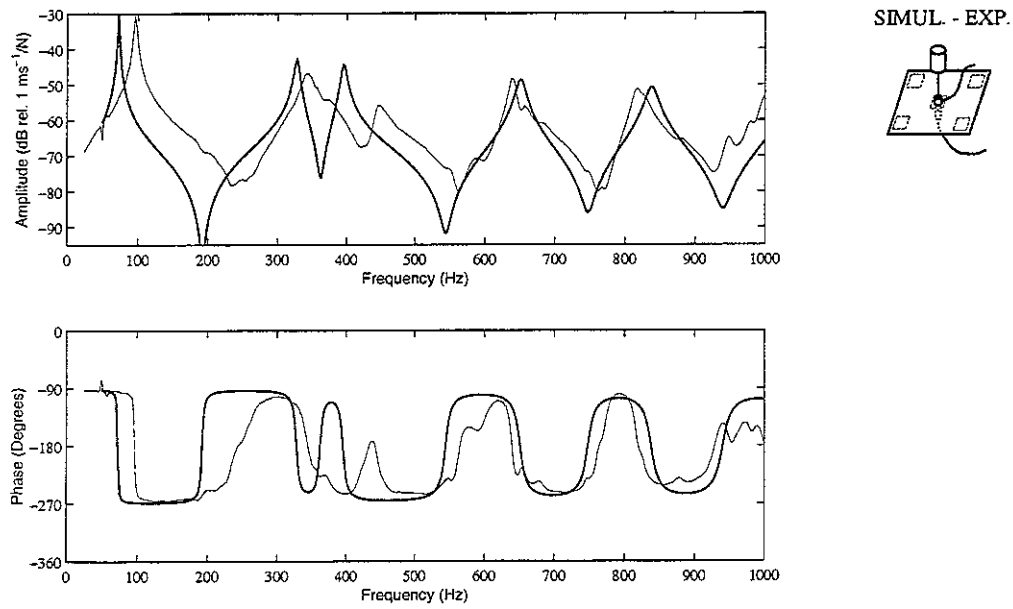

Figure 3.13: *Open Loop FRF (0-1 kHz) in the centre of the plate, exciting with mechanical shaker: simulated FRF (solid line) and measured FRF (faint line).*

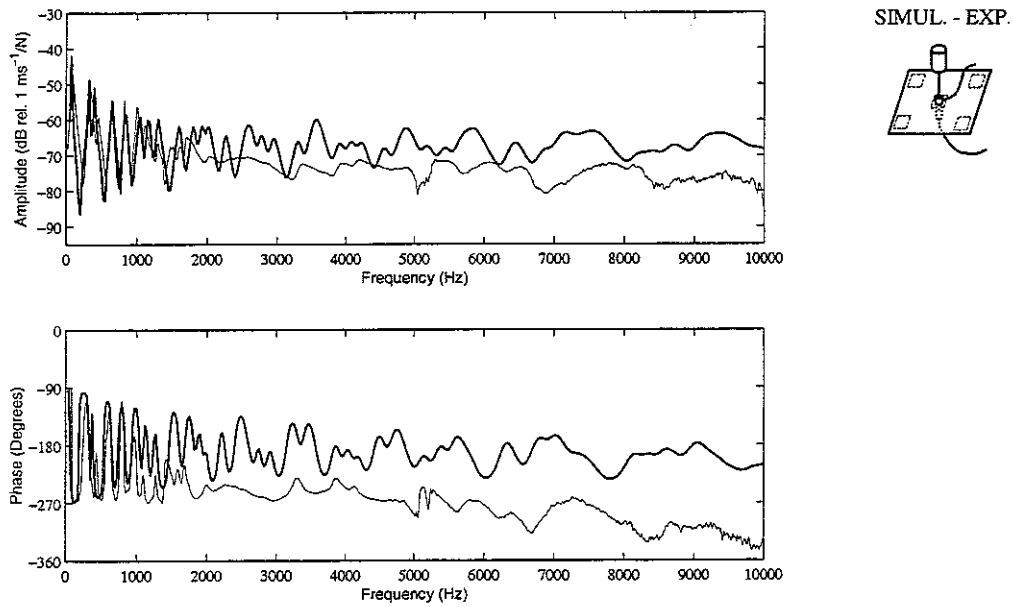

Figure 3.14: *Open Loop FRF (0-10 kHz) in the centre of the plate, exciting with mechanical shaker: simulated FRF (solid line) and measured FRF (faint line).*

other, which confirm that the choice of modelling the panel boundary conditions as simply supported is correct. However, considering Figure 3.14, it should be noted that the measured frequency response function presents a decrease trend of the module above 2 kHz, while, in the same frequencies interval, the simulated frequency response function presents an almost flat amplitude of the response. Also, above 2 kHz, the phase of the measured frequency

response function is characterised by a constant decrement that results to a phase lag of –360 Degrees at 10 kHz. In contrast the phase of the simulated sensor-actuator frequency response function is confined between –90 and –270 Degrees as expected for a perfectly collocated velocity sensor and force actuator pair (with the sensor mounted on the other side of the panel).

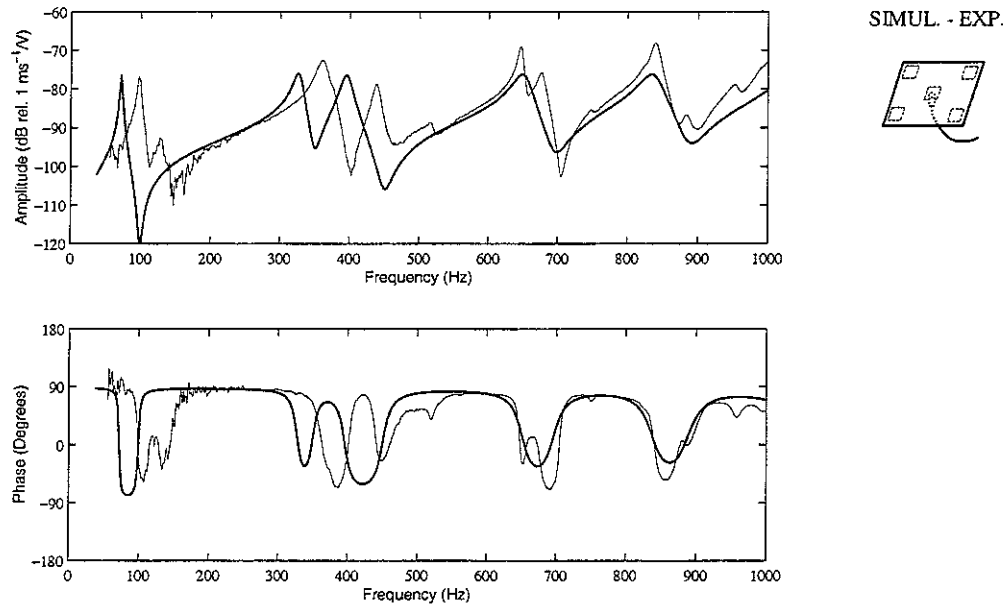

Figure 3.15: *Open Loop FRF (0-1 kHz) in the centre of the plate, exciting with piezoelectric actuator: simulated FRF (solid line) and measured FRF (faint line).*

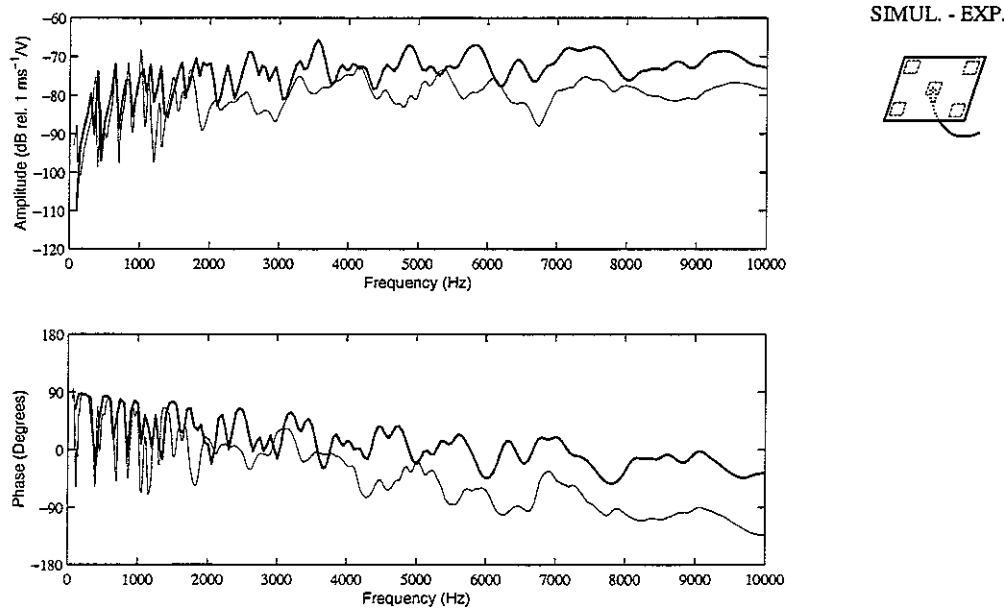

Figure 3.16: *Open Loop FRF (0-10 kHz) in the centre of the plate, exciting with piezoelectric actuator: simulated FRF (solid line) and measured FRF (faint line).*

The simulations for the sensor-actuator frequency response functions when the piezo actuator is used are reported in the next three plots for a frequency range between 0 and 1 kHz (Figure 3.15), between 0 and 10 kHz (Figure 3.16) and between 0 and 50 kHz (Figure 3.17). Also in these plots, the simulated frequency response functions (solid line) have been compared with the measured responses (faint line).

Comparing the experimental results with the numerical simulations reported in Figure 3.15, it can be seen that, as in the force excitation case plotted in Figure 3.13, the resonance frequencies of the simulated frequency response function are very close to those found in the measured frequency response function. In addition, as shown in Figure 3.16, the same divergence between the modules and phases of the measured and simulated frequency response function is found above 4 kHz. Indeed the measured frequency response function (faint line) presents a constantly decreasing trend of the modulus and phase above 4 kHz, while, in the same frequencies interval, the simulated frequency response function (solid line) presents an almost flat amplitude of the response and the phase is confined between -90 and -270 Degrees. This effect is even more clear in Figure 3.17 below where the measured and simulated frequency response function are plotted up to 50 kHz. The measured frequency response function is characterised by the constant decreasing trend of the modulus up to 45 kHz. At higher frequencies, the pot of the amplitude shows a clear pick at about 48 kHz. Also, in correspondence to this pick a phase lag of 180 Degrees is found. The simulated sensor-actuator frequency response function does not show this high frequency effect and the amplitude of the response remains flat and the phase decreases with a much lower rate than that of the measured one.

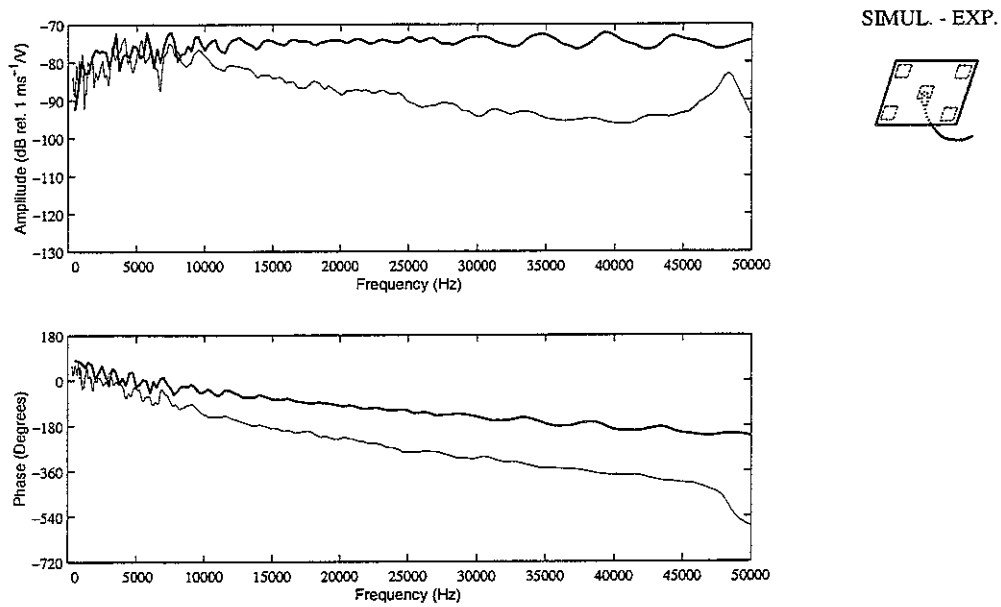

Figure 3.17: *Open Loop FRF (0-50 kHz) in the centre of the plate, exciting with piezoelectric actuator: simulated FRF (solid line) and measured FRF (faint line).*

In order to explain the discrepancies between the experimental and the numerical results emerged from the previous plots, the mass effect due to the presences of the sensor/actuator pairs and the accelerometer mounted frequency effect should be considered. These effects should not be negligible since the plate is comparably thin so that the mass effects of the actuator and sensor should be relatively important at higher frequencies.

3.3 Mass effect due to piezo and accelerometer

In order to consider the mass effect due to the presence of the piezo actuator and accelerometer sensor on the panel, the impedance of a point mass placed in the centre of the plate has been included in the numerical model. The point mass has been taken to be the mass of the piezo plus the mass of the accelerometer.
Using the principle of superposition, the translational velocity at the centre of the sensor-actuator transducers pair can be expressed as the summation of the vibrations generated by the control moments generated by the piezo actuator and by a point transverse force generated by the inertia effects of the masses of the actuator and sensor transducers so that:

$$\dot{w}_c(\omega) = Y_{cs}(\omega) m_s(\omega) + Y_{cc}(\omega) f_c(\omega) \tag{3.7}$$

where $Y_{cs}(\omega) = \dot{w}_c(\omega)/m_s(\omega)$ is the frequency response mobility between the velocity at the centre of the transducers pair, $\dot{w}_c(\omega)$, and the control moments of the piezo actuator, $m_s(\omega)$, and it is given by equation (3.6); $Y_{cc}(\omega) = \dot{w}_c(\omega)/f_c(\omega)$ is the driving point mobility between the velocity at the centre of the transducers pair, $\dot{w}_c(\omega)$, and the force transmitted by the masses of the piezo actuator, $f_c(\omega)$, and it is given by equation (3.2.). The force generated by the masses of the piezo actuator and accelerometer sensor, $m_{tot} = m_{piezo} + m_{accel}$, is given by

$$f_c(t) = m_{tot}\ \dot{w}_c(t) \tag{3.8}$$

so that, if the input impedance of the sensor actuator transducers is defined as follows

$$Z_M = \frac{f_c(\omega)}{\dot{w}_c(\omega)} = j\omega\, m_{tot} \tag{3.9}$$

then equation (3.7) becomes

$$\dot{w}_c(\omega) = \frac{Y_{cs}(\omega)}{1 - Y_{cc}(\omega) Z_M(\omega)} m_s(\omega) \tag{3.10}$$

so that the new transfer function of the velocity sensor and piezo actuator system is given by:

$$Y_{cs}(\omega) = \frac{\dot{w}_c(\omega)}{m_s(\omega)} = \frac{Y_{cs}(\omega)}{1 - Y_{cc}(\omega) Z_M(\omega)} \tag{3.11}$$

It must be underlined that this expression accounts only for the mass effects of the sensor and actuator transducers while the resonant effect of the accelerometer has been in this case neglected (see section 2.2).

In order to have a complete representation of the sensor actuator dynamics the accelerometer sensing frequency response function should also be taken into account. As described in more details in section 2.2, the output signal of an accelerometer is proportional to the velocity at the mounting position via the following frequency response function [22]:

$$T(\omega) = \frac{m_a}{k_a - m_a\omega^2 + jc_a\omega} = \frac{1}{\omega_n^2 - \omega^2 + j\xi 2\omega\omega_n} \quad . \tag{3.12}$$

where with m_a is the inertia mass of the accelerometer, k_a is the stiffness of the piezo transducer and c_a is the damping factor of the accelerometer, and thus $\omega_n = \sqrt{m_a/k_a}$ and ξ are respectively the natural frequency and damping ratio of the accelerometer.

The mounted frequency effect must be taken into to account to obtain a reasonable frequency spectrum of the simulated frequency response function above 40 kHz, where the measured response of the plate presents a significant peak of the module due to the resonant dynamics of the accelerometer. Indeed the sensitivity function of the accelerometer is constant up to about 30 kHz, and for higher values of frequency it is dominated by the mounted frequency resonance peak due to second order response of the mass-spring system used by the accelerometer to detect the acceleration at the mounting point.

Thus, using the formulations described above, both the mass effect and the sensing response effects have been included in the analytical model formulation of the sensor actuator frequency response function, which has been taken to be:

$$\overline{Y}_{cs}(\omega) = T(\omega)\, Y_{cs}(\omega) \tag{3.13}$$

with $Y_{cs}(\omega)$ given by equation (3.11) and $T(\omega)$ given by equation (3.12). The numerical results given by this new formula are plotted in Figures 3.18 to 3.20 for the frequency ranges of 0-1 kHz, 0-10 kHz and 0-50 kHz. In these plots, three curves are plotted: the simulated frequency response with no mass and sensitivity effects (solid line), with only mass effect (dashed line) and with both mass and sensitivity effects (faint line).

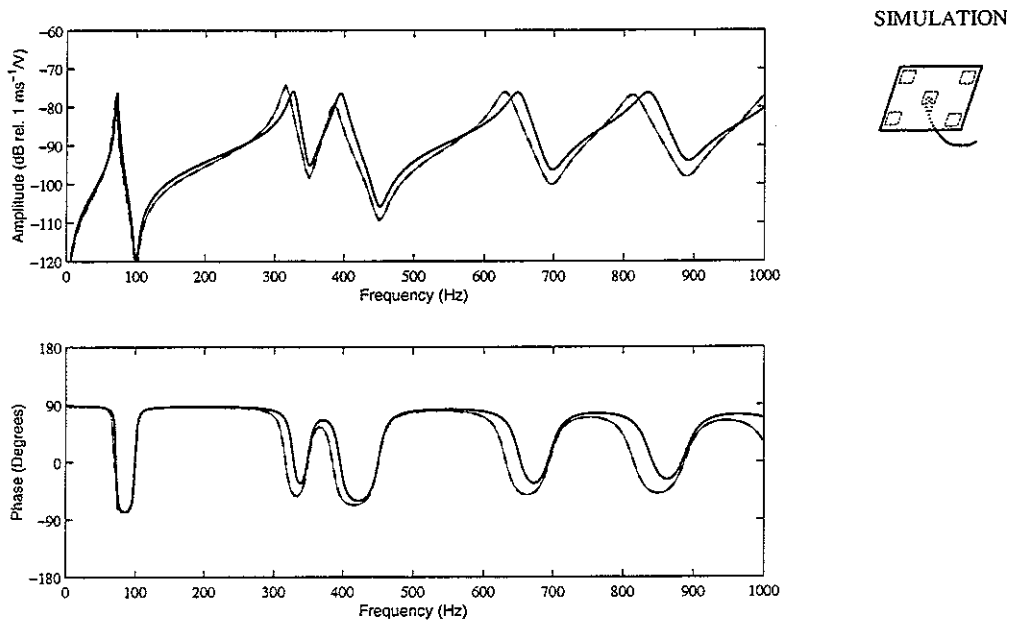

Figure 3.18: *Open Loop FRF (0-1 kHz) in the centre of the plate, exciting with piezoelectric actuator: simulated FRF with no effects (solid line), with mass effect (dashed line) and with resonance and mass effects (faint line).*

Figure 3.18 shows the simulation results in the first frequency range (0-1 kHz). It can be seen that, at low frequencies, the masses of the actuator piezoelectric patch and accelerometer sensor affects the dynamic of the panel with a small shifting to lower values of the resonance frequencies of the plate. Also, at low frequencies where the sensitivity function of the accelerometer is constant the faint line, which represents the frequency response function with mass and accelerometer sensitivity effects, overlaps the dashed line, which represents the frequency response function with only mass effect taken into account.

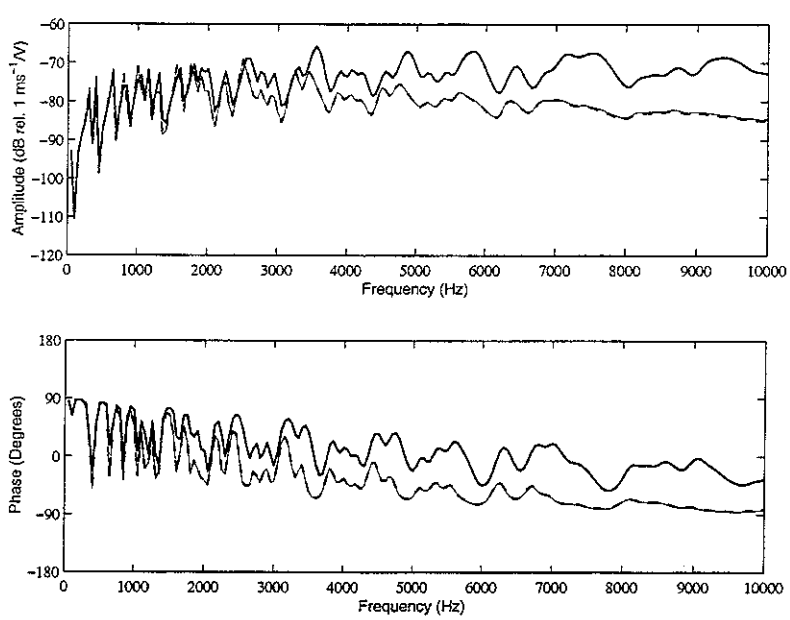

Figure 3.19: *Open Loop FRF (0-10 kHz) in the centre of the plate, exciting with piezoelectric actuator: simulated FRF with no effects (solid line), with mass effect (dashed line) and with resonance and mass effects (faint line).*

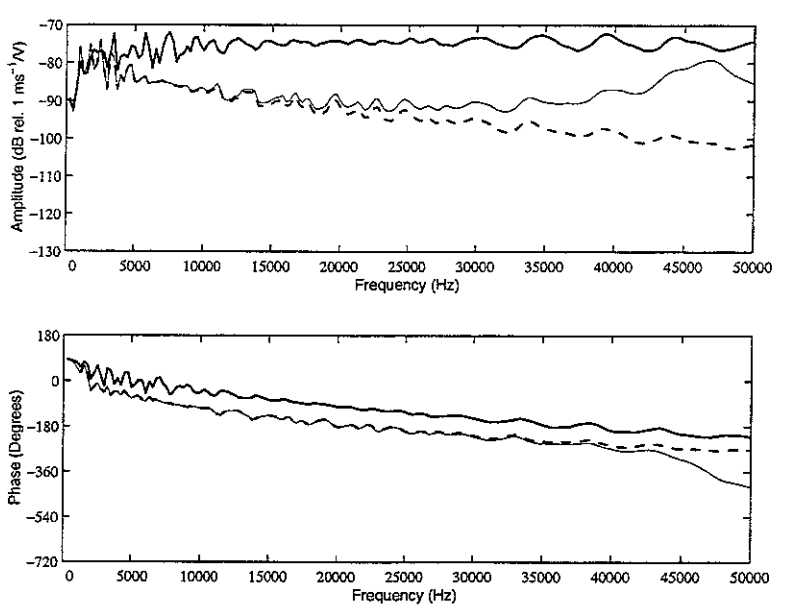

Figure3.20: *Open Loop FRF (0-50 kHz) in the centre of the plate, exciting with piezoelectric actuator: simulated FRF with no effects (solid line), with mass effect (dashed line) and with resonance and mass effects (faint line).*

In Figure 3.19 the three simulated frequency response functions are plotted in a frequency range of 0-10 kHz. In this case, the frequency response function with mass effect (dashed line) presents a decrease trend of the module above 4 kHz with respect to the original frequency response function which does not take into account the mass and accelerometer sensitivity effects (solid line). Thus, it is indeed the mass effect of the two transducers that produces the constant decreasing amplitude and constant phase lag of the measured sensor actuator frequency response function.

Figure 3.20 shows the three simulated frequency response functions within a frequency range of 0-50 kHz. The simulated frequency response function accounting only the transducers mass effect (dashed line) has a monotonic descent trend, while the frequency response function which takes into account for both the mass effects and accelerometer sensitivity (faint line) is characterized by a high frequency peak of the module with a relative phase shifting of 180 degrees in correspondence to the resonance frequency of the accelerometer as found with the measured frequency response function shown in Figure 3.17 (faint line).

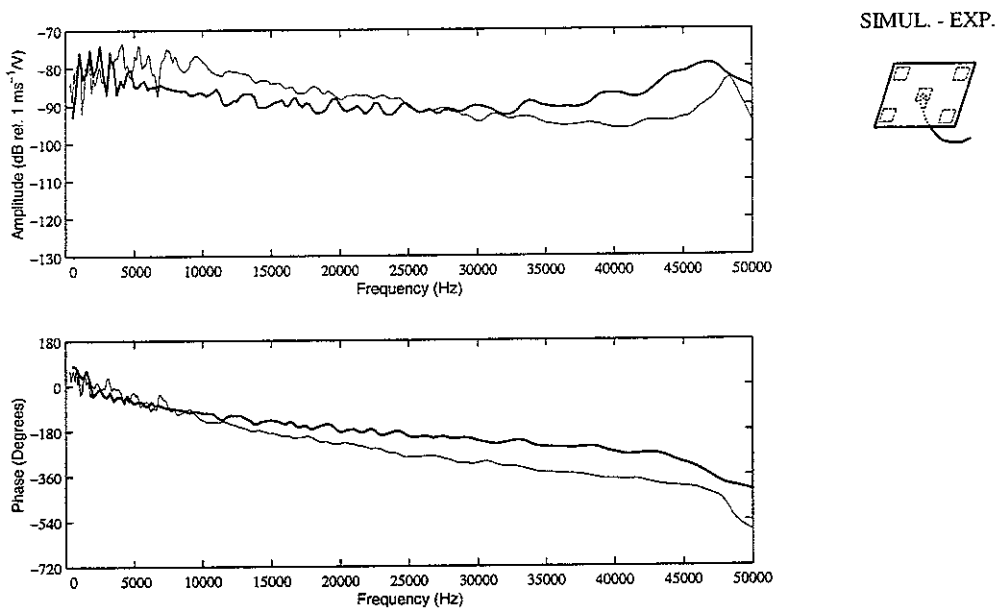

Figure 3.21: *Open Loop FRF (0-50 kHz) in the centre of the plate, exciting with piezoelectric actuator: simulated FRF with resonance and mass effects (solid line) and measured FRF (faint line).*

In Figure 3.21 the measured and simulated, including the transducers' mass and accelerometer's sensitivity effects, sensor-actuator frequency response functions are compared. Both the amplitude and phase plots of the measured (faint line) and simulated (solid line) frequency response functions agrees quite well and this confirms that the higher frequency constant decrement of the amplitude and constant phase lag are due to the mass effects of the sensor and actuator transducers while the pick with phase lag of –180 Degrees at about 48 kHz is due to the sensitivity function of the sensor that is affected by the mounted resonance frequency of the accelerometer.

The analysis of the measured and simulated sensor-actuator frequency response functions shows that the frequency responses are affected by an evident phase shift above 4 kHz as shown for example in Figures 3.17 and 3.21. This phase lag is due to the fact that the

accelerometer and the piezoelectric patch are not a truly collocated and dual sensor–actuator pair. The actuation mechanism of the piezoceramic actuator can be modelled as four lines of moments acting along the edges of the piezoelectric patch, with transverse point forces at the four corners [24]. The sensor is instead measuring the transverse velocity at the centre position of the actuator patch. There are thus two types of problems: the actuation and sensing are not collocated and also the moment actuation is not compatible to the linear transverse velocity sensing. Both effects contribute to determine a non–positive definite frequency response function at higher frequencies.

3.4 Effect due to piezo actuators dimensions

Intuitively, the non–collocated positioning effect found above 4 kHz for the accelerometer sensor piezo actuator frequency response function depends on the size of the actuator patch with reference to the bending wavelength vibration of the plate. The collocated positioning effect can therefore be extended to a wider frequency range by using a smaller piezoelectric patch actuator.

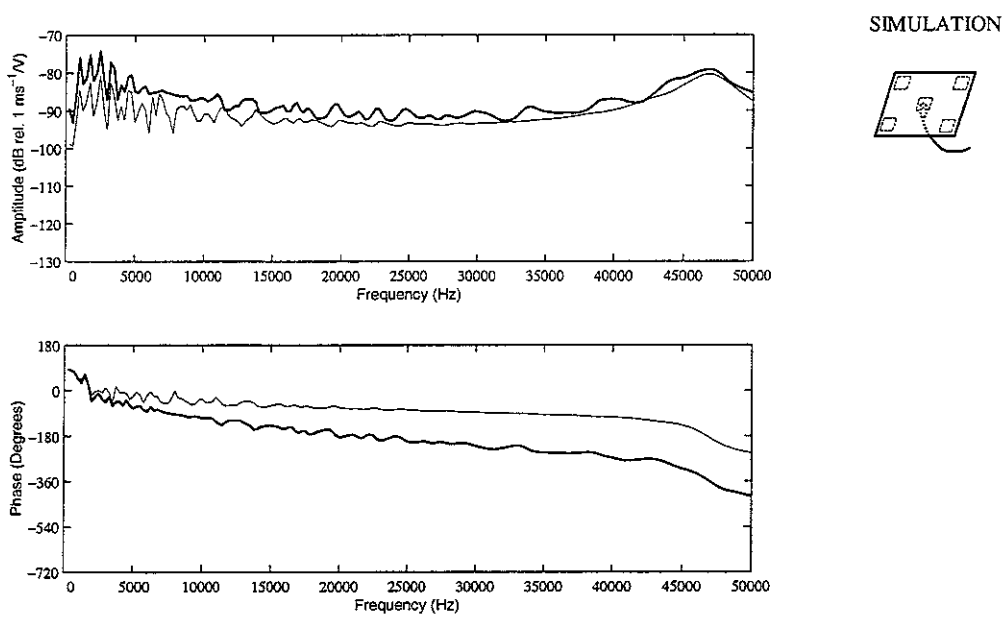

Figure3.22: *Open Loop FRF (0-50 kHz) in the centre of the plate, exciting with piezoelectric actuator: simulated FRF with standard size piezoelectric patch (solid line) and with smaller size patch (faint line).*

Figure 3.22 shows the predicted sensor–actuator frequency response functions with two different piezoelectric patch actuators, of dimensions 25×25 mm (solid line) and 12×12 mm (faint line). The bottom plot confirms that with a smaller patch the phase roll off is much lower than with the larger patch. Indeed by halving the size of the actuator the frequency response function is then found to be positive definite up to about 45 kHz. The draw back is that by reducing the size of the piezoelectric patch the control authority is also decreased. Therefore a compromise has to be found between the possibility of extending the minimum phase property of the sensor actuator frequency response function to higher frequencies and the required control authority to produce the desired control effect.

4. IMPLEMENTATION OF VELOCITY FEEDBACK USING ONLY ONE SENSOR/ACTUATOR PAIR.

In this section the control performances of a single control unit (accelerometer-feedback controller-piezo actuator) are numerically evaluated and contrasted with those obtained from experimental measurements. The control effectiveness of the control unit at the centre of the plate is assessed with reference to two types of primary excitations: first, the piezo actuator at the top right corner of the panel and second, a force type actuator provided by a mechanical shaker positioned close to the top right corner of the panel. Two control configurations have been investigated: a direct feedback of the velocity signal measured at the centre of the plate and a feedback of the same signal filtered through a compensator. The scheme reported in Figure 4.1 shows the experimental arrangement used for this study.

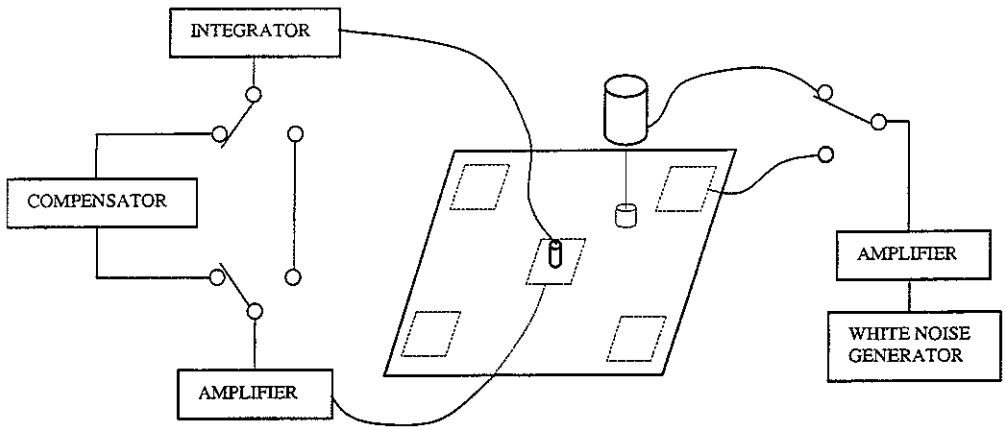

Figure 4.1:Experimental arrangement used for implementing single-channel feedback control system

The main features of velocity feedback control and about the design of a compensator for the implementation of a stable and robust feedback control loop are discussed in the next subsection. The following subsection is concerned with the experimental implementation of the single channel control system: the control effectiveness is analysed in terms of the frequency response function of the velocity at the error sensor per unit excitation of the primary disturbance source (i.e. the top right piezo or the shaker) in absence and in presence of the feedback loop.

4.1 Design of the compensator and simulation of the feedback control system

The design of the single channel velocity feedback control systems has been tested on the central sensor–actuator pair. Figure 4.2 shows the block diagram of the single–input single–output feedback control system that has been implemented. The total output velocity measured by the accelerometer sensor, $y(j\omega)$, is given by the vibration generated by the primary disturbance, $d(j\omega)$, and by the vibration generated by the control actuator which is set to be proportional, but with opposite phase, to the velocity measured by the accelerometer sensor itself. Therefore, for this feedback control scheme, the ratio between the error signal, $y(j\omega)$, and that of the primary disturbance, $d(j\omega)$, is given by [9]:

$$\frac{y(j\omega)}{d(j\omega)} = \frac{D(j\omega)}{1+G(j\omega)H(j\omega)} \tag{4.1}$$

where $G(j\omega)$ is the frequency response function between the sensor and actuator pair, $D(j\omega)$ is the frequency response function between the sensor and the excitation source (piezo actuator or shaker) and $H(j\omega)$ is the control function. In order to implement velocity feedback control, the control function is set to be a constant gain $H(j\omega) = h$ so that, provided the sensor actuator frequency response function is positive real, by increasing the gain h the ratio $y(j\omega)/d(j\omega)$ is always brought down.

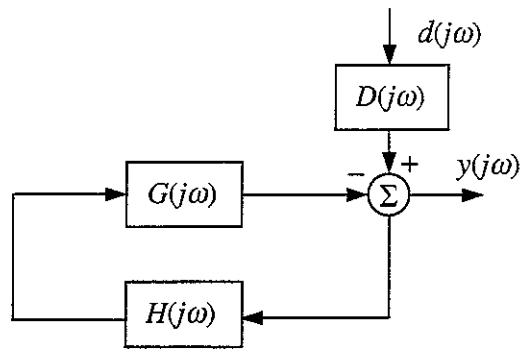

Figure 4.2: *Architecture of the closed loop system*

In order to guarantee an unconditionally stable control operability that gives reductions of vibration at all frequencies, the open loop Nyquist plot of the sensor–actuator frequency response function, $G(j\omega)$, should stay in the right–hand half of the complex plane for any frequency [9]. The results presented in previous section show that this is not the case for the sensor–actuator system under study. Indeed, the faint line in the bottom plot of Figure 3.9 indicates that above about 7.5 kHz the phase is greater than –90° and therefore the real part of the sensor–actuator frequency response function is negative as shown in the Nyquist plot in Figure 4.3. However the curve in Figure 4.3 does not encircle the Nyquist point $(-1,0)$ and therefore, for limited values of control gain, it would be possible to implement stable control. The gain margin for stable control is determined by the amplitude of the sensor–actuator frequency response function at frequencies between about 7.5 kHz and about 25 kHz. However it must be underlined that for those frequencies where the sensor–actuator frequency response function $G(j\omega)$ enters the circle of radius 1 and centre $(-1,0)$ in the Nyquist plot then the response at the error sensor is increased rather than diminished. In fact the denominator of equation (4.1) becomes smaller than 1 and therefore the ratio $y(j\omega)/d(j\omega)$ is raised rather than diminished. This phenomenon is known as control spillover and should also considered in the selection of the control gain and eventually in the design of a compensator circuit.

Considering in more details the Nyquist plot, it can be noticed that the mass effect of the piezoelectric patch actuator and accelerometer sensor that control the response between 7.5 kHz and 25 kHz, is working in favour of stability since it reduces the amplitude of the sensor–actuator frequency response function exactly in the frequency band for which the phase lag is between –90° and –270°, i.e. frequencies where the frequency response function

is negative definite. Also, the resonance effect due to the accelerometer sensor at around 45 kHz is, in this case, not compromising the stability of the control system since the sensor–actuator frequency response function between 35 kHz and about 45 kHz is positive definite, i.e. the phase is confined between –270° and –450°. However it must be said that this was not designed in advance and has come out from a fortunate choice of the mass of the piezoelectric patch and accelerometer.

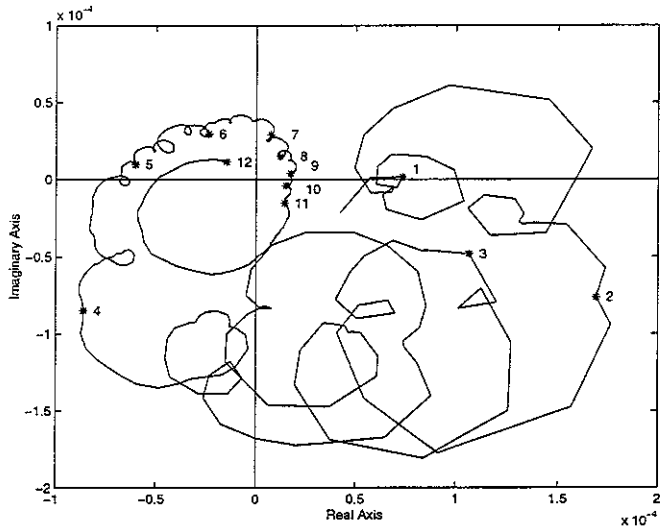

Figure4.3: *Nyquist plot (0-50 kHz) in the centre of the plate, exciting with piezoelectric actuator, with accelerometer on the bottom side: 1=2 kHz, 2=4 kHz, 3=5 kHz, 4=10 kHz, 5=15 kHz, 6=20 kHz, 7=25 kHz, 8=30 kHz, 9=35 kHz, 10=40 kHz, 11=45 kHz, 12=50 kHz*

To summarise, it is of crucial importance to carefully design the sensor–actuator system and making sure that low amplitudes of the frequency response function are given in frequency bands for which the frequency response function itself is negative definite. A safe approach would be to choose an accelerometer sensor with a relatively high mass effect and a very damped resonance frequency response. Also, as highlighted in section 3.4, the upper frequency limit for which the sensor–actuator frequency response function is positive definite can be increased by reducing the size of the piezoelectric patch actuator even though this has to be compromised with a decrement of the control authority.

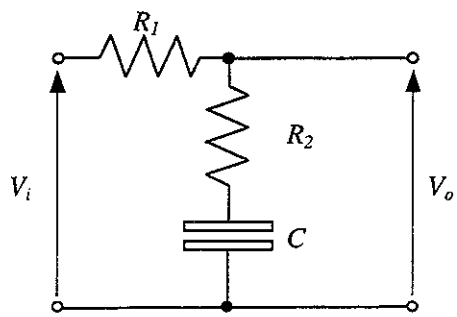

$$C(j\omega) = \frac{V_o(j\omega)}{V_i(j\omega)} = \frac{1 + j\omega R_2 C}{1 + j\omega(R_1 + R_2)C}$$

$$R_1 = 18\ \text{k}\Omega$$
$$R_2 = 1\ \text{k}\Omega$$
$$C = 15\ \text{nF}$$

Figure 4.4: *Phase lag compensator built in the feedback controller*

As discussed above, the test panel studied in this section is prone to generate instabilities in a frequency range between 7.5 kHz and 20 kHz (see can Figures 3.9 and 4.3). Therefore, in order to allow the implementation of the high gains required to get a good level of the panel's vibration reduction and consequently reduction of sound transmission through the panel, the phase–lag compensator with frequency response function $C(j\omega)$, shown in Figure 4.4, has been designed and implemented in the controller that is shown in Figure 4.5 below.

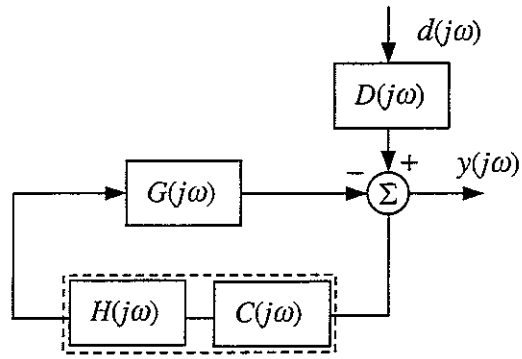

Figure 4.5: *Architecture of the closed loop system with compensator circuit*

The optimal values for the resistors and capacitor of the compensator circuit have been derived iteratively by simulating the closed loop sensor-actuator frequency response function,

$$T(j\omega) = H\, G_{ms}(j\omega)\, C(j\omega) \tag{4.2}$$

where H is a constant control gain, G_{ms} is the measured sensor actuator frequency response function and $C(j\omega)$ is the phase-lag compensator frequency response function which, according to the notation given in Figure 4.4, is given by:

$$C(j\omega) = \frac{V_o(j\omega)}{V_i(j\omega)} = \frac{1 + j\omega R_2 C}{1 + j\omega(R_1 + R_2)C} \tag{4.3}$$

The iterative procedure has brought to the design of a phase-lag compensator with the resistors and capacitor given in Figure 4.4. As shown in the figure below, this compensator has a relatively large amplitude roll off with a phase lag up to –65° at 3 kHz, which is recovered at higher frequencies.

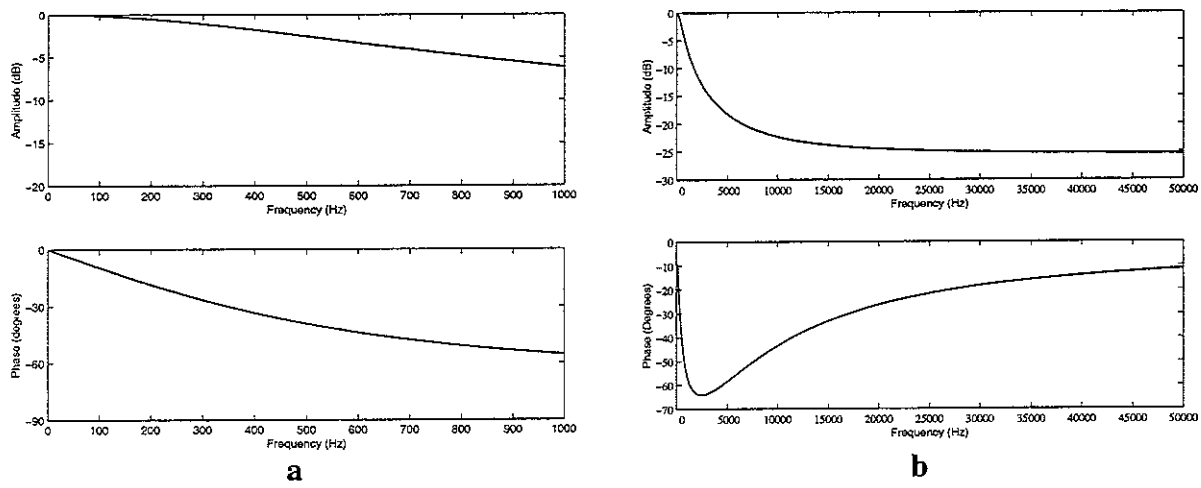

Figure 4.6: *Transfer function of the compensator in the range 0-1 kHz (a) and 0-50 kHz (b)*

The two plots shown in Figure 4.7 contrasts the Nyquist diagrams of the closed loop frequency response functions, obtained with a fixed gain using either a direct velocity feedback (Figure 4.7a) or velocity feedback with the compensator described above (Figure 4.7b). These two plots show that, for the chosen control gain, the direct velocity feedback control is close to the stability limit while the velocity feedback control using the compensator is far away from the instability point and gives a fairly good gain margin. Also, it is more robust since it guarantees reduction of the vibration at the control sensor position almost for all frequencies.

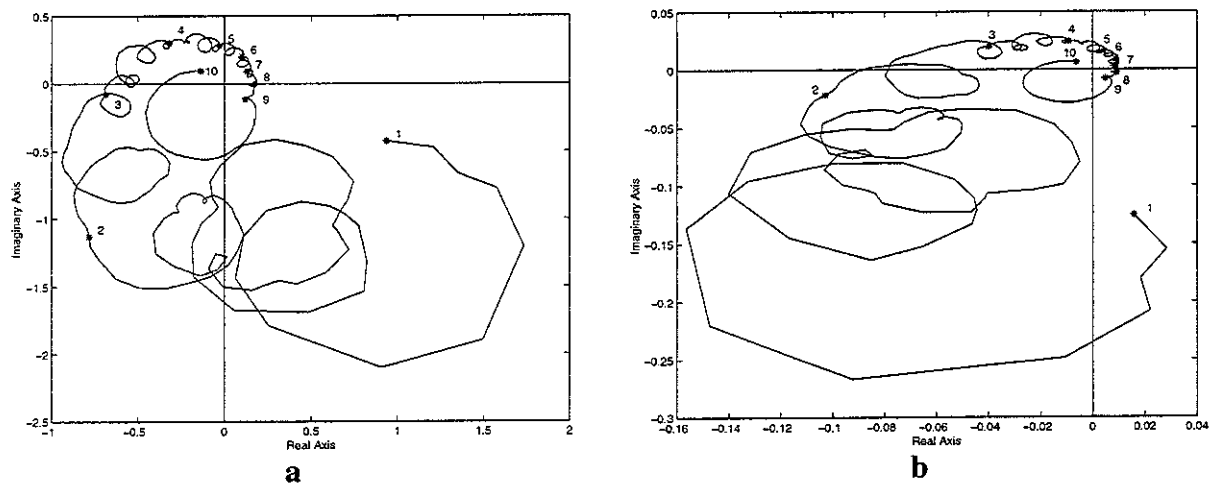

Figure 4.7: *Nyquist diagrams of the closed loop transfer function in presence of a direct feedback (a) and using a compensator (b):*
1=5 kHz, 2=10 kHz, 3=15 kHz, 4=20 kHz, 5=25 kHz,
6=30 kHz,7=35 kHz, 8=40 kHz, 9=45 kHz, 10=50 kHz

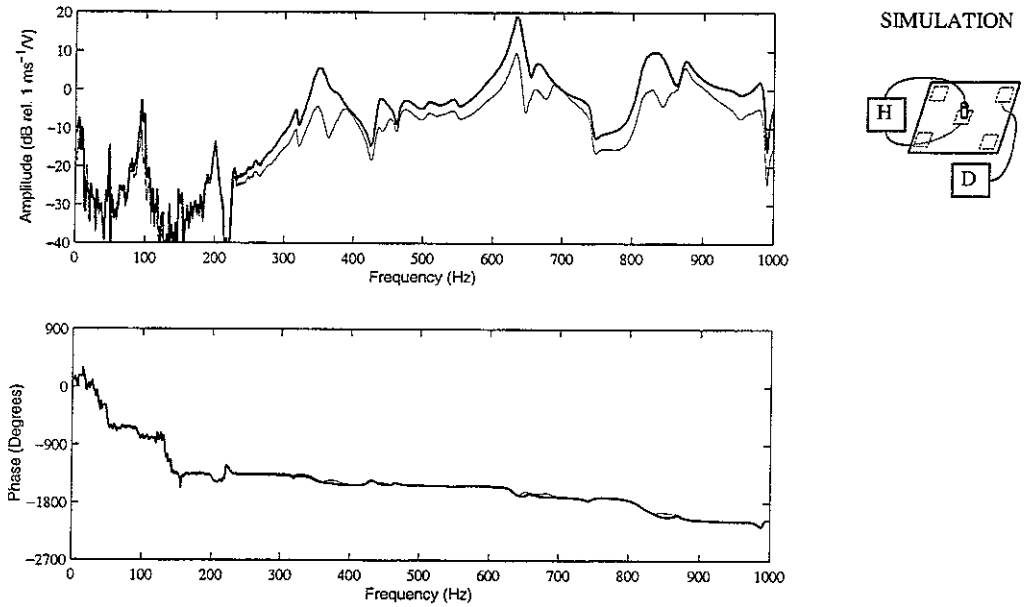

Figure 4.8: *Simulation of the feedback control effectiveness (0-1 kHz) in term of transfer function of the velocity at the error sensor per unit excitation of the top right piezo: no control system (solid line) and feedback control loop (faint line) using the compensator*

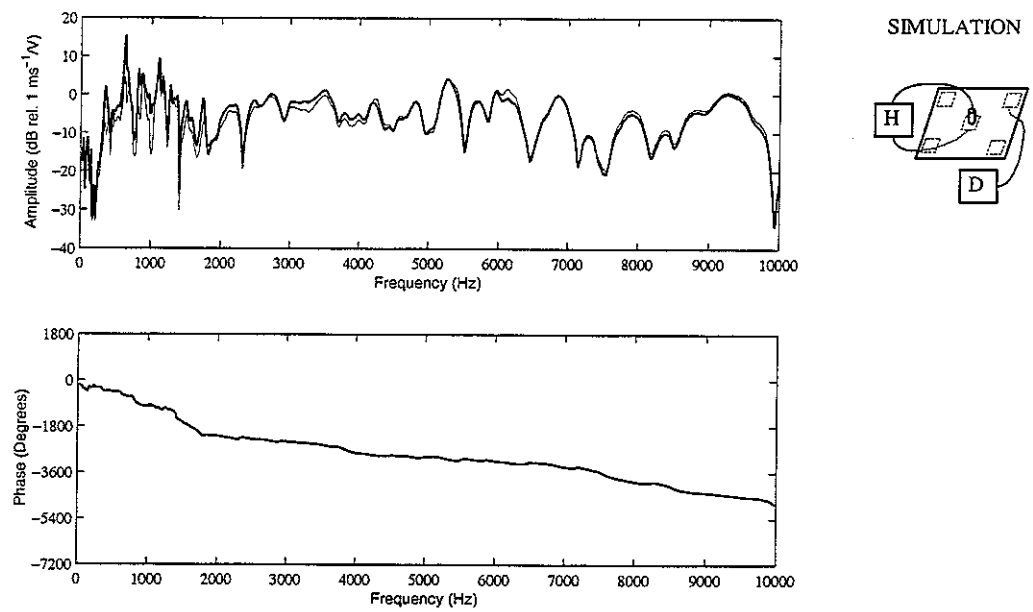

Figure 4.9: *Simulation of the feedback control effectiveness (0-10 kHz) in term of transfer function of the velocity at the error sensor per unit excitation of the top right piezo: no control system (solid line) and feedback control loop (faint line) using the compensator*

In order to assess the effectiveness of the velocity feedback loop with compensator a set of simulations have been produced for the system shown in Figure 4.1. Off line control experiments have been carried out using the measured sensor–control piezo actuator, $G(j\omega)$, (at the centre of the panel) and sensor–primary piezo actuator, $D(j\omega)$, (at the top right corner of the panel) frequency response functions. Figures 4.8 to 4.10 show for three frequency

ranges, 1 kHz, 10 kHz and 50 kHz, the velocity at the error sensor when the panel is excited by the top right piezo actuator (solid line) and when the velocity feedback control with compensator is implemented using the collocated piezo actuator at the centre of the panel. The solid line corresponds directly to the measured frequency response function $G(j\omega)$ while the faint line has been calculated with equation (4.1) assuming a constant gain H that could be implemented in practice and guarantees stability and some robustness in terms of overall control performance in all frequency range.

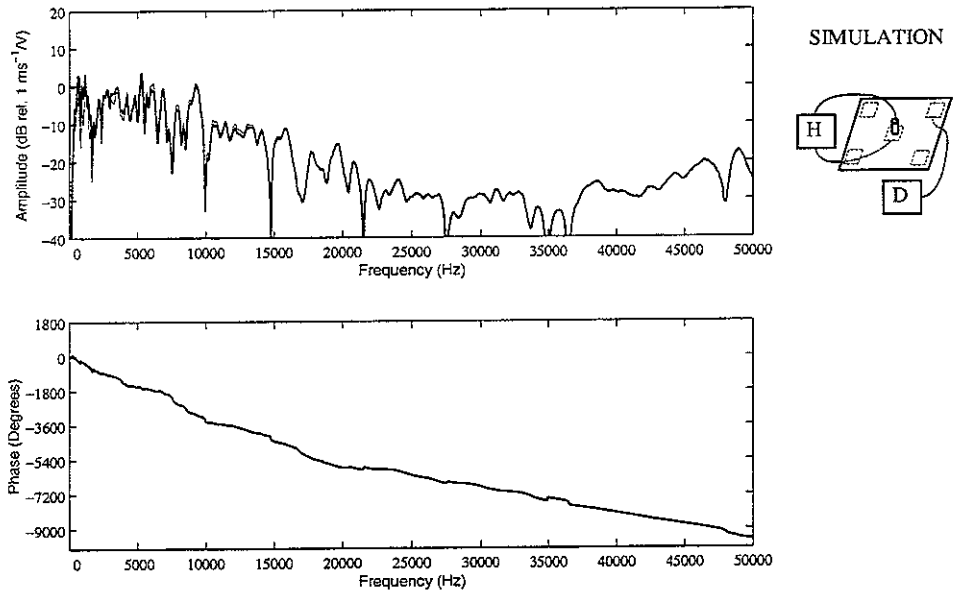

Figure 4.10: *Simulation of the feedback control effectiveness (0-50 kHz) in term of transfer function of the velocity at the error sensor per unit excitation of the top right piezo: no control system (solid line) and feedback control loop (faint line) using the compensator*

Figure 4.8, shows that above 200 Hz the vibration at the error sensor is reduced by 5 to 10 dB still keeping the control loop well within stability. At some narrow band frequencies the reduction can even be at the order of 15 to 30 dB. Figure 4.9 show that some reductions are achieved up to 4 Hz. At higher frequencies there is almost no control and instead for some frequency bands there could be some enhancement of the vibration at the error sensor. However, it must be noticed that in any case the level of the vibration at the error sensor above 10 kHz is in any case 10 or even 20 dB lower than that at low frequency and the increment of the vibratory effect is particularly small.

4.2 Implementation of velocity feedback control system

The on line control effectiveness of the control unit at the centre of the panel is now discussed. As shown in Figure 4.1 the panel has been excited either by the top right piezo actuator or by the top right shaker actuator. In order to implement the single channel feedback control system shown in Figures 4.5, the output signal of the accelerometer has been transformed to velocity with a B&K 2365 integrator, an high voltage power amplifier has been used to drive the piezo actuator and a analogue electrical circuit has been built to

implement the phase lag compensator shown in Figure 4.4. The control gain has been chosen in such a way as to guarantee stability and in such a way as to avoid excessive spillover phenomena at higher frequencies.
The Following three Figures, 4.11 to 4.13, show for three frequency ranges, 1 kHz, 10 kHz and 50 kHz, the velocity at the error sensor when the panel is excited by the top right piezo actuator (solid line) and when the velocity feedback control with compensator is implemented using the collocated piezo actuator at the centre of the panel. Figure 4.11 shows that the low frequency primary excitation provided by the primary piezo actuator is quite weak and so the plotted frequency response function is relatively disturbed up to about 600 Hz. However even for such a disturbed signal the control system provides a good reduction of about 10 dB of the first resonance pick at 100 Hz. The control effect is even better for the second resonance peak (400 Hz) and for the third (700 Hz), with reductions of about 15 dB and 30 dB respectively. Figure 4.12 shows that the chosen control gain provides good control results up to about 4 Hz while at higher frequencies, there is control spillover that produces a small amplification of the measured velocity by the control sensor of about 2 to 5 dB. However Figure 4.13 shows that the spillover phenomenon tends to disappear above 15 kHz. In conclusion the on line experiment using a collocated accelerometer sensor and piezo actuator transducers connected by a single channel analogue fixed gain feedback control system with the phase-lag compensator shown in Figure 4.4 has given good results at low frequency with reductions of up to 30 dB the resonance peak. The gain chosen gives some control spillover between 4 kHz and 15 kHz, which can produce vibration enhancement at the sensor position up to 5 dB.

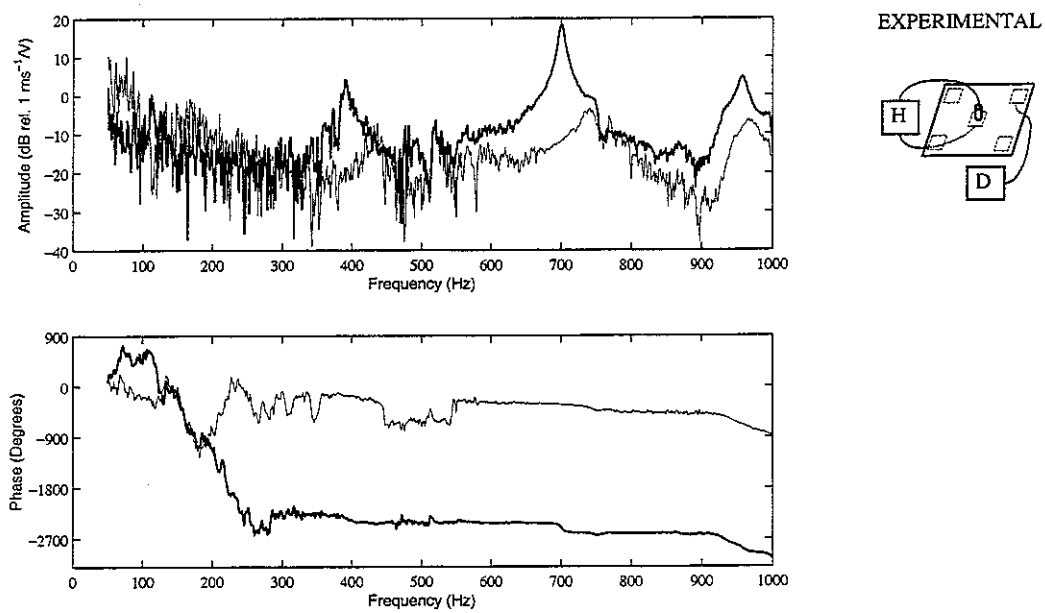

Figure 4.11: *Experimental feedback control effectiveness (0-1 kHz) in term of transfer function of the velocity at the error sensor per unit excitation of the top right piezo: no control system (solid line) and feedback control loop (faint line) using the compensator*

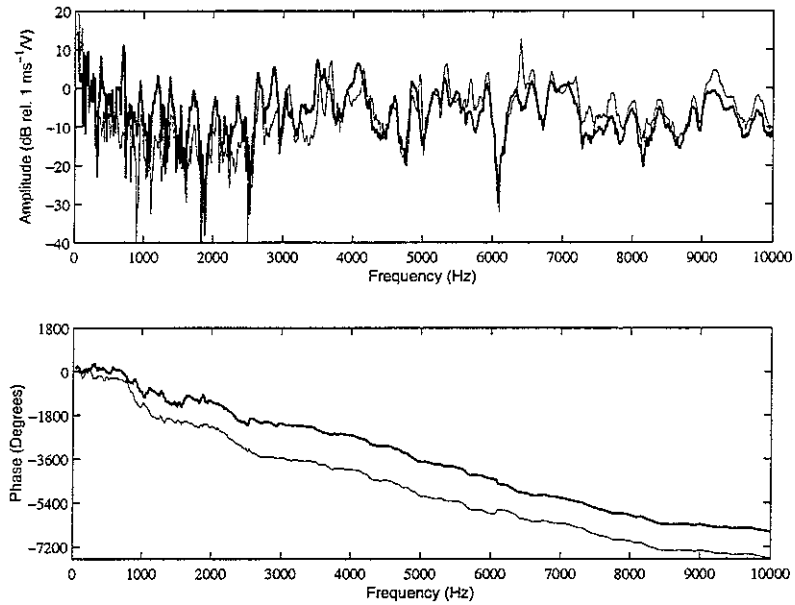

Figure 4.12: *Experimental feedback control effectiveness (0-10 kHz) in term of transfer function of the velocity at the error sensor per unit excitation of the top right piezo: no control system (solid line) and feedback control loop (faint line) using the compensator*

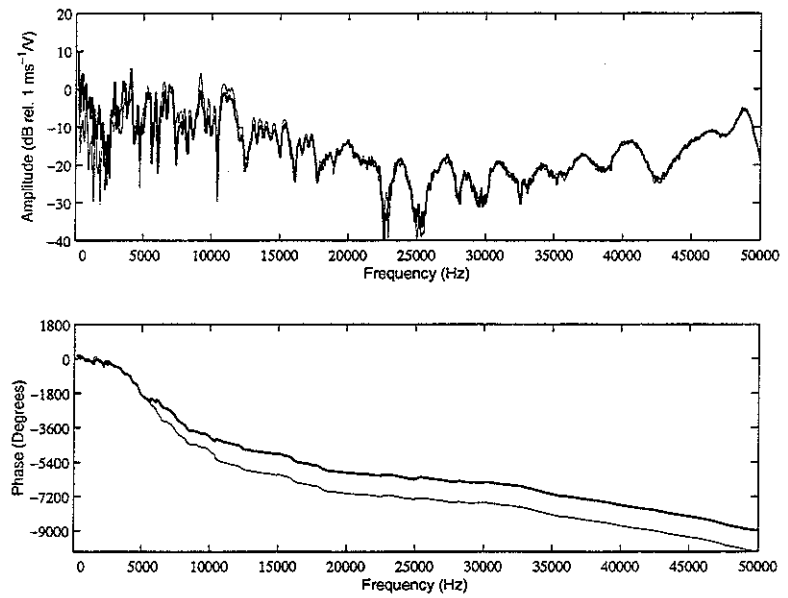

Figure 4.13: *Experimental feedback control effectiveness (0-50 kHz) in term of transfer function of the velocity at the error sensor per unit excitation of the top right piezo: no control system (solid line) and feedback control loop (faint line) using the compensator*

Figures 4.14 and 4.15 the show for two frequency ranges, 1 kHz and 10 kHz, the velocity at the error sensor when the panel is excited by the top right shaker actuator (solid line) and when the velocity feedback control with compensator is implemented using the collocated piezo actuator at the centre of the panel. The shaker force actuator is more effective at low frequencies so that all the low frequency natural modes are excited and the frequency

response function clearly shown a least five resonances below 700 Hz. With this type of excitation the control system is better exploited. Indeed the average vibration reduction at the sensor position is about 15 dB with maximum reductions up to 30 dB in correspondence to the seven resonance frequencies in the frequency band 0 to 1 kHz.

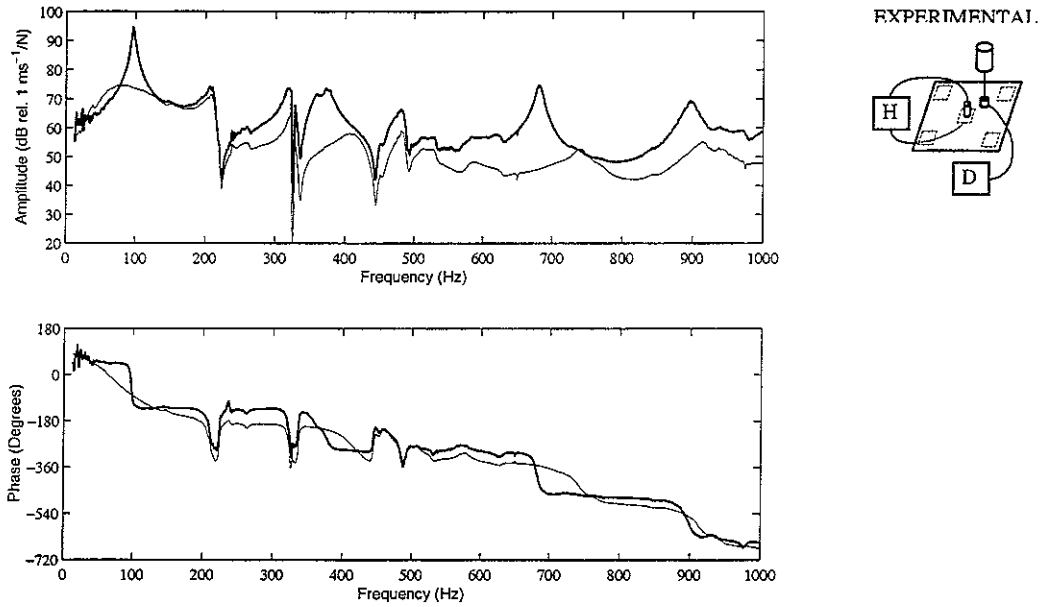

Figure 4.14: *Experimental feedback control effectiveness (0-1 kHz) in term of transfer function of the velocity at the error sensor per unit excitation of the mechanical shaker: no control system (solid line) and feedback control loop (faint line) using the compensator*

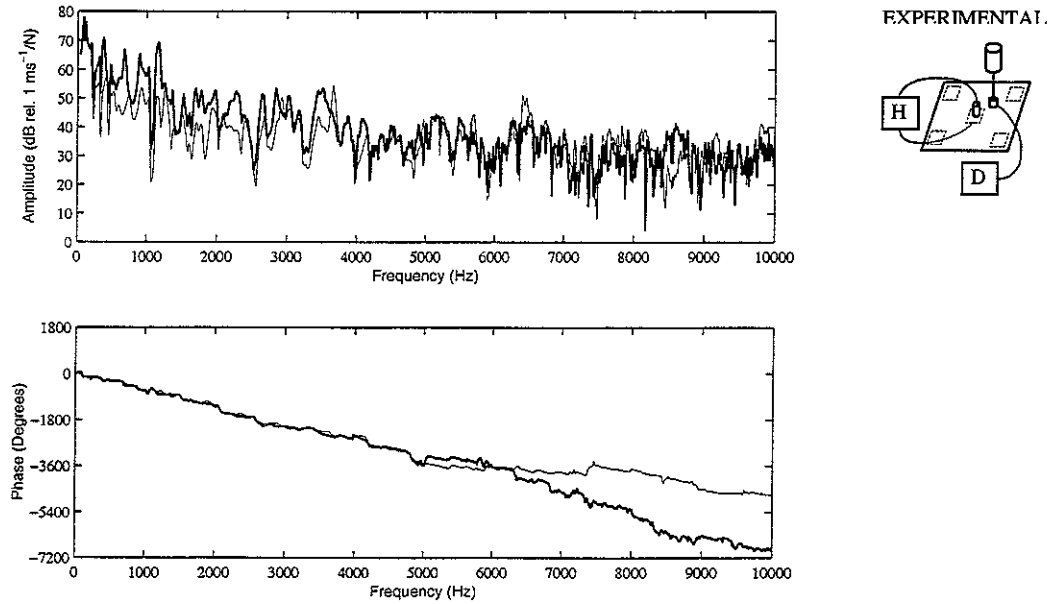

Figure 4.15: *Experimental feedback control effectiveness (0-10 kHz) in term of transfer function of the velocity at the error sensor per unit excitation of the mechanical shaker: no control system (solid line) and feedback control loop (faint line) using the compensator*

The plot in Figure 4.15 shows that, also in this case, the control action is effective up to 4 kHz and some control spillover effects are visible beyond 6 kHz. However the vibration level above 4 kHz is in any case some 20 dB lower because of the poor actuation effectiveness of the primary shaker at higher frequencies. Indeed the third plot up to 50 kHz has even not been given because the noise level of the measurement was too high beyond 10 kHz.

5. DESIGN OF THE SMART PANEL AND TEST RIG FOR THE ACTIVE CONTROL OF SOUND TRANSMISSION EXPERIMENT

The preliminary test activity on the single channel feedback control system has provided very promising results, which have encouraged a further development of the control system. Therefore, a new smart panel has been designed and built in order to implement the multi-channel control system discussed in section 2. The arrangement consists of a smart panel with an array of 16 decentralized sensor–controller–actuator systems. Each control unit is composed of a small square piezoelectric patch bonded on one side of the panel. An accelerometer is placed on the other side of the panel in such a way as it measures the panel transverse velocity in correspondence of the centre of the piezoelectric actuator. The actuator is driven by a single channel analogue feedback controller that provides a constant gain for the implementation of velocity feedback control. The panel with sixteen independent control units has been mounted on a Perspex box with inside a loudspeaker, which generates the primary disturbance.

In the next subsections the various components of the new smart panel and test rig facility are described in details. Also, the electronic design of the multi-channel control system is analysed and discussed.

5.1 Design of the smart panel

The testing smart panel built for this study consists of an aluminium panel of thickness $t = 1\,\text{mm}$, which has been clamped on a rigid frame so that the "vibrating area" is $l_x \times l_y = 414 \times 314\,\text{mm}$. The natural frequencies of the panel without taking into account the stiffening and mass effects of the control transducers are given in Table 5.1 below.

Table5.1: Natural frequencies of the clamped panel up to 1 kHz (the stiffening and mass effects of the control transducers are not taken into account).

m	n	Frequency (Hz)	m	n	Frequency (Hz)	m	n	Frequency (Hz)
1	1	69.7	5	1	441.3	2	5	776.2
2	1	118	1	4	495.6	7	1	795.8
1	2	163.4	5	2	522.4	6	3	814.7
3	1	197.3	4	3	522.9	5	4	837.7
2	2	208	2	4	538.8	3	5	846.1
3	2	283.0	6	1	604.8	7	2	875.1
4	1	305.3	3	4	609.3	4	5	944.3
1	3	305.7	5	3	654.3	6	4	995.7
2	3	349.1	6	2	684.8	7	3	1003.5
4	2	388.2	4	4	708.8	8	1	1014.0
3	3	421.1	1	5	732.9	1	6	1017.6

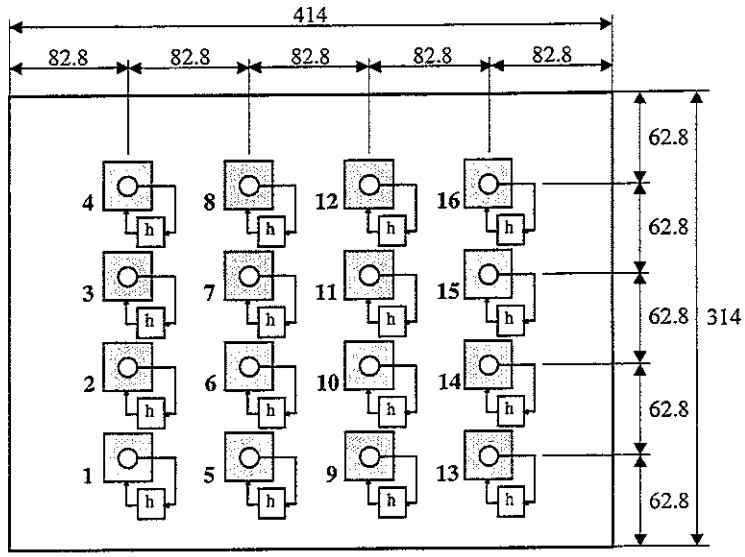

Figure5.1: *Arrangement of sixteen piezoelectric actuators, as shown by the squares, driven locally by the output of sixteen velocity sensors, as shown by the circles, via individual control loops with a gain of h (dimensions are in mm).*

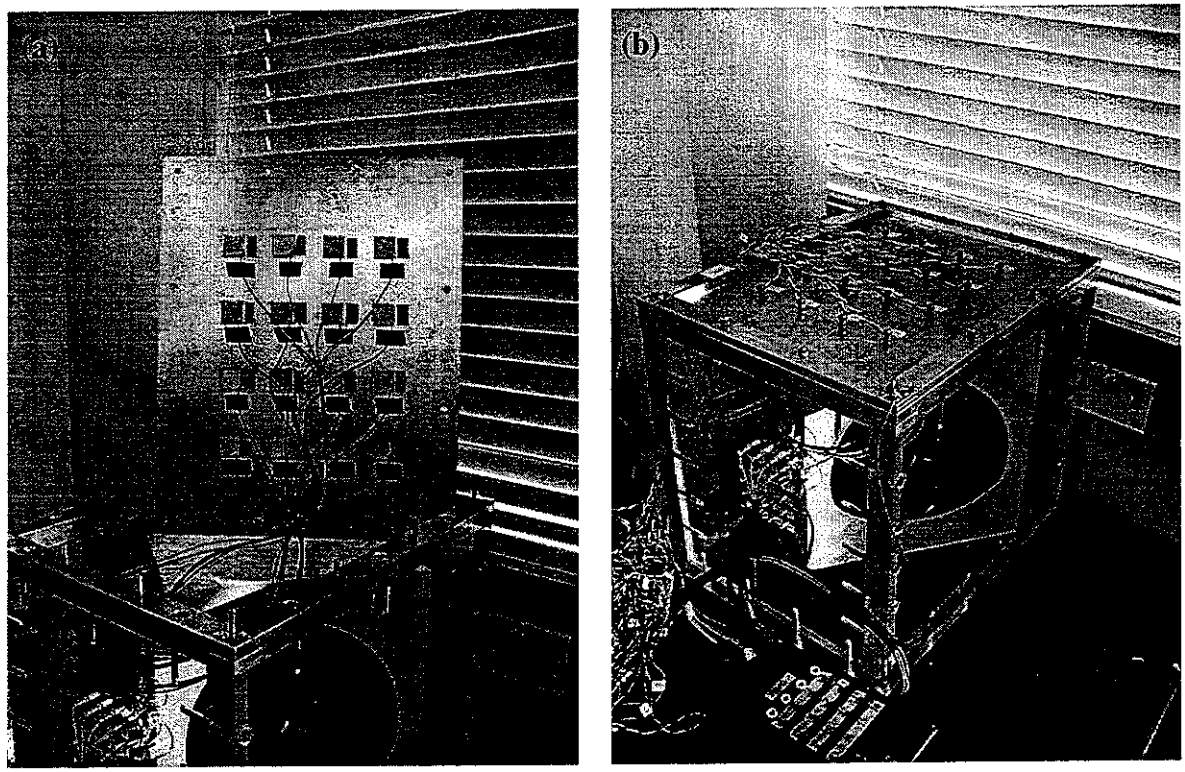

Figure5.2:*Panel with 16 piezoceramic actuators (a) and 16 collocated accelerometers. Each sensor actuator pair is driven by a decentralized analogue feedback controller. The panel is mounted on a Perspex box with inside a loudspeaker, which generates the primary disturbance (b)*

The panel is equipped with an array of 16 decentralized sensor–controller–actuator systems. As shown in Figures 5.1 and 5.2a, a 4×4 array of piezoceramic actuators, of dimensions $a \times b \times c = 25 \times 25 \times 1\,\text{mm}$, has been evenly bonded on one side of the panel so that the

distances between the centres of two adjacent patches or between the centre of a side patch and the edge of the panel is $d_x = 82.6$ mm and $d_y = 62.6$ mm. As can be seen in Figures 5.1 and 5.2b, on the other side of the panel a 4×4 array of high sensitivity ICP accelerometers (PCB Piezotronics, model 352C67) has been arranged in correspondence to the centres of the sixteen piezoceramic patches. Each sensor–actuator pair is connected via a single channel analogue feedback controller. The controller is set to feedback a control signal proportional to the transverse velocity at the centre position of the actuator detected by the accelerometer.

5.2 Design of the box facility

In order to assess the performance of the control system in terms of attenuation of the sound power radiation, the panel has been mounted on a Perspex box, which, has shown in Figure 5.2, has inside a loudspeaker that generates the primary disturbance. The internal dimensions of the Perspex box are: $p_x \times p_y \times p_z = 414 \times 314 \times 360$ mm and the natural frequencies of the acoustic modes up to 2.25 kHz are given in Table 5.2 below [25].

Table5.2: Natural frequencies of the acoustic cavity up to 1.56 kHz from ref. [25]

i	j	k	Frequency (Hz)	i	j	k	Frequency (Hz)	i	j	k	Frequency (Hz)
1	0	0	414.25	1	0	2	1038.9	3	1	0	1357.5
0	0	1	476.39	0	2	0	1092.4	2	2	0	1371
0	1	0	546.18	0	1	2	1098.2	2	1	2	1375.7
1	0	1	631.31	2	1	1	1100.8	0	0	3	1429.2
1	1	0	685.5	1	2	0	1168.3	3	1	1	1438.6
0	1	1	724.75	1	1	2	1173.8	0	2	2	1449.5
2	0	0	828.5	0	2	1	1191.7	2	2	1	1451.4
1	1	1	834.78	3	0	0	1242.8	1	0	3	1488
0	0	2	952.78	1	2	1	1261.7	1	2	2	1507.5
2	0	1	955.7	2	0	2	1262.6	0	1	3	1530
2	1	0	992.33	3	0	1	1330.9	3	0	2	1566

As shown in Figure 5.3, a pair of rigid aluminium frames has been used to clamp the smart panel on the open side of the box. Both frames have a width of *w=30* mm, but they have different thickness: 25 mm for the bottom frame and 10 mm for the top one. The dimensions of the plate used to build the smart panel have been chosen to match the width and length of the clamping frame so that $l_{px} \times l_{py} \times t = 444 \times 344 \times 1$ mm.

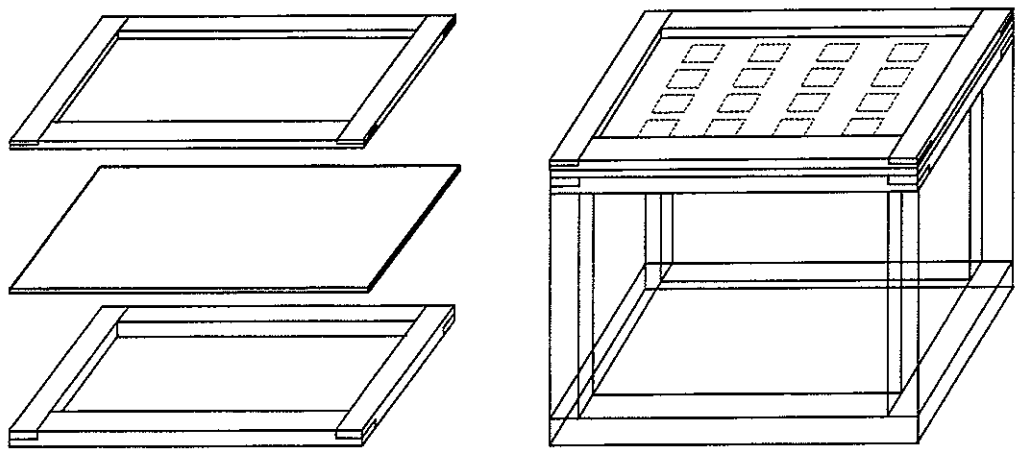

Figure 5.3:*Design of the rigid frames using for mounting the smart panel on the open side of the Perspex box.*

The box is made with relatively thick plates of Perspex so that the acoustic field generated by the loudspeaker inside it is essentially transmitted through the smart panel. The thickness of the Perspex plates have been chosen to be 30 mm so that, below 5 kHz the sound transmission through the smart panel is about 30 dB higher than the flanking component radiated by the Perspex walls. With this arrangement it is therefore possible to evaluate the reduction of sound transmission through the smart panel even when the control system is working and therefore attenuates the passive sound transmission by some 5 to 15 dB.

As can be noticed in Figure 5.2b, a set of electric plugs has been applied to one wall of the box to help the wiring between the sixteen pair of sensor/actuator and the electrical equipment (power amplifier, phase-lag compensator and integrator).

5.3 Design of the electric circuit

Taking advantage of the work carried out on the small panel to design a single channel velocity feedback control system sixteen independent single channel control units have been designed and built. Each unit consists of an integrator circuit to transform the output of the accelerometer sensor to velocity, a power amplifier and a phase lag compensator circuit as shown in Figure 4.4. The preliminary activity provided key information with regards to the electric characteristics of these three electric components, particularly for the design of the integrator and of the amplifier stages.

The analogue control systems built for each decentralized control unit are composed by a cascade of six electrical elements: an integrator, the phase–lag compensator previously described, a low–power pre–amplifier for the velocity test point, a low–power amplifier for adjusting the gain level, a switching circuit driven by a manual switch to select the output (inverted, non-inverted, no output) and a ILP HY2001 power amplifier to drive the piezoelectric actuator. Moreover the controller includes an operational amplifier driven by a manual switch to enable/disable all the control signals at the same time.

Such a controller provides a maximum voltage signal of 30 Volts peak to peak for an output power of 40 Watts RMS.

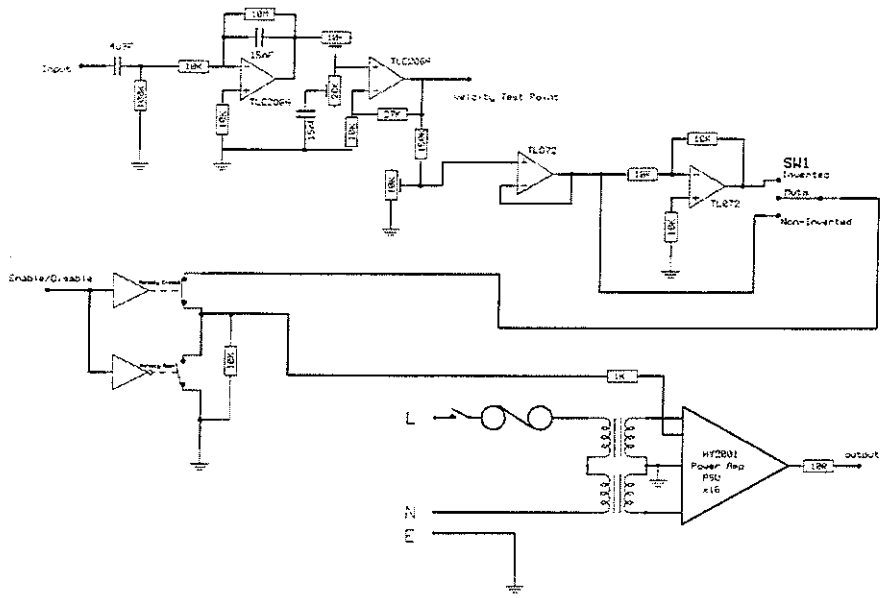

Figure 5.4: *Electric scheme of each of the 16 channels decentralised feedback control system*

Figure 5.4 shows the electric scheme used for each channel of the analogue control system. All the sixteen channels have been assembled in the single device shown in Figure 5.5 below. The complete testing system is shown in Figure 5.6 where on the centre it can be noticed the Perspex box with inside the loudspeaker primary source and on top the smart panel with the sixteen piezo actuators and accelerometer sensors. On the left side is visible the sixteen channel PCB signal conditioner while on the right hand side the analogue sixteen channels decentralised feedback control units system is shown.

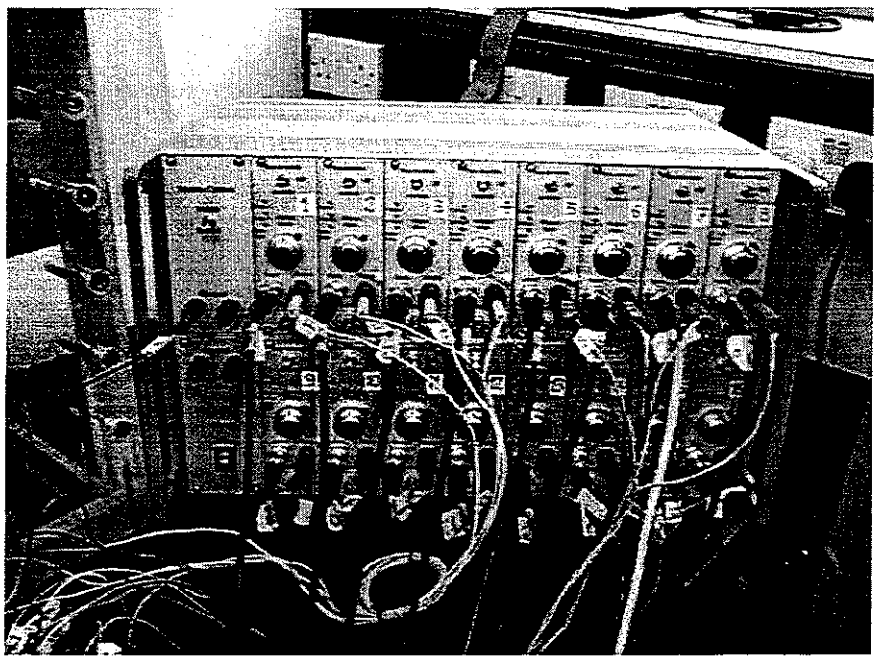

Figure5.5: *The sixteen channels decentralised feedback control system*

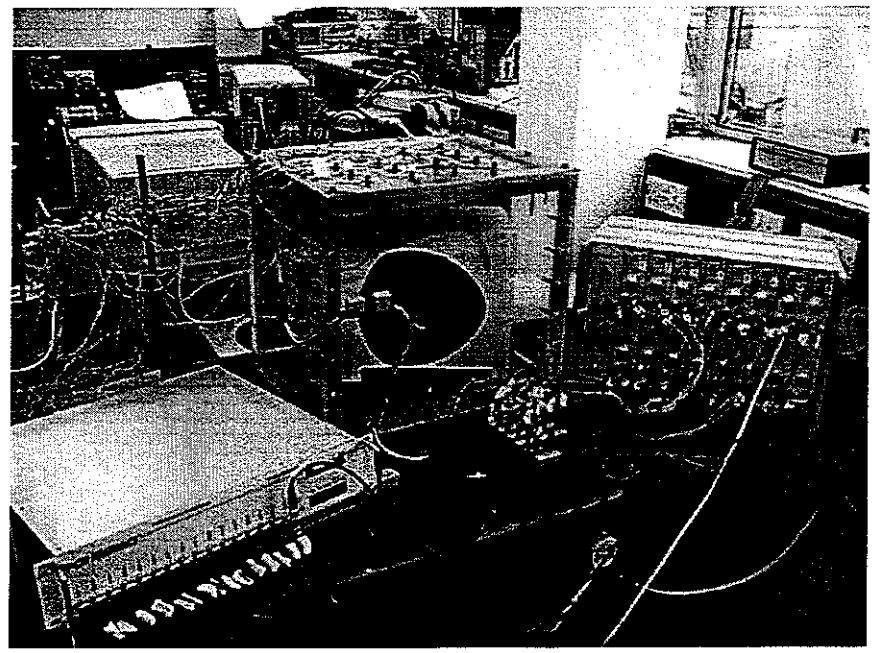

Figure 5.6: *The complete experimental setup with the Perspex box with on top the smart panel and the control equipment: signal conditioner (left), controller (right).*

6. IMPLEMENTATION OF THE DECENTRALIZED ACTIVE CONTROL SYSTEM

This section is focused on the implementation of the final version of the smart panel with 16 decentralised feedback control units studied in this project. The development of this system has required both experimental work and numerical simulations. The measurement work has been exclusively done on the testing system described in section 5. In order to understand, justify and learn how to optimise the system, some simulation tasks have been also been carried out using the mathematical model developed for the introductory theoretical study on the effectiveness of this smart panel as presented in section 2.

In the following subsection the open loop sensor–actuator measured frequency response functions of sensor–actuator pairs are first analysed and contrasted with those derived from the simulations, in a frequency range up to 50 kHz. The results refer to measurements taken on one of the four central control units, precisely the number 7, according to the numeration used in Figure 5.1. In the second subsection the stability and of the number 7 control unit is assessed. Since the system is not unconditionally stable, the study is oriented to identify the best compromise of the control gain such that there is good low frequency control and both enough gain margin and low spillover effects at higher frequencies. Finally the control performances of the smart panel excited by the acoustic field in the Perspex cavity are evaluated. Both the reduction of vibration at the error sensor of the control unit number seven and the reduction of sound transmission are given. These experiments have been conducted in the Control Laboratory so that the reduction of the panel vibration and sound transmission have been estimated using respectively the measured vibrations at the error sensors or the measured sound pressure with one microphone placed in correspondence to the centre of the panel at about 0.5 m.

Future work will involve the use of a laser vibrometer to measure the overall vibration of the smart panel when it is excited only by the acoustic field in the Perspex cavity and when the control system is turned on. This will give the possibility to estimate the kinetic energy of the panel before and after control. This gives a good estimate as well of the reduction of the near field sound radiation by the panel. Also, a more appropriate testing exercise will be carried out in an anechoic chamber in such a way that, using the appropriate arrangement of microphones, the total sound power radiate before and after control can be measured. Ideally, the best testing will be to measure the Transmission Loss of the panel by fixing the panel in the window connecting the reverberant (for the diffuse field primary excitation) and anechoic (for the radiation in free space measurement) rooms available at the ISVR.

6.1 Measured and simulated sensors/actuators frequency response function

In this subsection a comparison between the measured frequency response function of the plate and the simulated response provided by the numerical model is presented. A spectral analyser of Advantest Corporation, model R9211B/C, has been used to measure the frequency response functions of the sensor/actuator pair number 7, i.e. the relationship between the velocity signal of the sensor and the disturbance signal applied to the piezo actuator. The measured frequency response functions have been compared with simulated ones, which have been derived using the mathematical model presented in section 2.2. When the dynamic effects of the sixteen sensor–actuator systems are taken into account and no primary excitation is applied to the panel, i.e. $\mathbf{f}_p(\omega) \equiv 0$, then, according to the notation shown in

Figure 2.6 of section 2.2, the velocities of the panel at the centre of the sensor-actuator units is given by:

$$\mathbf{v}_c(\omega) = \mathbf{Y}_{cc}(\omega)\mathbf{f}_c(\omega) + \mathbf{Y}_{cs}(\omega)\mathbf{f}_s(\omega) \ , \tag{6.1}$$

Remembering that the force and velocity vectors at the centres of the control units $\mathbf{v}_a(\omega)$ and $\mathbf{f}_a(\omega)$, given in equations (6.2a,b), are linked by the impedance matrix $\mathbf{Z}_{aa}(\omega)$, given in equation (6.4), by equation (6.3)

$$\mathbf{f}_a(\omega) = \mathbf{Z}_{aa}(\omega)\mathbf{v}_a(\omega) \ , \tag{6.2}$$

so that, using (a) the dynamic equilibrium, $\mathbf{f}_c = -\mathbf{f}_a$, and (b) compatibility conditions, $\mathbf{v}_c = \mathbf{v}_a$, at the junctions between the control units and the plate the vector with the velocities of the panel at the centre of the sensor-actuator units is found in this case to be:

$$\mathbf{v}_c(\omega) = \left(\mathbf{I} + \mathbf{Y}_{cc}(\omega)\mathbf{Z}_{aa}(\omega)\right)^{-1}\mathbf{Y}_{cs}(\omega)\mathbf{f}_s(\omega) \ , \tag{6.3}$$

The vector with the measured velocities by the accelerometer sensors $\mathbf{v}_m(\omega)$ can be retrieved from equation (2.61) so that

$$\mathbf{v}_m(\omega) = \mathbf{A}(\omega)\left(\mathbf{I} + \mathbf{Y}_{cc}(\omega)\mathbf{Z}_{aa}(\omega)\right)^{-1}\mathbf{Y}_{cs}(\omega)\mathbf{f}_s(\omega) \ , \tag{6.4}$$

where the diagonal matrix $\mathbf{A}(\omega)$ contains the sensing functions of the sixteen accelerometer sensors. Equation (6.4) can also be written as

$$\mathbf{v}_m(\omega) = \mathbf{T}(\omega)\mathbf{f}_s(\omega) \ , \tag{6.5}$$

where

$$\mathbf{T}(\omega) = \mathbf{A}(\omega)\left(\mathbf{I} + \mathbf{Y}_{cc}(\omega)\mathbf{Z}_{aa}(\omega)\right)^{-1}\mathbf{Y}_{cs}(\omega) \ , \tag{6.6}$$

So, when the mass effects of the piezo and accelerometer transducers and the dynamic effects of the accelerometers are taken into account, then the sixteen sensor actuator frequency response functions can be extracted from equation (6.5) by taking the sixteen diagonal terms of the matrix $\mathbf{T}(\omega)$. For example the frequency response function giving the measured velocity at the accelerometer sensor number 7 due to the unit excitation of the collocated piezo actuator 7 is given by the frequency response function $T_{7,7}(\omega)$.

In practice the physical properties of the sixteen accelerometer sensors and piezo actuators differs from each other, in particular each accelerometer has a different resonance frequency which, for the sixteen transducers used in the smart panel, have been found to go from a minimum of 35 kHz to a maximum of about 42 kHz. This is variability of the resonance frequency is rather important and therefore the simulations shown below have been obtained by using the physical parameters summarised in Table 2.5 with the inertia masses of the sixteen accelerometers, m_a, spread in a range of values such that the natural frequencies of

the sixteen accelerometers are uniformly distributed between 35 kHz and 42 kHz. Also, in order to account for the inertia and stiffening effects of the piezo actuators the smeared density and Young's parameters given in Table 2.1 have been used in the simulations.

In the following three figures, 6.1 to 6.3, the measured sensor-actuator frequency response functions are contrasted with those obtained from the numerical model respectively for three frequency ranges of 0-1 kHz, 0-10 kHz and 0-50 kHz. In these plots, together with the measured frequency response function (faint line) two other curves are plotted: the first is the simulated sensor-actuator frequency response function when the sensor-actuator mass and dynamics effects are not accounted for (dashed line), and the second is the simulated sensor-actuator frequency response function when the sensor-actuator mass and dynamics effects are instead taken into account (solid line).

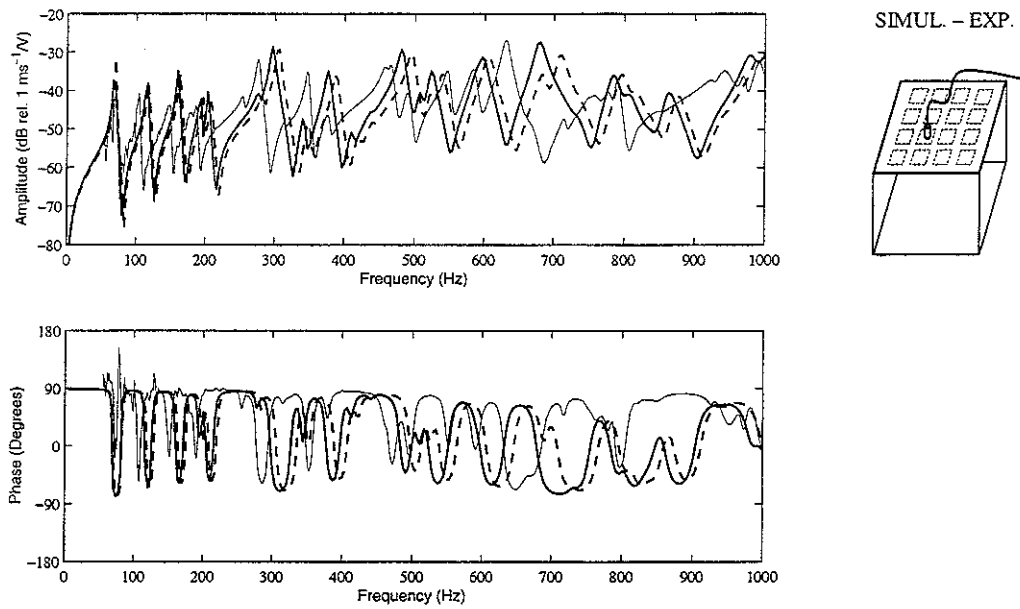

Figure 6.1: *Open Loop FRF (0-1 kHz) of the sensor/actuator pair n. 7: simulated FRF with no effects (dashed line), with sensor-actuator mass and dynamics effects (solid line), and measured FRF (faint line)*

Figure 6.1 shows that, for frequencies up to the fourth resonance frequency of the plate (283 Hz), the solid line, which represent the simulated frequency response function with the sensor-actuator dynamic effects, overlaps the dashed line, which represent the simulated frequency response function without effects. However, for frequencies above the fourth resonance, the sensor-actuator dynamic effect produces a small downward shifting of the resonance frequencies of the plate as one would expect as the result of adding mass to the system. Comparing the measured frequency response function with both the numerical simulations, it can be seen that the agreement between the experimental and numerical results is satisfactory, either in terms of amplitude or phase value of the frequency response function. Figures 6.2 shows the simulated frequency response functions compared with the measured frequency response function in a frequency range of 0-10 kHz. In this case, the amplitude of the simulated frequency response function with sensor-actuator dynamics effects (solid line)

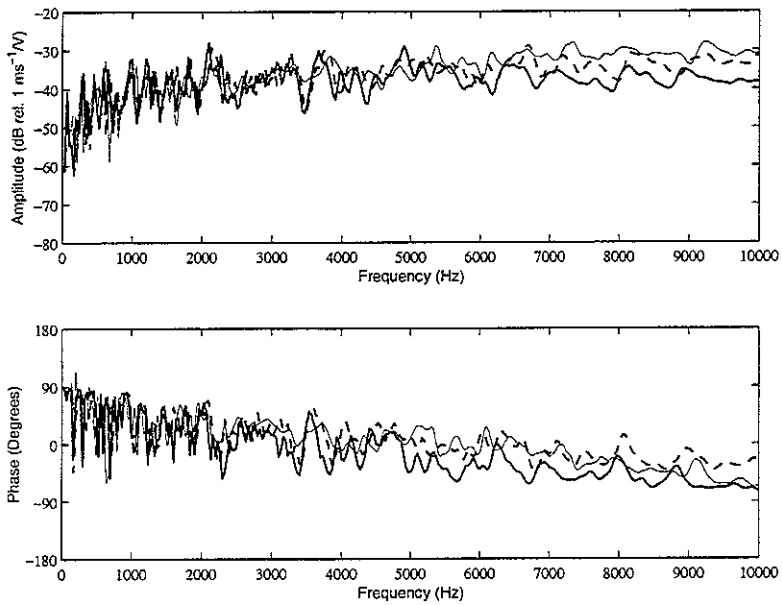

Figure 6.2: *Open Loop FRF (0-10 kHz) of the sensor/actuator pair n. 7: simulated FRF with no effects (dashed line), with sensor-actuator mass and dynamics effects (solid line), and measured FRF (faint line)*

presents a more flat trend of the module above 4 kHz with respect to the simulated frequency response function, which does not account for these effects (dashed line). In terms of amplitudes, both simulated curves present small differences respect to the measured one (faint line) and in terms of phase values a good agreement can be seen, particularly between the measured and simulated frequency response function which include the sensor-actuator effects.

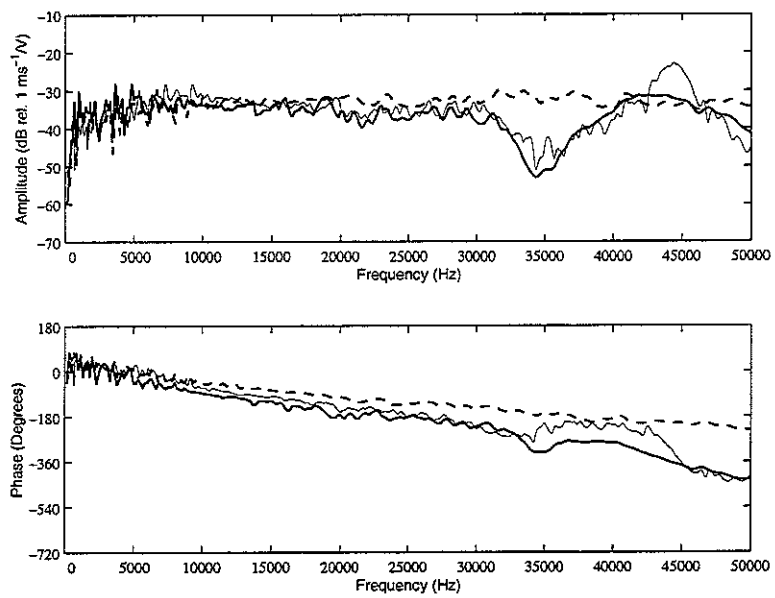

Figure 6.3: *Open Loop FRF (0-50 kHz) of the sensor/actuator pair n. 7: simulated FRF with no effects (dashed line), with sensor-actuator mass and dynamics effects (solid line), and measured FRF (faint line)*

Figure 6.3 shows, within a frequency range of 0-50 kHz, the two simulated frequency response functions (with and without sensor-actuator dynamic effects) contrasted with the measured frequency response function. The simulated frequency response function that does not account for sensor-actuator dynamics effects (dashed line) presents an almost flat amplitude trend in the whole frequency range. In contrast, the frequency response function which takes into account for both the accelerometer and piezo actuator mass effects and the accelerometer dynamics (solid line) has a more complex behaviour which is characterised by a relatively wide frequency band trough between 30 kHz and 40 kHz and a crest between 43 kHz and 46 kHz which better agrees with the measured response.

Indeed, as shown in Figure 2.5, the accelerometer is a sort of a single degree of freedom neutralizer that reduces the vibration level at the measurement point in correspondence to its natural frequency. In fact each input impedance frequency function of the accelerometers have a peak in correspondence to the resonance frequency of the accelerometers and then a trough at higher frequencies. Figure 6.4 shows the input impedances of the sixteen accelerometers assuming their resonance frequencies are uniformly spread between 35 kHz and 42 kHz. From this plot it is fairly clear that there is a relatively high impedance effect in such a frequency band that therefore tends to reduce the vibration of the panel as found in Figure 6.3.

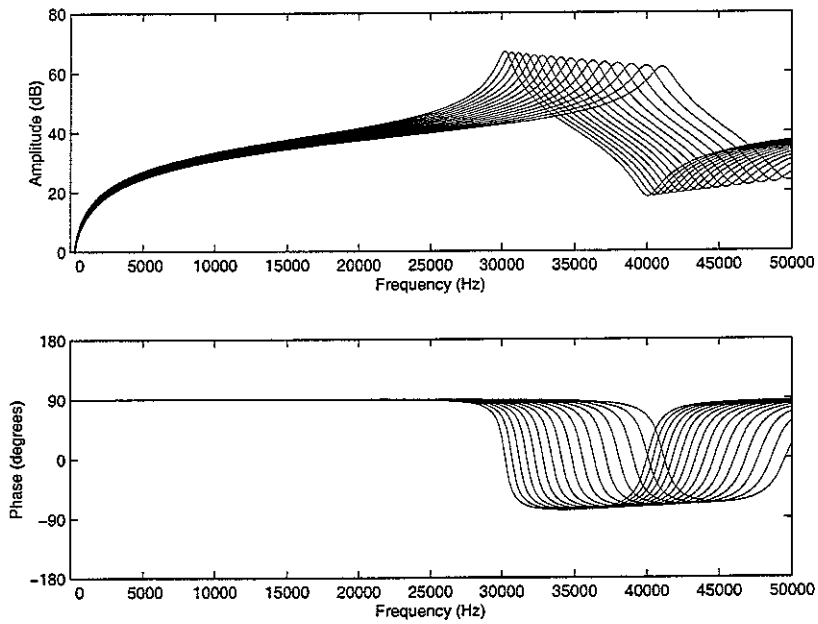

Figure 6.4: *Input impedance frequency functions of the sixteen accelerometer sensors used in the panel.*

The sensitivity functions that give the ratio between the measured velocity signals by the accelerometers and the true velocities underneath the accelerometers are characterised by a peak in correspondence to the resonance frequencies of the accelerometers. However this effect is limited to a relatively narrow frequency band as shown in Figure 6.5 below. Therefore, the measured sensor–actuator frequency response function remains characterized by the trough at 30 kHz to 40 kHz and the crest between 43 kHz and 46 kHz generated by the sixteen accelerometers that works as neutralizers.

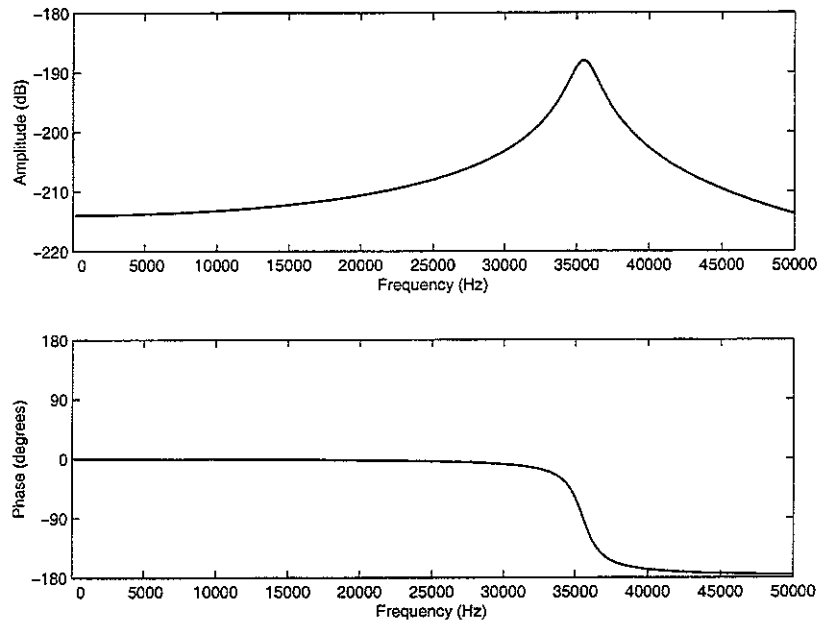

Figure 6.5: *Sensitivity function of one accelerometer used in the smart panel.*

The analysis of the measured and simulated sensor-actuator frequency response functions shows that the frequency responses are affected by an evident phase shift above 10 kHz as shown for example in Figures 6.3. This phase lag is due to the fact that the accelerometer and the piezoelectric patch are not a truly collocated and dual sensor–actuator pair. The actuation mechanism of the piezoceramic actuator can be modelled as four lines of moments acting along the edges of the piezoelectric patch, with transverse point forces at the four corners [24]. The sensor is instead measuring the transverse velocity at the centre position of the actuator patch. There are thus two types of problems: the actuation and sensing are not collocated and also the moment actuation is not compatible to the linear transverse velocity sensing. Both effects contribute to determine a non–positive definite frequency response function at higher frequencies.

Intuitively, the non–collocated positioning effect found above 10 kHz for the accelerometer sensor piezo actuator frequency response function depends on the size of the actuator patch with reference to the bending wavelength vibration of the plate. The collocated positioning effect can therefore be extended to a wider frequency range by using a smaller piezoelectric patch actuator. Figure 6.4 shows the predicted sensor–actuator frequency response functions with two different piezoelectric patch actuators, of dimensions 25×25 mm (solid line) and 12×12 mm (faint line). The bottom plot confirms that with a smaller patch the phase roll off is much lower than with the larger patch. Indeed by halving the size of the actuator the frequency response function is then found to be positive definite up to about 35 kHz. The draw back is that by reducing the size of the piezoelectric patch the control authority is also decreased. Therefore a compromise has to be found between the possibility of extending the minimum phase property of the sensor actuator frequency response function to higher frequencies and the required control authority to produce the desired control effect.

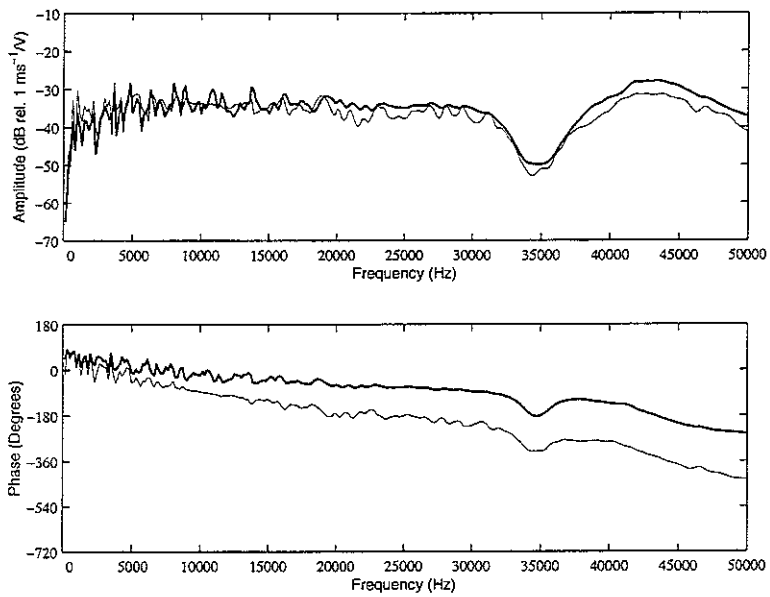

Figure 6.6:*Open Loop FRF (0-50 kHz) of the sensor/actuator pair n. 7: simulated FRF with standard size piezoelectric patch (solid line) and with smaller size patch (faint line)*

6.2 Nyquist plot of the measured sensor-actuator frequency response function

The sixteen velocity feedback control systems implemented for the new smart panel have the same structure than that of the one developed for the small panel with five piezo actuators studied in Section 4. Thus they can be studied with reference to the block diagram shown in Figure 4.5 with the compensator given in Figure 4.4. As discussed in Section 4.1, there are two important features to be taken into account for the design of this control system: first the stability and second the control effectiveness and control spillover phenomena. In order to have an unconditionally stable control system that gives some control performance at all frequencies the Nyquist plot of the sensor–actuator open loop frequency response function should stay in the right hand side of the plot, in other words the frequency response function must be positive definite. If this is not the case, then two problems can arise: first, if the sensor–actuator frequency response function encircles the Nyquist point $(0,-1)$ so that the feedback controller is unstable; second, at those frequencies where the sensor–actuator frequency response function enters the circle of radius 1 and centre $(0,-1)$ the vibration at the error sensor rises rather than falling down because of control spillover. The analysis of the sensor–actuator frequency response function in the previous section has shown that the frequency response function is not minimum phase. Indeed above about 10 kHz the phase exceed -90° and constantly rises up to -360° in correspondence to 50 Hz. Also, the amplitude gradually rises up to 2 kHz and then remains constant around the maximum amplitude values at higher frequencies. There is just a trough between 30 kHz and 40 kHz, which is however followed by a crest with relatively high amplitudes between 43 kHz and 46 kHz. Therefore it is likely that at higher frequencies the sensor–actuator frequency response function enters the left hand side of the Nyquist plot and for relatively low values of gains enters the circle of radius 1 and centre $(0,-1)$ or even encircles the Nyquist point $(0,-1)$ since the amplitude of the sensor–actuator response was found to be relatively large even at high frequencies. Thus, it is possible that even for small values of gain the control system is affected by control spillover at the higher frequencies or even goes unstable.

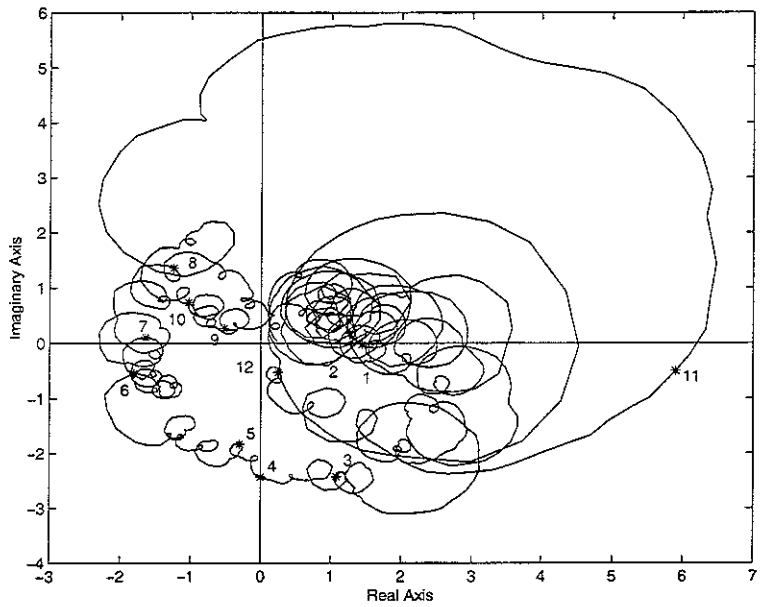

Figure 6.7: *Nyquist plot (0-50 kHz) at the sensor number 7, exciting with the collocated piezoelectric actuator: 1=1 kHz, 2=5 kHz, 3=10 kHz, 4=12.5 kHz, 5=15 kHz, 6=20 kHz, 7=25 kHz, 8=30 kHz, 9=35 kHz, 10=40 kHz, 11=45 kHz, 12=50 kHz*

Considering in details the Nyquist plot of the sensor–actuator frequency response function, it can be noticed that the trough of the amplitude of the sensor–actuator frequency response function between 30 kHz and 40 kHz, which is due the neutralizing effects of the sixteen accelerometers, occupies exactly the negative, left hand side, of the Nyquist plot. Therefore, as expected the Nyquist plot is characterised by a left hand side part which however is quite squeezed towards the imaginary axis. This is a very important result, since, even if the sensor – actuator frequency response function is not minimum phase, still relatively large control gains can be used without entering in instability and without having too large control spillover phenomena. Also, the resonance effect due to the accelerometer sensor at around 44 kHz is, in this case, not compromising the stability of the control system since the sensor–actuator frequency response function between 40 kHz and about 50 kHz is positive definite.

However it must be said that this was not designed in advance and has come out from a fortunate choice of the mass of the piezoelectric patch and accelerometer. The design of the sensor – actuator transducer is therefore very important and besides actuation effectiveness, it is a requirement to have a couple of transducers which could be minimum phase but with very small amplitudes in correspondence of frequency bands in which the sensor – actuator frequency response function is negative definite.

6.3 Implementation of the velocity feedback control system

This section is concerned with the experimental implementation of the decentralised control system mounted on the test rig facility described in section 5.2. As previously described, the arrangement that has been used consists of a smart panel with sixteen piezoelectric actuators driven locally by the output of sixteen velocity sensors (see Figure 5.2). The controller that has been used for the on line implementation is described in section 5.3 and it provides

sixteen individual control loops with adjustable gains with a maximum output power of 40 Watts for each channel (see Figure 5.5).

In these experimental tests, the panel has been excited by a white noise acoustic disturbance provided by the loudspeaker positioned inside the Perspex box. In order to assess the performance of the decentralised control system, the frequency response functions of the error sensors number 7 and 13 shown in Figure 5.1 per unit excitation of the loudspeaker have been measured with and without the sixteen local feedback loops implemented. The performance of the control system has been investigated in two frequency ranges: 0 to 1 kHz and 0 to 5 kHz.

An initial indication of the noise reduction effectiveness of the smart panel has also been derived by measuring the acoustic sound pressure at about 0.5 m above the panel in correspondence to the centre of the panel itself for three frequency ranges of the disturbance: 0 to 1 kHz, 0 to 2 kHz and 0 to 5 kHz. The measurements have been carried out in a laboratory room with some acoustic treatments on the sidewalls.

The results presented in this section should thus be considered as a first indication of the true control effectiveness since both the vibratory level and sound radiation of the panel are not evaluated in an appropriate way.

The vibration of the panel in correspondence to the error sensor n. 7 is shown in Figures 6.8 and 6.9 with reference to a frequency band 0 to 1 kHz. The solid line represents the measured response of the plate without control while the faint line represents the same parameter when either only the control unit n. 7 (Figure 6.8) or all sixteen control units (Figure 6.9) are working with a fixed feedback control gain chosen to guarantee stability and low spillover effects at higher frequencies. From these two plots, it can be noticed that the single control loop provides attenuation factors of about 5 dB on the two dominant resonance frequencies measured by the sensor, while the sixteen decentralised channels feedback control system produces attenuation factors of 15 to 20 dB.

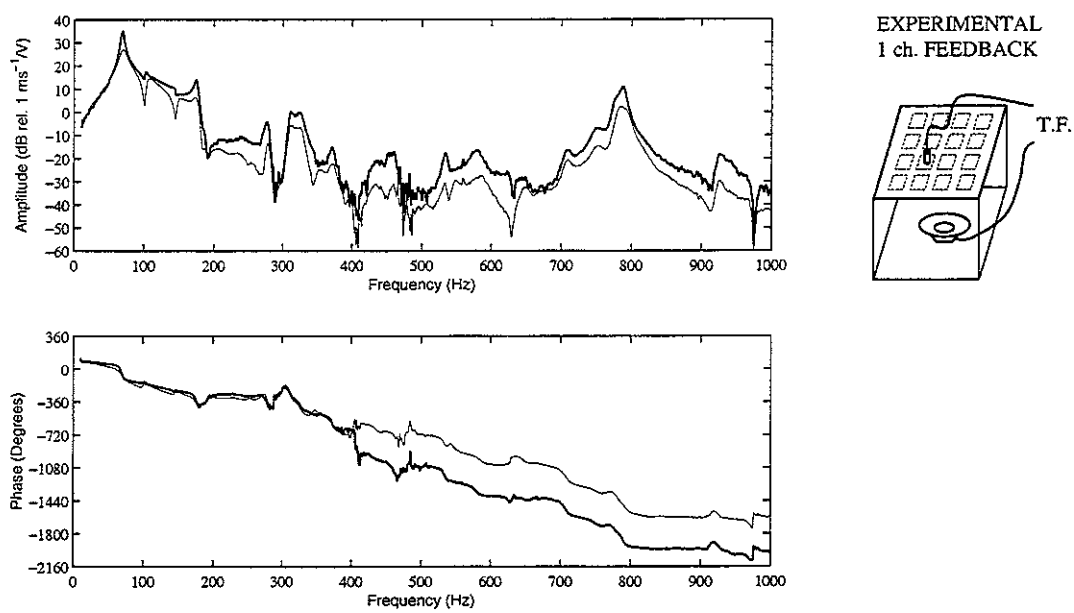

Figure6.8: *Experimental feedback control effectiveness (0-1 kHz) with a single loop on the sensor/actuator pair n. 7, considering the transfer function of the velocity at the error sensor n. 7 per unit excitation of the loudspeaker: no control system (solid line) and feedback control loop (faint line) using the compensator*

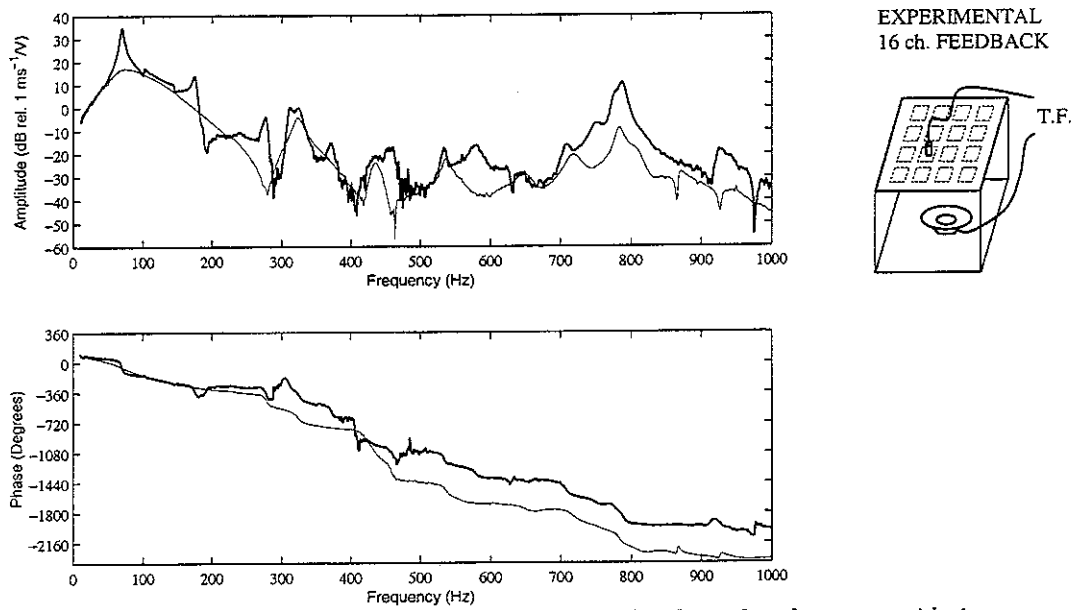

Figure 6.9: *Experimental feedback control effectiveness (0-1 kHz) with 16 independent loops, considering the transfer function of the velocity at the error sensor n. 7 per unit excitation of the loudspeaker: no control system (solid line) and feedback control loop (faint line) using the compensator*

Figures 6.10 and 6.11 gives the same two plots shown above in the frequency range 0 to 5 kHz. Considering these two plots, it can be seen that the single control unit provides attenuation factors of about 5 dB up to 5 kHz, while the sixteen channels decentralised feedback control system can give attenuation factors up to 10–15 dB in the same frequency range. Also in both cases, i.e. single and sixteen feedback control units, the closed loop response is not affected by any instability at the higher frequency.

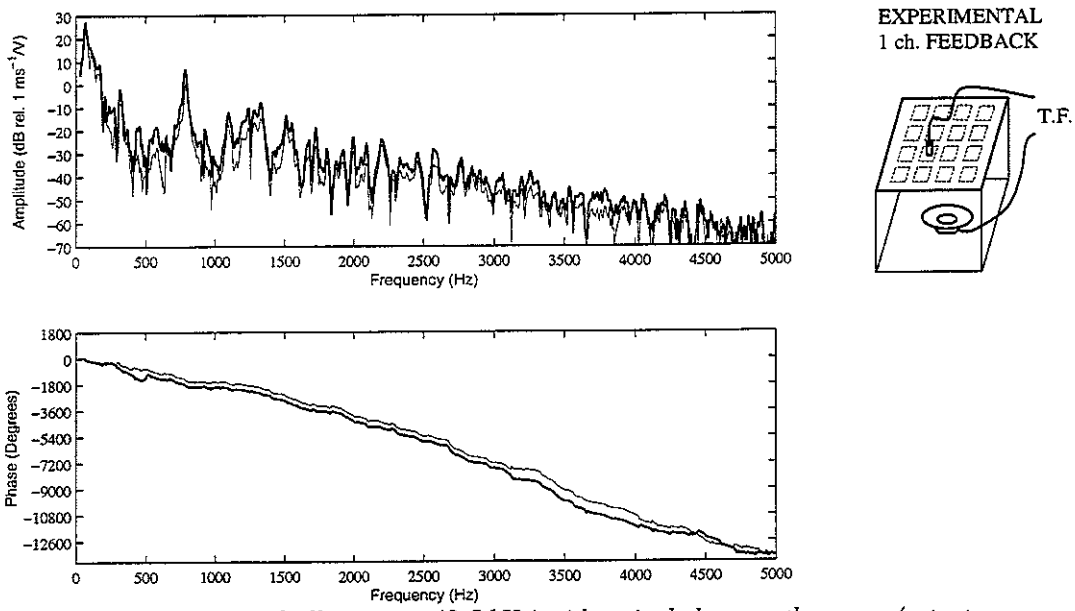

Figure 6.10: *Experimental feedback control effectiveness (0-5 kHz) with a single loop on the sensor/actuator pair n. 7, considering the transfer function of the velocity at the error sensor n. 7 per unit excitation of the loudspeaker: no control system (solid line) and feedback control loop (faint line) using the compensator*

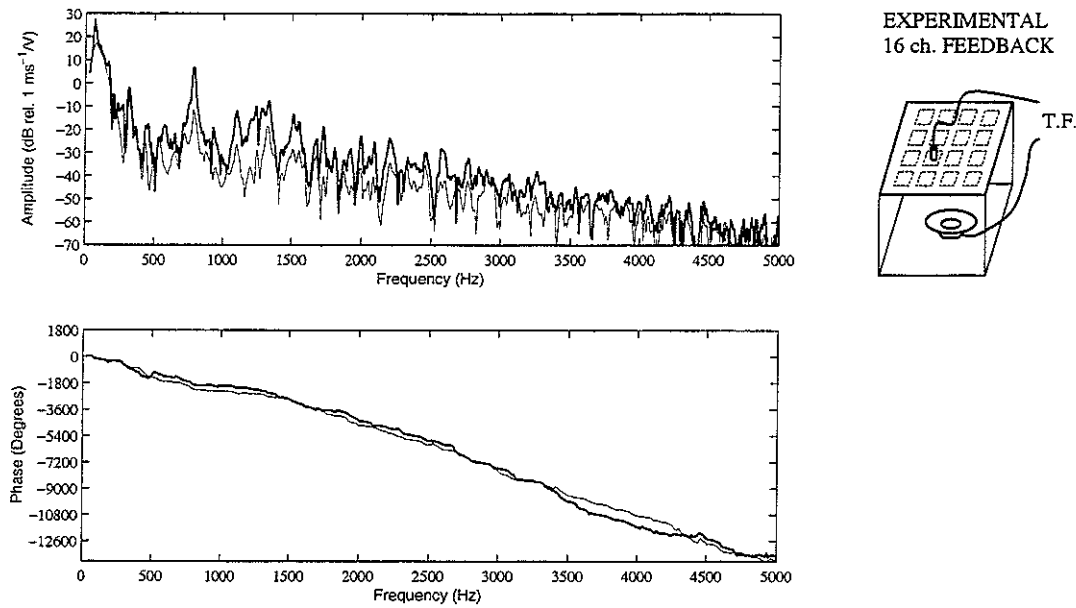

Figure 6.11: *Experimental feedback control effectiveness (0-5 kHz) with 16 independent loops, considering the transfer function of the velocity at the error sensor n. 7 per unit excitation of the loudspeaker: no control system (solid line) and feedback control loop (faint line) using the compensator*

The vibration level at the error sensors n. 13 per unit excitation of the loudspeaker are reported in the Figures 6.12 and 6.13 for the frequency range of 0 to 1 kHz and 0 to 5 kHz respectively. The attenuation factors obtained with this error sensor are similar to those previously reported, and, also in this case, the closed loop response is not affected by any instability at the higher frequency.

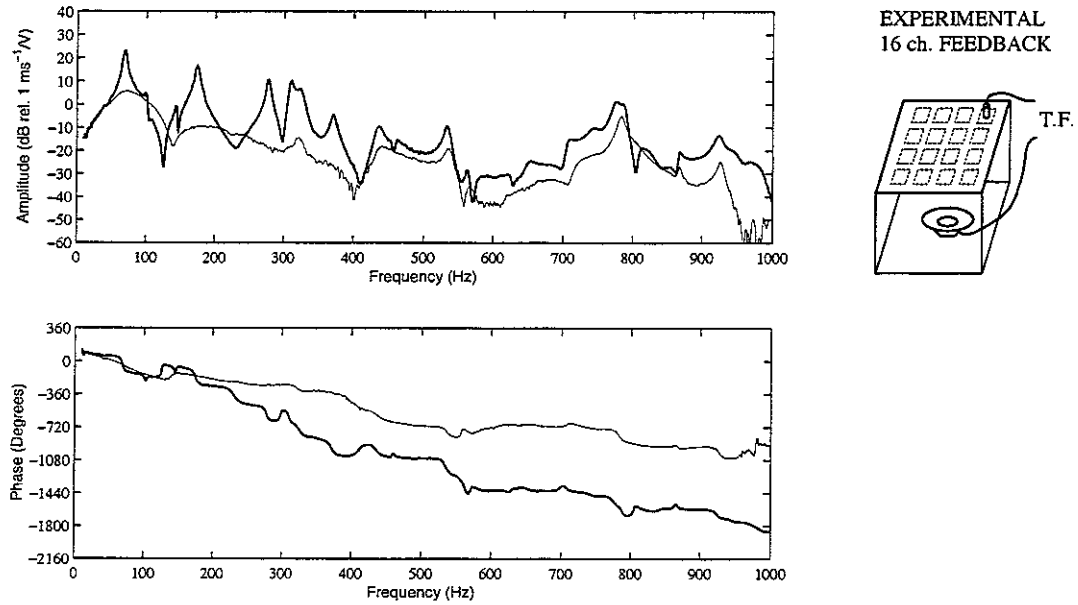

Figure 6.12: *Experimental feedback control effectiveness (0-1 kHz) with 16 independent loops, considering the transfer function of the velocity at the error sensor n. 13 per unit excitation of the loudspeaker: no control system (solid line) and feedback control loop (faint line) using the compensator*

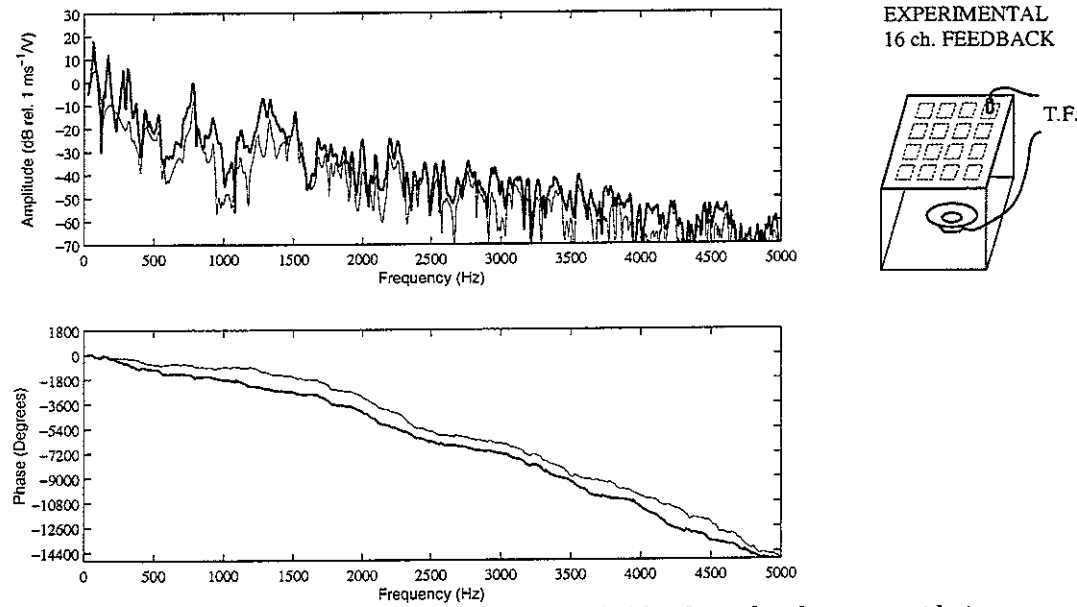

Figure 6.13: *Experimental feedback control effectiveness (0-5 kHz) with 16 independent loops, considering the transfer function of the velocity at the error sensor n. 13 per unit excitation of the loudspeaker: no control system (solid line) and feedback control loop (faint line) using the compensator*

The final part of this section is concerned with the noise reduction effectiveness of the smart panel, which has been estimated by measuring the acoustic sound pressure at about 0.5 m above the panel in correspondence to the centre of the panel itself. As previously explained, this results should be considered as a first indication of the true control effectiveness that need to be investigated more in detail by means of standard procedure of measurement of the sound pressure level around the plate in a anechoic chamber. The results obtained with this initial set of measurements are reported in Figures 6.14 to 6.16 for three different frequency ranges: 0 to 1 kHz, 0 to 2 kHz and 0 to 5 kHz. The solid line in Figure 6.14 shows the measured sound pressure per unit primary excitation to the primary loudspeaker without the control system on. The faint line gives the sound pressure when the sixteen control units are operating with a fixed gain that guarantees a stable feedback control. This plot indicates good reductions of about 7 dB and 12 dB in small frequency bands at about 100 Hz and 270 Hz. In Figure 6.15 the same kind of plot is shown for a frequency range 0 to 2 kHz, and it shows further reductions of about 20 dB and 10 dB in small frequency bands around 1300 Hz and 1750 Hz. Finally, Figure 6.16 shows the overall performances of the decentralised control system in the frequency range of 0 to 5 kHz. This plot shows no further control effects above 2 kHz, however it is found that the feedback controller guarantees a stable control effect with no spillover up to 5 kHz.

This preliminary result is quite encouraging since it could well be that an appropriate measurement of the total sound power radiation with a set of microphones arranged on a hemisphere over the panel and carried out in an anechoic room will unravel a better picture. Also, in this experiment, the control gains have been set without investigating whether they really coincided with the optimal gain as indicated in the theoretical work presented by Elliott et al. [15].

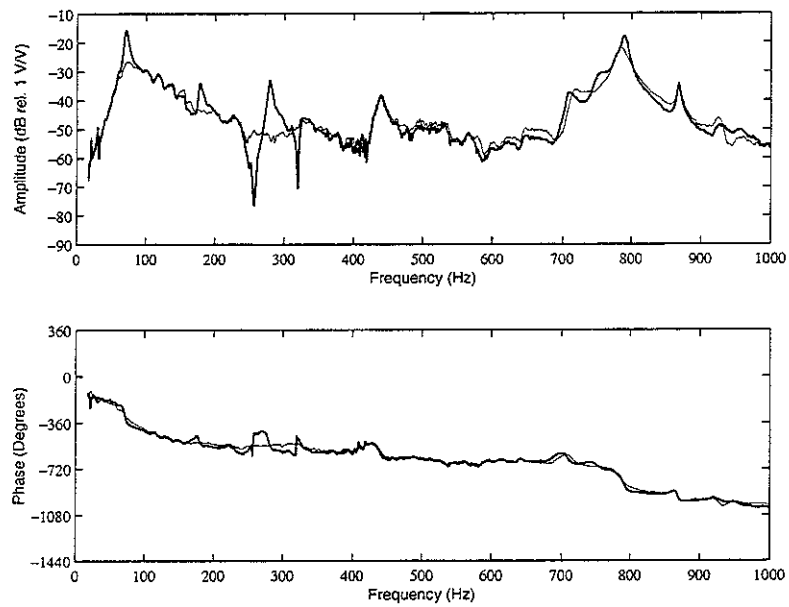

Figure 6.14: *Experimental feedback control effectiveness (0-1 kHz) with 16 independent loops, considering the transfer function of the microphone signal per unit excitation of the loudspeaker: no control system (solid line) and feedback control loop (faint line) using the compensator*

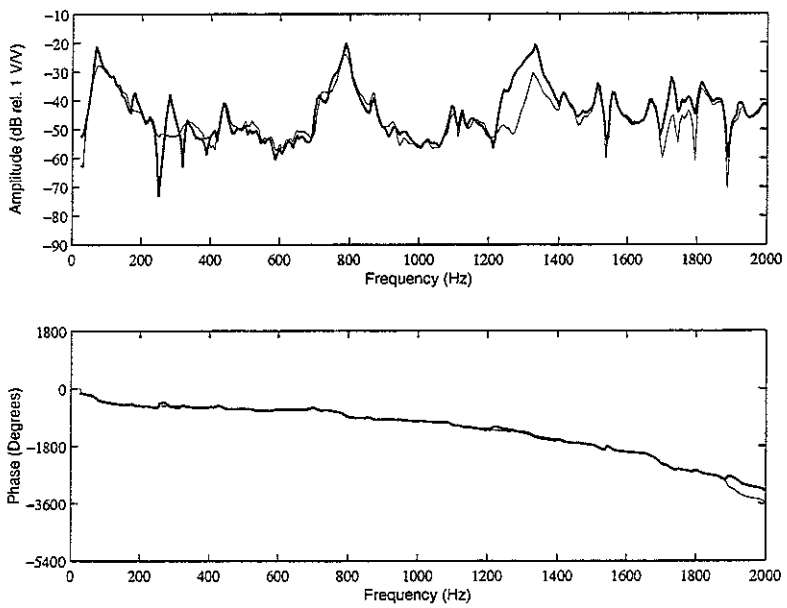

Figure 6.15: *Experimental feedback control effectiveness (0-2 kHz) with 16 independent loops, considering the transfer function of the microphone signal per unit excitation of the loudspeaker: no control system (solid line) and feedback control loop (faint line) using the compensator*

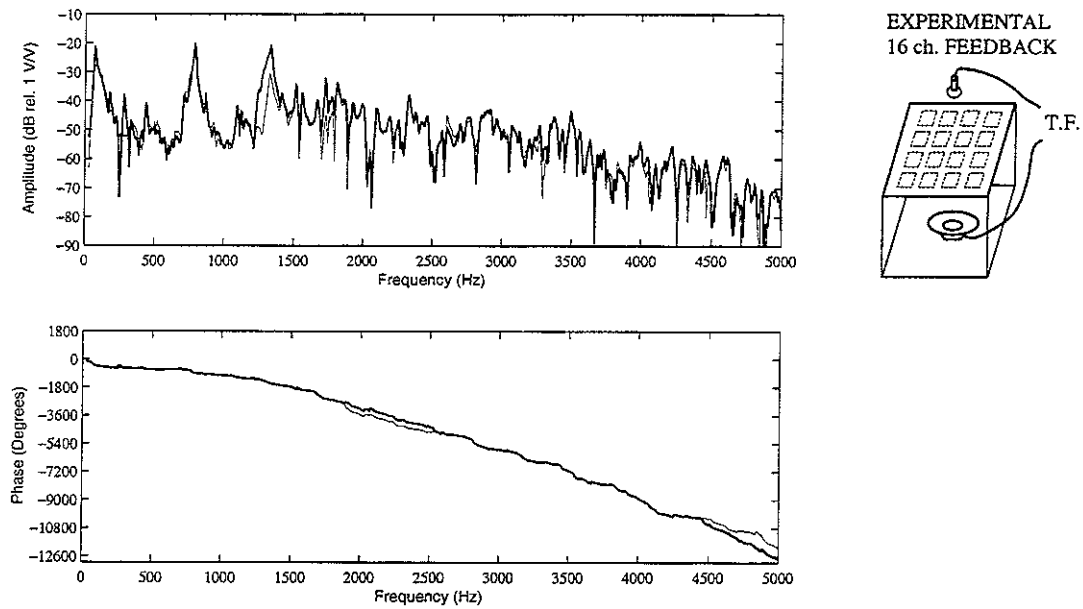

Figure 6.16: *Experimental feedback control effectiveness (0-5 kHz) with 16 independent loops, considering the transfer function of the microphone signal per unit excitation of the loudspeaker: no control system (solid line) and feedback control loop (faint line) using the compensator*

7. CONCLUDING REMARKS

The study presented in this report is concerned with the design of a smart panel with an array of 16 decentralized sensor–controller–actuator systems. Each control unit is composed of a small square piezoelectric plate bonded on one side of the panel. An accelerometer is placed on the other side of the panel in such a way as it measures the panel transverse velocity in correspondence of the centre of the small piezoelectric actuator. The actuator is driven by a simple analogue feedback controller, which provides a constant gain for the implementation of velocity feedback control.

A theoretical model is formulated with which the total kinetic energy and sound radiation ratio can be derived as a function of the incident acoustic field and as a function of the feedback gain implemented in the sixteen decentralised control units. Simulations results have been produced with reference to a range of feedback control gains and the results of two cases have been considered. In case one the sensor–actuator transducers have been idealised as sensors devices that precisely detect the point velocity at the centre of the control unit and actuator devices that generates four line of moments along the perimeter of each actuator patch. In case two, the stiffness and mass effects of the piezoelectric actuators and the mass effects together with the local dynamics of the accelerometers sensors have been taken into account. The numerical simulations have highlighted the following points.

1) The response of the panel and its sound radiation have been discussed with reference to a range of feedback gains in the decentralised control loops without considering the stiffness and mass effects of the piezoceramic actuator patches and the dynamic and mass effects of the velocity transducers. As the gains of the feedback loops are increased, the resonances in the response become more heavily damped, as one would expect with velocity feedback control. If the gains of the feedback loops are increased beyond a certain value, however, the closed loop response displays new peaks, such as that at about 140 Hz for example, which become more pronounced as the feedback gain is increased.
2) The same analysis has been carried out considering the sensor-actuator dynamic effects. The modal response of the panel is slightly different to that found for the previous case. This is due to the added masses of the sensors and actuators transducers. As one would expect, also in this case, as the gains of the feedback loops are increased, the resonances in the response become more heavily damped and when the gains of the feedback loops are increased beyond a certain value, the closed loop response displays new peaks due to the additional constraints at the sensors positions.

The second part of the study has been focused on a pre-existing aluminium panel of dimensions $l_x \times l_y \times s = 278 \times 247 \times 1$ mm which is glued on a rigid Perspex frame and it is equipped with five piezoelectric strain actuators patches bonded on the bottom side of the panel. A set of accelerometer has been placed in correspondence of the centre of each actuator, in such a way as to have five co-locate sensor-actuator pairs. The measured sensors/actuators frequency response functions of two control units (the central and top right pairs) have been analysed and contrasted with those derived analytically using the Euler–Bernoulli plate theory for bending vibration. In order to consider the mass effect due to the presence of the piezo actuator and accelerometer sensor on the panel, the impedance of a point mass placed in the centre of the plate has been included in the numerical model. Also, the sensing response effects have been considered including in the model formulation the accelerometer sensing frequency response function. Finally, a single channel stable feedback

analogue controller has been designed and implemented. This activity has highlighted the following points.

1) The frequency response function of the sensor–actuator pair used in the smart panel (Figure 4.3) is positive real (i.e. its phase is confined between $\pm 90^{\circ}$) up to about 7.5 kHz. At higher frequencies there is a constant phase roll off that builds up with frequency to -270° up to about 35 kHz. Above 35 kHz the frequency response function is again positive real.
2) The modulus of the sensor–actuator frequency response function is on average constant up to 7 kHz, above this frequency there is a constant roll–off that brings down the amplitude by about 20 dB at 35 kHz; however, around 44 kHz there is a clear resonance peak that brings back the amplitude to about the same level as that at low frequencies.
3) The constant roll–off has been found to be due to the local mass effect of the piezoelectric patch actuator and accelerometer sensor; the higher frequency resonance is instead due to the local dynamics of the accelerometer.
4) The positive real property of sensor–actuator response can be extended to higher frequencies by reducing the size of the piezoelectric patch actuator.
5) Because the sensor–actuator open loop frequency response function is not strictly positive real, the feedback control system is stable for a limited set of control gains.
6) Higher control gains can be implemented when a phase lag compensator is implemented in the controller. Also the control effectiveness can be improved by designing a sensor–actuator unit with a high–frequency and highly–damped velocity sensor resonance frequency.
7) The velocity measured by one of the control sensor was reduced between 5 dB and 20 dB up to about 5 kHz when only that control unit is operating

The final part of this study is concerned with the design and on-line implementation of the smart panel with sixteen decentralised feedback control systems. The testing smart panel built for this study consists a thin aluminium panel of dimensions $414 \times 314 \times 1$ mm with an embedded array of 4×4 square piezoceramic actuators. The sensing system consists of an array of 4×4 accelerometers that are positioned on the panel above the centres of the sixteen piezoceramic patches. Each of the sixteen sensor–actuator pairs is arranged to implement local (decentralised) velocity feedback control. In order to assess the performance of the control system in terms of attenuation of the sound power radiation, the panel has been mounted on a Perspex box, which has inside a loudspeaker that generates the primary disturbance. Sixteen independent single channel control units have been designed and built. Each unit consist of an integrator circuit to transform the output of the accelerometer sensor to velocity, a power amplifier and a phase lag compensator circuit. The on-line implementation has highlighted the following points.

1) The velocity measured by one of the control sensor was reduced between 5 dB and 10 dB up to about 5 kHz when only that control unit is operating.
2) When all control units are operating, the velocity measured by the same control sensor is then reduced between 5 dB and 20 dB up to about 5 kHz.
3) When all control units are operating, the measured sound pressure at about 0.5 m from the panel in correspondence to its centre has been found to be decreased by about 7 dB, 12 dB, 20 dB and 10 dB in small frequency bands at about 100 Hz, 270 Hz, 1300 Hz and 1750 Hz respectively.

8. REFERENCES

[1] J. S. Mixson and J. F. Wilby, "Interior noise", *Aeroacoustics of Flight Vehicles, Theory and Practice*, edited by H.H. Hubbard, NASA Langley Research Center, Hampton, VA, (1995), Chap. 16

[2] P. Nelson, *Transportation Noise Reference Book* (Butterworths, London, 1987)

[3] P. A. Nelson and S. J. Elliott, "Global Control of Enclosed Sound Fields", *Active Control of Sound* (Academic, London, 1999), Chap. 10

[4] U. Emborg, S. Leth, F. Samuelson and J. Holmgren, "Active and passive noise control in practice on the SAAB 2000 high speed turboprop", AIAA/Confederation of European Aerospace Societies Paper 98-2231, (1998)

[5] C. R. Fuller, R. J. Silcox, "Active structural acoustic control", J. Acoust. Soc. Am. **91**(1), 519 (1992)

[6] C. R. Fuller, S. J. Elliott and P. A. Nelson, "Active Structural Acoustic Control. I Plate System", *Active Control of Vibration* (Academic, London, 1997), Chap. 8

[7] C. F. Ross and M. R. Purver, "Active cabin noise control," Proceedings of ACTIVE 97, Budapest, HU, XXXIX-XLVI (1997)

[8] M. E. Johnson and S. J. Elliott, "Active control of sound and vibration using volume velocity cancellation," J. Acoust. Soc. Am. **98**(4), 2174-2186 (1995)

[9] S. J. Elliott, "Design and Performance of Feedback Controllers", *Signal Processing for Active Control*, (Academic, London, 2000), Chap. 6

[10] R. L. Clark, W. R. Saunders and G. P. Gibbs, *Adaptive Structures, Dynamics & Control"*, (Wiley, New York, 1998)

[11] P. Gardonio, Y. S. Lee, S. J. Elliott and S. Debost, "Active control of sound and vibration using volume velocity cancellation," J. Acoust. Soc. Am. **110**(6), 3025-3031 (2001)

[12] G. P. Gibbs, R. L. Clark, D. E. Cox and J. S. Vipperman, "Radiation modal expansion: Application to active structural acoustic control", J. Acoust. Soc. Am. **107**(1), 332-339 (2000)

[13] A. Francois, P. De Man and A. Preumont, "Piezoelectric array sensing of volume displacement: a hardware demonstration", J. Sound and Vib. **244**(3), 395-405 (2001)

[14] B. Petitjean and I. Legrain, "Feedback controllers for active vibration suppression", J. Structural Control, **3**(1-2), 111-127 (1996)

[15] S.J. Elliott, P. Gardonio T.J. Sors and M.J. Brennan, "Active vibroacoustic control with multiple local feedback loops." J. Acoust. Soc. Am. **111**(2), 908-915 (2002)

[16] S.J. Elliott and P. Gardonio, "Active control of sound transmission," Proceedings of Inter Noise 2001, The Hague, The Netherlands, 27-30 August (2001), pp 671-680

[17] P. Gardonio and S.J. Elliott, *Driving point and transfer mobility matrices for thin plates excited in flexure*, ISVR Technical Report No 277 (1999)

[18] G.B. Warburton, *The dynamical behaviour of Structures*, (Pergamon Press,1976)

[19] S. J. Elliott and M. E. Johnson, "Radiation modes and the active control of sound power," J. Acoust. Soc. Am. **94**(4), 2194-2204 (1993)

[20] B. Wang, C.R. Fuller and E.K. Dimitriadis, "Active control of noise transmission through rectangular plates using multiple piezoelectric or point force actuators", J. Acoust. Soc. Am. **90**(5), 2820-2830 (1991)

[21] E. L. Hixson, "Mechanical Impedance", *Shock and Vibration handbook,* edited by C. M. Harris and C. E. Crede (McGraw-Hill, USA, 1976), Chap. 10

[22] S. S. Rao, "Vibration measurement and applications", *Mechanical Vibration*, (Addison-Wesley, USA,1995), Chap. 10

[23] W. Weaver, jr., S. P. Timoshenko and D. H. Young, *Vibration problems in engineering*, (John Wiley & Sons, USA,1990)

[24] C.K. Lee, "Theory of laminated piezoelectric plates for the design of distributed sensor/actuators. Part I: governing equations and reciprocal relationships", J. Acoust. Soc. Am. **87**(3), (1990)

[25] D. J. Nefske and S. H. Sung, "Sound in Small Enclosures", *Noise and Vibration control Engineering*, edited by L. L. Beranek and I. L. Ver (John Wiley & Sons, USA,1992), Chap. 6